

Particle dynamics simulation and diagnostics of the PECVD
processes in fluorocarbon rf discharges

Von der Fakultät Mathematik und Physik der Universität
Stuttgart zur Erlangung der Würde eines Doktors der
Naturwissenschaften (Dr. rer. nat.) genehmigte Abhandlung

Vorgelegt von

Jakob Philipp Barz

aus Tübingen

Hauptberichter: Prof. Dr. rer. nat. habil. Achim Lunk

Mitberichter: Prof. Dr. rer. nat. habil. Tilman Pfau

Tag der mündlichen Prüfung: 29.03.2010

Institut für Plasmaforschung der Universität Stuttgart

2010

Acknowledgments

First of all, I want to thank my family and friends for their support and patience during the preparation of this thesis. Many many thanks especially to Erwaa and Jasmin.

Prof. Achim Lunk is thanked for taking the time for many helpful discussions, in particular on the physical aspects of plasma processes, and for the very kind and same time exact supervision of this work. Many thanks also for the warm reception at the Institute for Plasma Research and the invitations to the summer garden parties.

Many thanks to Prof. Tilman Pfau for taking the part of being the second supervisor of this thesis.

Many thanks also to Prof. Herwig Brunner and Prof. Thomas Hirth for giving me the opportunity to start a PhD at the Fraunhofer IGB and for the upgrading to a full position in 2007.

Dr. Christian Oehr is thanked for many fruitful and stimulating discussions (often on friday evenings), especially on the chemical point of views of plasmas and on world politics.

I also want to thank my colleagues Bentsian Elkin, Michael Haupt, Joachim Mayer, Michaela Müller, Michael Müller, Monika Riedl, Igor Vinogradov, and Uwe Vohrer, and those not mentioned by name and who contributed to this work.

The Federal Ministry for Education and Research (BMBF) is gratefully acknowledged for financing parts of this work and instrumentation under FKZ 03N8022 and FKZ 13N8662.

Contents

Symbols, acronyms and glossary	7
Summary and conclusion	11
Deutsche Zusammenfassung der Arbeit	15
Tasks and aims	19
1 Particle dynamics in plasmas	21
1.1 Processes in gas discharges (overview)	21
1.2 The balance and transport equations	23
1.2.1 Transport kinetics in plasmas	23
1.2.2 Plasma-related transport equations	26
1.2.3 A simplified discharge model	28
1.2.4 Fragmentation of molecules	29
1.3 Chemical processes in the volume and on the surface	31
1.3.1 Chemical reaction kinetics	31
1.3.2 Chemical kinetics in plasmas	34
1.3.3 Fluorocarbon reactions	37
2 Experimental setup and measurements	43
2.1 Plasma reactor and measurements of the electrical discharge parameters	43
2.2 Laser-induced fluorescence	45
2.2.1 Setup of LIF	45
2.2.2 Calibration of CF densities	48
2.2.3 Calibration of difluorocarbene densities	53
2.2.4 Calibration of the density profiles by LIF	57
2.3 Mass Spectrometry	60
2.4 Characterization methods for plasma polymer	63
3 Modeling of the plasma	65
3.1 Modeling of electron-molecule interactions with BOLSIG+	65
3.1.1 Influence of cross section data	68
3.1.2 Influence of additional parameters	72

3.1.3	Parameter dependence of rate coefficients	79
3.2	Modeling of plasma particle dynamics in SIGLO-RF	81
3.2.1	Input parameter file of SIGLO-RF	82
3.2.2	Modeling results	86
3.2.3	Dissociation rate coefficients	90
3.3	Modeling of chemical processes	95
3.3.1	Dissociation and reaction processes	95
3.3.2	Additional effects of ions on the plasma chemistry	98
4	Comparison between modeling and experimental results	103
4.1	Results of particle dynamics in simulation and experiment	103
4.1.1	Comparison of electrical discharge characteristics	104
4.1.2	Comparison of the electron density and its distribution	111
4.2	Gas phase kinetics of single-carbon species	115
4.2.1	CF temporal and spatial development	115
4.2.2	Difluorocarbene temporal and spatial development	117
4.2.3	Modeling of kinetics of single-carbon species	132
4.2.4	Discussion of single-carbon kinetics in the gas phase	138
4.2.5	Summary of radical kinetics	143
4.2.6	Production of single-carbon species at the walls	144
4.3	Gas phase kinetics and oligomer formation	150
4.3.1	Oligomer production probed by QMS	150
4.3.2	Modeling of oligomer formation	156
4.3.3	Discussion of oligomer formation	160
4.4	Gas phase reactions and polymer deposition	161
4.4.1	Polymer deposition and polymer properties	161
4.4.2	Correlation between polymer deposition and oligomer formation	171
A	Gas flow dynamics in the reactor	175
B	LIF image calibration	179
	Bibliography	181
	List of figures	193
	List of tables	197

Symbols, acronyms and glossary

α	n_-/n_e ; degree of ionization $(n_+ + n_-)/n_n$ (context dep.)
α_d	polarizability
ϵ	electron energy
γ	T_e/T_i
$\vec{\Gamma}$	flux
η	viscosity
θ	angle with of the velocity respect to the electric field vector
κ	decay constant
λ	thermal conductivity; wavelength (context dependent)
λ_{De}	Debye length
λ_i	mean free path
μ	mobility
μ_0	zero-field mobility
μ_r	reduced mass
ν	frequency
ω	angular frequency
Ω	collision integral
Φ	quantity
ρ	density
σ	cross section
a	parameter
B	Einstein coefficient for absorption
c	concentration
c_c	concentration in the reactor center
d	distance, thickness (absorption)
d	electrode spacing, 45 mm
D	diffusion coefficient
dc	duty cycle: t_{on}/T
e	elemental charge
E	energy
\vec{E}	electric field
$f(\vec{x}, \vec{v}, t)$	distribution function

$f(\epsilon)$	electron energy distribution function
F	excitation efficiency; gas flow (context dependent)
\vec{F}	force
\vec{g}	gravitation force
H	enthalpy
I	intensity
\vec{j}	current density
k	Boltzmann constant
K	detection efficiency
$k_{1,2,3}$	first, second, third order rate
m	mass; inclination (context dependent)
M	(molecular) mass, also: collision partner
n, N	number of backbone atoms; number density (context dep.)
p, \tilde{p}	pressure, pressure tensor
P	power
Q	heat
q	charge
q_r	radiation source term
R	branching ratio
r	radial position
$r_{F/C}$	fluorine-to-carbon ratio
$r_{FC/HFC}$	fluorocarbon-to-hydrofluorocarbon ratio
S	source term; surface area (context dependent)
T	absolute temperature; pulse period (context dependent)
t	time
U	voltage
u_B	Bohm velocity
u_s	ion sheath velocity
\vec{v}	velocity
V	volume
W	work
w_i	mass fraction
x_i	mole fraction
\vec{x}	position
z	axial position; position along \vec{E} (context dependent)
z_c	axial center position ($z = d/2 = 22.5$ mm)
$-/+/e/i/n/ol$	negative/positive charge/electron/ion/neutral/oligomer

afterglow	post-discharge regime (technical term)
amu	atomic mass unit
ARXPS	angle resolved XPS
BOLSIG+	electron Boltzmann-equation solver
ccp	capacitively coupled plasma
Comsol	multiphysics modeling and simulation software
cw	continuous wave
EEDF	electron energy distribution function
EPR	electron paramagnetic resonance (syn. ESR)
ESR	electron spin resonance
FC	fluorocarbon
fwhm	full width at half maximum
glow	plasma-on time (technical term)
HFC	hydrofluorocarbon
hw	helicon wave plasma excitation
icp	inductively coupled plasma
ICCD	intensified charge-coupled device
IR	infrared
LIF	laser-induced fluorescence
LIFBASE	database and spectral simulation software
LLIF	linear laser-induced fluorescence
OES	optical emission spectroscopy
OPO	optical parametrical oscillator
PECVD	plasma-enhanced chemical vapor deposition
PLIF	planar laser-induced fluorescence
pp	parallel-plate reactor setup
QMS	quadrupole mass spectrometer
rf	radio frequency
RIE	reactive ion etching ((mostly) asymmetric ccp)
sc	standard conditions, parameters see Table 2.1
sccm	standard cubic centimeter per minute
SIGLO-RF	1-D fluid model software for ccp discharges
TOF-SIMS	time-of-flight scanning ion-mass spectroscopy
UV	ultraviolet part of the electromagnetic spectrum
UI probe	current-voltage probe
Vis	visible part of the electromagnetic spectrum
XPS	x-ray photoelectron spectroscopy

Summary and conclusion

The present work deals with the investigation of fluorocarbon plasmas by different experimental methods and supporting numerical analysis of the plasma with an emphasis on plasma-chemical interactions. Several insights could be gained from the combined experimental and numerical approaches, especially concerning the conclusiveness of the results and previous observations from the literature.

Plasma diagnostics were performed with non-invasive methods, such as UI probe measurements, microwave interferometry, laser-induced fluorescence, UV absorption measurements, and mass spectrometry. The complementary numerical simulations accounted for the electron-neutral interactions, discharge dynamics, and chemical reactions.

From the excitation and ionization cross sections of argon as well as the dissociation, ionization, and attachment cross sections of trifluoromethane (CHF_3), the field-dependence of transport parameters were obtained. These transport parameters were used as input data for fluid-modeling of the discharge. For the plasma dynamics simulation, the Boltzmann-equation was solved numerically for transport of mass, momentum, and energy in a time-dependent two-term approach. The so-obtained electron density and the power-voltage characteristics were compared to measurements with microwave interferometry and the UI probe, respectively.

An overall good agreement of the numerical and measured electron densities was obtained over a large variation range of plasma power, gas composition, and pressure. The power-voltage characteristics showed a good agreement between numerical results and data obtained right after ignition of plasma. It was further found that the measured data showed time-dependent developments from which strong deviations resulted. The time scales of changes were typically in the range of milliseconds to seconds after ignition. It was concluded that compositional changes in the gas phase were the reason. The high abundance of oligomers as well as small molecules like HF in the gas phase on one hand, and the loss of molecules by polymer deposition on the other hand affect the charge carrier mobilities and the ionic composition, such result in the changes observed.

Furthermore, from this investigation, the major fragmentation processes were identified: $\text{CHF}_3 \xrightarrow{e} \text{CF}_3 + \text{H}$ is the highest-yield neutral dissociation process ($k \approx 8 \times 10^{-11} \text{ cm}^3\text{s}^{-1}$), followed by $\text{CHF}_3 \xrightarrow{e} \text{CHF}_2 + \text{F}$ ($k \approx 5.28 \times 10^{-11} \text{ cm}^3\text{s}^{-1}$). Other neutral dissociation processes had rates being orders of magnitude lower. Ionic channels of importance were $\text{Ar} \xrightarrow{e} \text{Ar}^+ + e$ ($k \approx 7 \times 10^{-13} \text{ cm}^3\text{s}^{-1}$), $\text{CHF}_3 \xrightarrow{e} \text{CF}_3^+ + \text{H} + e$ ($k \approx 2 \times 10^{-12} \text{ cm}^3\text{s}^{-1}$), $\text{CHF}_3 \xrightarrow{e} \text{CHF}_2^+ + \text{F} + e$ ($k \approx 5 \times 10^{-14} \text{ cm}^3\text{s}^{-1}$). Finally, the rate of the attachment process $\text{CHF}_3 \xrightarrow{e} \text{CHF}_2 + \text{F}^-$ was determined to be $k \approx 6.5 \times 10^{-12} \text{ cm}^3\text{s}^{-1}$. So far, a good agreement to a similar simulation study in the literature was found which in this particular case proofed the equality of the fluid model approach for ions and electrons used herein to Monte-Carlo methods.

For the investigation of the reaction-diffusion processes, investigations by laser-induced fluorescence were carried out. In order to obtain best resolution along the axial direction of the plasma reactor, the conventional crossed-beam technique was modified. Such, a resolution of up to $60 \mu\text{m}$ became possible. Thus, highly-resolved axial densities of two plasma abundant intermediates, CF (fluoromethylidene) and CF_2 (difluorocarbene), were obtained. Pulsing of the plasma was found to be appropriate for the study of creation and reaction kinetics. For the analysis of the gas phase kinetics, a numerical chemical-diffusion model was set up. The density of CF was found to fast increase and saturate after plasma ignition, and was basically produced via fluorine abstraction from CF_2 by reaction with hydrogen. The analysis revealed that the loss resulted mainly in the formation of CF_2 . The increase of CF_2 was accompanied by the development of a concave density profile along the plasma reactor, resulting from strong wall production of the molecule during the plasma glow. Another formation reaction was hydrogen-induced abstraction of fluorine from CF_3 . It was further found by modeling that HF was highly abundant from the plasma as well as large fluorocarbon species, which were further probed by mass spectrometry. The overall process can be roughly described by the balance $n\text{CHF}_3 \rightarrow (\text{CF}_2)_n + n\text{HF}$.

To complete the analysis of the plasma dynamics, the deposition of plasma polymer onto substrates was examined. The deposition rate was determined, and changes in the surface chemistry at the transition from uncovered substrates to closed films was revealed. For the identification of the deposition precursors, results from the chemical-diffusion model were adopted for the analysis.

The oligomer molecules, which are produced at high results according to the simulation, were shown to correlate well with the polymer deposition rate. It was found by electron spin resonance (ESR) that chemical reactions took place within the deposited polymer films. The restructuring of the polymer by these reactions resulted in highly cross-linked films according to x-ray photoelectron spectroscopy (XPS). Further, it was found that the amount of fluorine in the polymer was lower than could be expected from the oligomers formed according to the chemical model. Such, it was suggested that ejection of fluorine containing species was taking place especially during the plasma glow, promoted by electron and ion bombardment, and radiation. Moreover, the ejection of fluorine containing species was tentatively ascribed to the production of CF_2 at the surface of the plasma chamber as observed by LIF. Although difluorocarbene is a reactive molecule, it does not possess unpaired electrons due to its sp^2 hybridization. Such way, the ejection of this molecule is much more likely than e.g. the ejection of radicals.

Concluding, radical and metastable fluxes from the electrodes, combined with isotropic gas phase reactions, determine the density profiles of several species from trifluoromethane plasmas. They strongly feed back the plasma chemistry, which itself feeds back the plasma particle dynamics. According to models, the deposition occurs via formation of oligomers in the gas phase, which deposit on the surface either as neutrals or ions, and become crosslinked by subsequent reactions. The origin of the particle fluxes at the electrodes is not yet identified, but indications were found for the chemical cross-linking processes being the cause. For future work, it is recommended to apply complimentary techniques for the detection of radicals in polymer layers as well as chemical changes in the polymer network. Both techniques should be applied in a time-resolved mode, with a special emphasis to study afterglow relaxation processes: In this regime of pulsed plasmas, disturbances due to processes in the former plasma bulk are expected to have a minor influence on the deposit, and inner relaxation might be identified easier.

Deutsche Zusammenfassung der Arbeit

In der vorliegenden Arbeit wurden Fluorkohlenstoffplasmen auf Basis von Argon-Trifluormethanmischungen, teilweise mit gepulster Radiofrequenzanregung, durch verschiedene experimentelle Methoden untersucht. Auf unterschiedlichen Gebieten, nämlich der Elektron-Neutralteilchenwechselwirkung, der Teilchendynamik sowie der Untersuchung physikalisch-chemischer Transporterscheinungen kamen unterstützend numerische Verfahren zum Einsatz, um das Zusammenspiel von Teilchendynamik und chemischen Reaktionsprozessen zu untersuchen. Durch die Kombination von experimentellen und numerischen Ansätzen konnten Einblicke in die häufig sehr komplexen Vorgänge in Plasmen gewonnen werden: In diesen Plasmen lassen sich physikalische und chemische Vorgänge aufgrund starker Überlagerung ansonsten kaum voneinander trennen. Zudem konnte die Schlüssigkeit der in dieser und in vorigen Arbeiten gewonnenen Erkenntnisse durch diese Herangehensweise überprüft werden.

Es kamen hierzu nicht-invasive plasmadiagnostische Methoden zum Einsatz. Dabei handelte es sich um Strom-Spannungsmessungen, Mikrowelleninterferometrie, laserinduzierte Fluoreszenz, Absorptionsmessungen im ultravioletten Wellenlängenbereich sowie Massenspektrometrie.

Die ergänzend durchgeführten numerischen Simulationen betrafen im ersten Schritt die Elektronen-Neutralteilchen-Wechselwirkungen wie Dissoziation und Ionisation. Im zweiten Schritt wurde eine Radiofrequenzentladung simuliert, es folgte abschließend eine Modellierung der chemischen Prozesse.

Auf Basis von Literaturdaten wurden die Raten der Stoßprozesse von Elektronen mit Argon und Trifluormethan (CHF_3) berechnet. Die resultierenden Transportparameter wie z.B. die Elektronen- und Ionenmobilitäten wurden als Datengrundlage für die nachfolgende Plasmamodellierung verwendet. Für die Teilchendynamiksimulation wurde ein zwei-Flüssigkeiten-Modell gewählt, das über den Ansatz der Boltzmanntransportgleichungen für Masse-, Impuls- und Energietransport numerisch gelöst wurde.

Als meßbare Größen resultierten hieraus die Elektronendichte sowie die Leistungs-Spannungscharakteristika von unterschiedlichen Entladungen. Hierzu wurden äußere Einstellparameter wie Leistung, Gasflüsse und Gesamt-

druck variiert. Der Vergleich der berechneten mit den über Mikrowelleninterferometrie gemessenen Elektronendichten ergab eine gute Übereinstimmung. Im Falle der Leistung-Spannungs-Kennlinien ergab sich zunächst eine gute Übereinstimmung direkt nach Zündung des Plasmas, doch trat eine zeitabhängige Veränderung der Kennlinien auf. Eine Detailanalyse ergab, daß sich die Charakteristika in Zeiträumen von Millisekunden bis hin zu mehreren Sekunden nach Zünden der Entladung veränderten. Daraus kann geschlossen werden, daß die Bildung neuer, oligomerer Spezies sowie von kleinen Molekülen wie Flußsäure (HF) im Gasraum für dieses Phänomen verantwortlich ist. Auch der Verlust von Teilchen durch Abscheidung eines Polymerfilmes führt zu einer Veränderung der Zusammensetzung gasförmiger Teilchen. Insgesamt ändern sich dadurch die Mobilitäten der Ladungsträger sowie die Wirkungsquerschnitte für Ionisations- und Elektronenanlagerungsprozesse, wodurch die Entladungscharakteristika offensichtlich beeinflusst werden.

Die Hauptprozesse molekularer und atomarer Elektronenwechselwirkung wurden identifiziert: Vorwiegend dissoziiert CHF_3 in Neutralteilchen über $\text{CHF}_3 \xrightarrow{e} \text{CF}_3 + \text{H}$ mit einer Rate von $k \approx 8 \times 10^{-11} \text{ cm}^3\text{s}^{-1}$, gefolgt von $\text{CHF}_3 \xrightarrow{e} \text{CHF}_2 + \text{F}$ ($k \approx 5.28 \times 10^{-11} \text{ cm}^3\text{s}^{-1}$). Andere Neutralteilchen-Dissoziationsprozesse spielen keine Rolle, da ihre Raten um Größenordnungen niedriger sind. Die Hauptionisationsprozesse sind $\text{CHF}_3 \xrightarrow{e} \text{CF}_3^+ + \text{H} + e$ ($k \approx 2 \times 10^{-12} \text{ cm}^3\text{s}^{-1}$), $\text{CHF}_3 \xrightarrow{e} \text{CHF}_2^+ + \text{F} + e$ ($k \approx 5 \times 10^{-14} \text{ cm}^3\text{s}^{-1}$). Zur Entstehung von Kationen trägt des weiteren $\text{Ar} \xrightarrow{e} \text{Ar}^+ + e$ ($k \approx 7 \times 10^{-13} \text{ cm}^3\text{s}^{-1}$) bei. Schließlich wurde die Rate des Elektronenanlagerungsprozesses $\text{CHF}_3 \xrightarrow{e} \text{CHF}_2 + \text{F}^-$, der ebenfalls dissoziativ ist, zu $k \approx 6.5 \times 10^{-12} \text{ cm}^3\text{s}^{-1}$ bestimmt. An dieser Stelle wurde eine gute Übereinstimmung mit Literaturdaten festgestellt, die aus einer Studie unter ähnlichen Voraussetzungen resultierten. Damit konnte die Gleichwertigkeit des in dieser Arbeit verwendeten zwei-Flüssigkeiten-Modells für Elektronen und Ionen mit den Resultaten von Monte-Carlo-Methoden bestätigt werden.

Zur Untersuchung der chemischen Diffusionsvorgänge wurden Untersuchungen mit laserinduzierte Fluoreszenz durchgeführt. Um die Auflösung dieser Technik für die Erstellung axialer Dichteprofile zu verbessern, wurde die konventionelle crossed-beam-Technik abgewandelt. Durch diese Abwandlung ist es möglich, eine Auflösung von bis zu $60 \mu\text{m}$ zu erreichen. Die axialen Dichten von zwei wichtigen Zwischenprodukten, CF (Fluormethylen) und CF_2 (Difluorcarben), wurden unter verschiedenen Bedingungen vermessen. Es stellte sich heraus, daß für eine Analyse der stattfindenden

chemischen Vorgänge in Plasmen gepulste Leistungseinspeisung besonders geeignet war. Die Ergebnisse der Messungen wurden mit Ergebnissen aus einem numerischen Finite-Elemente-Modell zur Berechnung chemischer Diffusionsvorgänge abgeglichen. Zeitaufgelöste Messungen der CF-Dichte ergaben stets eine schnelle Zunahme zu Beginn eines Plasmapulses, die kurz nach der Plasmazündung in einen stabilen Gleichgewichtszustand überging. Die Erzeugung des CF ließ sich auf die Abstraktion eines Fluoratoms von CF₂ durch die Reaktion mit Wasserstoff (CF₂ + H → CF + HF) zurückführen. Die Verlustprozesse führten hauptsächlich zur Produktion von CF₂. Die Zunahme von CF₂ wurde von der Entwicklung eines konkaven Dichteprofiles in axialer Richtung infolge starker Wandproduktion während der Glimmphase des Plasmas beherrscht. Eine weitere Quelle war Fluorabstraktion von CF₃. Im Rahmen der Reaktionsanalysen stellte sich heraus, daß HF sowie makromolekulare Fluorkohlenstoffe in großen Konzentrationen vorliegen, wie experimentell über Massenspektrometrie nachgewiesen werden konnte. Die Gesamtbilanz nCHF₃ → (CF₂)_n + nHF beschreibt grob diese Vorgänge in der Gasphase.

Um die Analyse der im Plasma stattfindenden Prozesse abzuschließen wurde die Abscheiderate von Plasmapolymer auf Siliziumwafern untersucht. Die Veränderungen der Oberflächenchemie beim Übergang von einem unbeschichteten Substrat bis zu einem geschlossenen Film wurden hinsichtlich der Stöchiometrie untersucht, um eine Korrelation zur Oligomerbildung in der Gasphase herzustellen.

Wie gezeigt werden konnte, gibt es einen eindeutigen Zusammenhang zwischen der Konzentration der Oligomermoleküle, die grundsätzlich abgeschieden werden können, und der tatsächlichen Abscheiderate. Die Oligomerbildung ist dabei deutlich höher als die Abscheiderate. Über Elektron-Spin-Resonanz (ESR) konnten chemische Reaktionen innerhalb des Polymers selbst lange nach Abschluß der Plasmaabscheidung nachgewiesen werden. Diese Reaktionen bewirken bekanntlich eine Umstrukturierung innerhalb des Polymers, die beispielsweise zu der Ausbildung höherer Quervernetzung führen kann. Die hohe Quervernetzung konnte über Röntgen-Photoelektronenspektroskopie (XPS) nachgewiesen werden. Des weiteren wurde im Rahmen der chemischen Analytik festgestellt, daß der Fluorgehalt des abgeschiedenen Materials geringer war als die Zusammensetzung der Oligomermoleküle gemäß der chemischen Modellierung vermuten ließe. Es ist also davon auszugehen, daß die Umstrukturierungsprozesse innerhalb des Polymerfilmes, insbesondere während der Plasmaentladung, bei der

starker Energieeintrag durch Teilchenbeschuß und Strahlung stattfindet, zum Ausstoß von fluorhaltigen Molekülen führen. Zu den ausgestoßenen Fluorverbindungen kann man Difluorcarben hinzuzählen, da eine starke Oberflächenproduktion dieses Moleküls mit LIF nachgewiesen werden konnte. Difluorcarben ist zwar chemisch durchaus noch reaktiv, besitzt aber dennoch aufgrund seiner sp^2 -Hybridisierung keine ungepaarten Elektronen, was einen Ausstoß gerade dieser Teilchen erheblich wahrscheinlicher macht als beispielsweise die Freisetzung von Radikalen.

Abschließend läßt sich also feststellen, daß Ströme metastabiler Teilchen von den Elektroden in das Reaktorvolumen hinein, zusammen mit nahezu isotropen Gasphasenreaktionen, anisotrope Dichteverteilungen in Trifluormethan-Plasmen hervorrufen. Die Teilchenströme haben eine starke Auswirkung auf die Plasmachemie, die ihrerseits auf die Teilchendynamik rückkoppelt. Die Abscheidung erfolgt gemäß den Modellvorstellungen aus in der Gasphase gebildeten Oligomeren, die entweder neutral oder ionisiert auf der Oberfläche abgeschiedenen werden, und dort durch nachfolgende Reaktionen vernetzt werden. Die Ursache der Teilchenproduktion konnte zwar nicht abschließend geklärt werden, doch gibt Anzeichen dafür, daß genannte chemische Vernetzungsprozesse innerhalb des abgeschiedenen Filmes dafür verantwortlich sind. Zur Klärung dieses Sachverhaltes sollten in Zukunft in-situ-Untersuchungen mit geeigneten Methoden durchgeführt werden, um die Schichtabscheidungs- und Quervernetzungsprozesse genauer zu untersuchen. Es empfiehlt sich dabei, die Messungen mit zeitaufgelösten Methoden in der Nachglimm-Phase, im sogenannten Afterglow, von Pulsplasmen durchzuführen: In diesem Bereich liegt einerseits noch eine hohe Reaktivität in der Schicht vor, doch sind die Störungen durch die Einwirkung des Plasmas minimal.

Tasks and aims

The understanding of fluorocarbon plasmas is a topic of relevance especially to the semiconductor industry. During the fabrication of electronics, etching as well as polymer deposition, e.g. as side-wall passivation, are of importance. In other industrial branches, fluorocarbon plasmas are applied for deposition of low-k dielectrics or hydrophobic and oleophobic, or antifrictional PTFE-like coatings.

Plasma physics and plasma chemistry of these plasmas are both complex. Such, for example, negative atomic and molecular ions are produced which require advanced analytical tools to be detected and which enhance the complexity of discharge simulations. On the other hand, plasma-chemical reactions are manifold, as besides "conventional" gas phase chemistry based on thermochemical reaction kinetics, reactive species are produced for example by the collision with electrons.

In the past, a lot of experimental research has been carried out to either investigate the plasma physical or the plasma chemical properties. The approaches are commonly based on experimental methods such as probe measurements of the electronic and ionic properties, and of the electrical discharge characteristics to describe the plasma physical part, or optical methods or mass spectrometry in order to assess the chemistry of plasmas. Despite of many experimental achievements, a comprehensive picture can be hardly obtained as many parameters or species remain unknown, or can not be traced with reasonable effort. Such, modeling of fluorocarbon discharges is often carried out in etching as well as depositing plasmas. A major problem still remain the chemical reactions occurring in the discharge, as the reaction rates of several processes were not yet investigated by chemists, and furthermore the unknown ionization and fragmentation cross sections of many molecules. Such way, the simulation always requires verification by experiments on an advanced level.

The present work is dedicated to the description of gas phase processes occurring in CHF_3/Ar plasmas and further of plasma-wall interactions. The aim is to overcome inconsistencies found in the literature and to identify key processes within the discharge. This especially concerns the time-dependent

chemical kinetics of reactive species as they are the most discussed topic in fluorocarbon plasmas. In addition to that, the deviations of the plasma characteristics from the idealized model due to chemical processes are in focus as well.

This is carried out by both particle dynamics simulations and different experimental methods. First, on a microscopic scale, the interactions of electrons with atoms and molecules are modeled. With the outcome of this step, on a mesoscopic to macroscopic scale, a particle dynamics model of electrons and ions within a discharge is developed. Here, a fluid approach is applied for the collective motion of each type of charge carrier. The calculated macroscopic characteristics of the discharge such as the electron density and the power-voltage characteristics are compared to experimental results. Furthermore, the process rates of the electron-molecule interactions are evaluated and such, the production rates of species to be included in the chemical model are obtained as an interface between plasma physics and plasma chemistry. To obtain a model for the plasma chemistry, thermochemical data of fluorocarbon species and other sources of chemical reactions have to be considered.

For the investigation of gas phase processes on the microscopic scale, laser-induced fluorescence is applied to detect intermediate, reactive species which could either be produced directly by electron-molecule interactions or by subsequent chemical reactions. Here, a good spatial resolution is required in order to trace-back anisotropies arising e.g. from plasma-wall interactions. For the anisotropies, several models are under discussion which include production and/or loss processes of the species at or close to the chamber walls. The models and perceptions from the literature are compared to the experimental observations and to the modeling of the plasma processes performed herein. In addition to that, mass spectrometry is applied to study the development of oligomer species as precursors for polymer deposition. Finally, the processes leading to polymer formation are discussed on the basis of the experimental and modeling results.

This work stands out of previous investigations on this field, as both experiments and modeling are mutually matched and conducted in a coactive manner.

Chapter 1

Particle dynamics in plasmas

1.1 Processes in gas discharges (overview)

The present work deals with the investigation of physical and chemical processes in fluorocarbon gas discharges. Fluorocarbon processes are one of the most successful applications of plasma technology and can be applied for both etching and coating of surfaces (see [1, 2]). Although they are therefore under continuous investigation by many groups, the results of the investigation of processes occurring in these plasmas are often contradicting, which is due to several effects.

Fluorocarbons are electronegative compounds, that means, negative molecular or atomic ions can be formed. Due to this, the charge carrier transport is much more sophisticated than e.g. in inert gas plasmas. The particle dynamics of charge carriers involving positive ions, negative ions, and electrons are highly complex due to electrostatic interactions between the charge carriers. Transport within these plasma can be dominated by phenomena like ambipolar diffusion. Furthermore, the transport processes are anisotropic in space.

In general, three zones are differentiated in radio-frequency gas discharges as depicted in Figure 1.1. The zone around the plasma center, in which the densities of positive as well as negative charge carriers are high, is referred to as the bulk plasma. In this zone, the discharge is quasi-neutral, i.e. $n_+ = n_e + n_-$. The bulk plasma is separated from the electrodes by the plasma sheath region. In this region, positive and negative charges are present in different amounts due to different mobilities and plasma frequencies of ions and electrons. Concerning the plasma frequency, for example, only electrons can follow the oscillating electric field in the plasma bulk ($\omega_{plasma,i} < \omega_{exc.} < \omega_{plasma,e}$).

Many fluorocarbon species are reactive. The physical process of electron collision induced dissociation of the feed gas (blue in Figure 1.2) is the

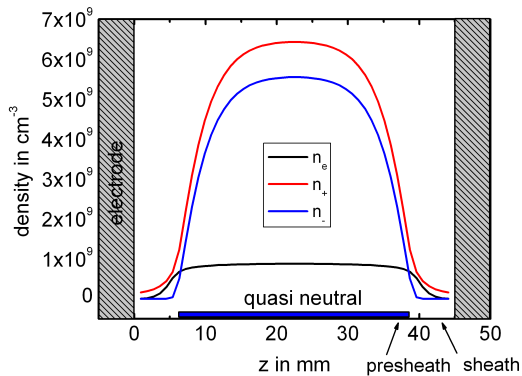


Figure 1.1: Plasma regions in electronegative discharges at 13.56 MHz excitation frequency (graph from two-fluid model).

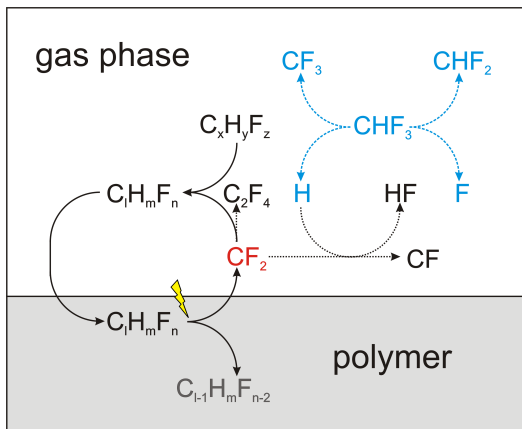


Figure 1.2: Reaction zones in the examined fluorocarbon plasmas.

initiation of chemical reactions. As a consequence, besides small fragments being formed, also large molecules (oligomers) can be produced. The concentration of molecules are determined by complex and partially cyclic gas phase and surface processes (marked red in the figure). Both, the small fragments and the oligomers, possess different electron collision cross sections compared to the parent feed-gas molecules. Such, the electrical discharge characteristics are subjected to changes depending on the chemical processes occurring in the gas phase.

To obtain a self-consistent description of both dynamics and plasma chemistry, it is hardly possible to separate both plasma dynamics and plasma chemistry under the given conditions. In the recent years, several techniques have been applied to understand fluorocarbon plasmas. As experimental methods, amongst others, optical techniques were applied like optical-emission spectroscopy, laser-induced fluorescence, UV/Vis absorption spectroscopy and IR absorption techniques. These optical techniques are mainly targeting species being formed or excited in the plasma. Information about plasma parameters like the electron energy distribution and the electron density, but also on oligomer formation and other chemical processes can be obtained either by measurements or by numerical modeling. The mathematical basics are described in the following sections. With them, the whole range from microscopic particle dynamics (e.g. electron-molecule collisions) to the particle dynamics on a mesoscopic/macroscopic scale (e.g. dynamics of the charge carriers in the discharge, description by fluids) can be covered.

1.2 The balance and transport equations

1.2.1 Transport kinetics in plasmas

For the transport of molecules by flows or diffusion as well as for the physics of discharges, the same fundamental principles are applied. In general, the transport of momentum, energy, and matter obeys the continuity equation. It is given by

$$\dot{\phi} = -\text{div}\vec{j} + S \quad (1.1)$$

and is the basis of all following transport equations. ϕ is a quantity, for example density, \vec{j} describes the current density of ϕ , and S is a source term. For the description of transport, the Navier-Stokes equations, Fick's laws, and the Boltzmann transport equation are deduced.

1.2.1.1 Navier-Stokes Equations

The Navier-Stokes equations consider the conservation of mass, momentum, and energy in hydrodynamic flows:

$$\frac{\partial \rho}{\partial t} + \operatorname{div}(\rho \vec{v}) = 0, \quad (1.2)$$

$$\frac{\partial \rho \vec{v}}{\partial t} + \operatorname{div}(\rho \vec{v} \otimes \vec{v} + \tilde{p}) = \rho \vec{g}, \quad (1.3)$$

$$\frac{\partial \rho_e}{\partial t} + \operatorname{div}(\rho_e \vec{v} - \lambda \operatorname{grad} T) + \tilde{p} : \operatorname{grad} \vec{v} = q_r. \quad (1.4)$$

Here, \vec{v} is the velocity, ρ the density (an index stands for velocity or energy density), \tilde{p} is the pressure tensor (hydrostatic and viscose pressure), \vec{g} is gravitational acceleration, λ the thermal conductivity, and q_r is an additional source term for radiation [3]. The above form requires simplifications to be solved, especially the momentum term. For gas flows in plasma reactors, incompressible flows are assumed for simplicity. Accordingly, the momentum equation simplifies to

$$\left(\frac{\partial \rho \vec{v}}{\partial t} + (\vec{v} \nabla) \vec{v} \right) = -\nabla p - \nabla \times [\eta (\nabla \times \vec{v})] + \frac{4}{3} \nabla (\eta \nabla \vec{v}) + \vec{F}. \quad (1.5)$$

This simplified equation is referred to as the Navier-Stokes equation. The viscosity therein is abbreviated by η , \vec{F} is an volume force term. The boundary condition for incompressible fluids

$$\nabla \vec{v} = 0 \quad (1.6)$$

must be fulfilled. The solution of the equation system can be carried out numerically, which was done in this work in order to determine the velocity distribution in the reactor setup, see Section A.

1.2.1.2 Diffusion and related phenomena

In case of pure diffusion, no external force is applied to the system. Instead, inherent gradients result in transport phenomena, see Table 1.1.

From Equation (1.1) with $\phi = \rho$, one obtains Fick's laws when the flux \vec{j} is originating from an internal concentration gradient:

$$\vec{\Gamma} = -D \operatorname{grad} \rho. \quad (1.7)$$

Table 1.1: Transport processes due to temperature and concentration gradients

flux \ gradient	temperature	concentration
energy	Fourier's law	Dufour effect
mass	Sorét effect	Fick's law

It results

$$\dot{\rho} = D \Delta \rho. \quad (1.8)$$

D is the diffusion coefficient, ρ is the density.

With an additional reaction term r_i for sources or sinks of a species i , the reaction-diffusion equation is obtained:

$$\frac{d\rho_i}{dt} = D_i(T, \rho_i, \rho_j, \rho_k, \dots) \Delta \rho_i + r_i(\vec{x}, t). \quad (1.9)$$

1.2.1.3 Determination of diffusion coefficients in the gas phase

The diffusion coefficient depends on the interactions of the diffusing particles with their surroundings. For neutral mass transport, the diffusion coefficient is collision-controlled and therefore depends on the collision cross sections as well as the masses of the particles, and the temperature. A common approach for binary (that means two-component) gas mixtures is the use of the binary diffusion coefficient [3]

$$D_{12} = \frac{3}{8} \frac{\sqrt{2\pi kT} \frac{m_1 m_2}{m_1 + m_2}}{\pi \sigma_{12}^2 \Omega^{(1,1)*}(T_{12}^*)} \frac{1}{\rho}. \quad (1.10)$$

Here, the masses of the particles are denoted by m_i , $\sigma_{12} = (\sigma_1 + \sigma_2)/2$ is the mean molecular diameter¹. The reduced temperature $T^* = kT/\epsilon$ is a function of the absolute temperature and the depth of the Lennard-Jones potential, ϵ (the maximum attractive potential). The values are averaged over both molecules when it denoted with 12 as index. $\Omega^{(1,1)*}$ is the reduced collision integral which decreases with increasing reduced temperature.

In multi-gas mixtures, the Stefan diffusion coefficient is often used which notes as

$$D_i^j = \frac{1 - w_i}{\sum_{j \neq i} \frac{x_j}{D_{ij}}} \quad (1.11)$$

¹ σ is used as parameter in the Lennard-Jones-6-12 potential $E_{L.-J.} = 4\epsilon(\sqrt{\sigma/r}^{12} - \sqrt{\sigma/r}^6)$.

with w_i being the mass fraction and x_i as mole fraction of the species i . D_{ij} is the binary diffusion coefficient from Equation (1.10) .

1.2.1.4 Other gradient-induced transport processes

The Sorét effect (thermal diffusion) is sometimes relevant for the transport kinetics of light particles like e.g. small radicals in plasmas. To observe thermal diffusion, significant thermal gradients are required, which is given in plasmas with high power densities [4], but negligible in the plasmas examined herein. Additional transport processes (Table 1.1) are not of relevance to this work.

1.2.1.5 Boltzmann Equation

The Boltzmann transport equation is as well derived from the continuity equation (1.1) and reads as

$$\frac{\partial f}{\partial t} + \vec{v} \cdot \nabla_{\vec{x}} f + \frac{\vec{F}}{m} \cdot \nabla_{\vec{v}} f = \left. \frac{\partial f}{\partial t} \right|_{\text{coll}}, \quad (1.12)$$

with $f(\vec{x}, \vec{v}, t)$ being a distribution function in the six-dimensional phase space (\vec{x}, \vec{v}) . It accounts for the positions and velocities of the particles. $\frac{\vec{F}}{m}$ is an acceleration term, the term on the right-hand side describes collisions.

In the description of plasmas, the three lowest moments of the Boltzmann equation are commonly considered, which are the particle conservation, the momentum conservation, and the conservation of energy. They are obtained by directly integrating over the velocity space, by multiplication with \vec{v} and integration over the velocity space, and by multiplication with $\frac{1}{2}mv^2$ and integrating over the velocity space, respectively. Further details can be found in the literature [5].

1.2.2 Plasma-related transport equations

The electrical properties of plasmas are governed by the transport kinetics of electrons and ions. They shall be introduced briefly in the following passages.

The flux a charged particle in a plasma is described by the flux equation

$$\Gamma = n\vec{v} = \pm\mu n\vec{E} - D \nabla n \quad (1.13)$$

with

$$\mu = \frac{|q|}{m\nu_m} \quad (1.14)$$

being the mobility and \vec{E} being the electric field. ν_m is herein the total momentum transfer frequency (for both elastic and inelastic collisions with ions as well as electrons). The diffusion coefficient of this species is given by

$$D = \frac{kT}{m\nu_m}. \quad (1.15)$$

One of the most important relations in plasma transport modeling is the Einstein relation, obtained from inserting (1.14) in (1.15):

$$\mu = \frac{|q|}{kT} D. \quad (1.16)$$

Equation (1.16) gives an estimate for the mean electron energy by

$$\langle \epsilon \rangle = \frac{3D_e}{2\mu_e}, \quad (1.17)$$

which is defined only for Maxwellian electron-energy distributions, but applicable as an estimate also in other cases.

Due to the quasi-neutrality of a plasma, the fluxes of electrons and ions must be equal (as long as no negative ions are present). The overall diffusion coefficient therefore depends on both the mobilities of ions and electrons. Diffusive losses of charged particles in such plasmas are ambipolar, i.e. both charge carriers are lost together by diffusion. The ambipolar diffusion coefficient is given by

$$D_a = \frac{\mu_i D_e + \mu_e D_i}{\mu_i + \mu_e} \quad (1.18)$$

for plasmas of electropositive gases.

In plasmas of electronegative gases, the diffusive loss of charge carriers is no longer necessarily ambipolar, but can be under certain conditions. In the first case, the (nonlinear) diffusion equations of the three types of charge carriers must be solved simultaneously. This can only be done numerically [5] and is carried out in this work.

In some other cases, diffusional losses are ambipolar, but still, the obtained ambipolar diffusion equation is nonlinear. Then, $\Gamma_+ = \Gamma_- + \Gamma_e$ is the flux balance equation to be solved. The solution of the positive ion flux $\Gamma_+ = -D_{a+} \nabla n$ is shown as an example in a simplified form to illustrate

the enhanced complexity [5]:

$$D_{a+} \approx D_+ \frac{1 + \gamma + 2\gamma\alpha}{1 + \gamma\alpha}. \quad (1.19)$$

Here, $\gamma = T_e/T_i$ and $\alpha = n_-/n_e$.

1.2.3 A simplified discharge model

In real radio-frequency discharges at 13.56 MHz, the charge carrier densities drop towards the electrodes. In the sheath region, only positive ions and electrons are found, whereas negative ions are trapped inside the plasma bulk. As positive ions can not follow the electric field ($\omega_{p,i} \ll \omega_{rf}$), they are only accelerated in time-averaged static fields. In the plasma bulk, positive ions are accelerated in the presheath region. This is due to a slight voltage drop from the positive plasma potential in the bulk discharge towards the plasma sheath region. In case the ions exceed the Bohm-velocity u_B , the positive ions enter the sheath region, are further accelerated, and are lost as ion currents at the electrodes:

$$u_s \geq u_B \quad (1.20)$$

Here, u_s is the directed ion presheath velocity.

For electronegative gases, and under simplified, collisionless conditions, it is

$$u_B = \left[\frac{eT_e(1 + \alpha_s)}{M(1 + \alpha_s\gamma)} \right]^{1/2}. \quad (1.21)$$

T_e is the electron temperature, $\gamma = T_e/T_i$ is the ratio of electron and ion temperature, and M the mass of the considered ion.

The density-ratio of negative ions and electrons in the sheath, $\alpha_s = n_{s-}/n_e$, can be derived from the density-ratio α_b in the plasma bulk by

$$\alpha_b = \alpha_s \exp \left[\frac{(1 + \alpha_s)(\gamma - 1)}{2(1 + \gamma\alpha_s)} \right] \quad (1.22)$$

When collisions have to be considered, the Bohm velocity is effectively modified to

$$u_s = u_B \left(1 + \frac{\pi\lambda_{De}}{2\lambda_i} \right), \quad (1.23)$$

involving the Debye length λ_{De} as well as the mean free path λ_i . This only

holds for positive ions, of which some part is lost as ion current $j_i = en_s u_s$. Negative ions are throughout trapped inside the discharge. See [5, 6] for more details on these general properties.

The plasma dynamical equations of electronegative gases can hardly be solved, especially, when the exact presheath and the sheath dynamics shall be taken into consideration. A very simplified approach therefore neglects the sheath dynamics and spatial density variations. It is, however, useful for a comparison to numerical results.

The conservation of ions, electrons, and energy requires

$$0 = k_{ioniz}n_n n_e V - k_{i-i-r}n_+ n_- V - \Gamma_{+s}S \quad (1.24)$$

$$0 = k_{att}n_n n_e V - k_{i-i-r}n_+ n_- V \quad (1.25)$$

$$P_{abs} = eE_c k_{ioniz}n_n n_e V + \Gamma_{+s}S e(E_e + E_i) \quad (1.26)$$

where k_{ioniz} denotes the ionization rate coefficient, k_{i-i-r} denotes the positive-negative ion recombination rate coefficient, k_{att} is the attachment rate coefficient, and E_x are the energy-loss per electron-ion pair created, the kinetic ion energy, and the kinetic electron energy for $x = c, i, e$, respectively. P_{abs} is the absorbed power, V and S are the volume and the surface area, respectively.

In the case that positive ion currents can be neglected, that means volume losses by positive-negative ion recombination (also: "ion-ion recombination", $i-i-r$) predominate, one obtains for the absorbed power and the electron density

$$P_{abs} \approx VeE_c k_{i-i-r}n_+^2 \quad (1.27)$$

$$n_e \approx \frac{k_{i-i-r}n_+^2}{k_{att}n_n}. \quad (1.28)$$

For the case of surface losses being predominant, no consistent results are obtained from this approximation.

1.2.4 Fragmentation of molecules

Molecules can generally be dissociated by several pathways involving chemical reactions as well as ion or electron collisions, and radiation. The electrons are, contrary to the ions, far from thermal equilibrium with energies around $T_e=2-6$ eV (23200-69600 K) and appear in densities n_e of typically 10^9-10^{12} cm⁻³. In low temperature plasmas, they contribute most of the

energy for dissociation processes. Their energetic distribution is of great importance for the dissociation rates. It is partially determined by the fragmentation pattern of the considered molecule under electron impact, resulting in neutral, ionized, and attachment dissociation. Other parameters are the pressure, electron- and ion densities, and the excitation frequency.

1.2.4.1 Determination of electron-energy distributions and process rates

Rate constants can generally be obtained from cross sections by integrating over the electron-energy distribution function by

$$k(\langle\epsilon\rangle) = \frac{2}{m_e} \int_0^\infty \sigma(\epsilon)\epsilon^{1/2}f(\epsilon)d\epsilon. \quad (1.29)$$

Here, ϵ is the electron energy, $\sigma(\epsilon)$ is the cross section and $f(\epsilon)$ is the electron energy distribution function (EEDF). It is further

$$\langle\epsilon\rangle = \int_0^\infty \epsilon^{3/2}f(\epsilon)d\epsilon \quad (1.30)$$

the mean electron energy.

For the collisionless case, the EEDF is a Maxwellian. In this case, the EEDF is often described by the electron temperature as parameter:

$$\frac{3}{2}T_e = \langle\epsilon\rangle \quad (1.31)$$

The electron temperature is only defined for a Maxwellian distribution, however, it is often used in non-Maxwellian cases as well. Though Maxwellian distributions are sometimes applied to plasma chemical models, it provokes large errors due to the disregard of elastic and inelastic electron collisions. In absence of such processes, a high energy tail is obtained in the EEDF. The resulting large rates are inconsistent with the energy consumption by excitation and fragmentation processes. Such way, the electron distribution is in general not Maxwellian [7].

The Druyvesteyn distribution allows for elastic collisions with energy-independent collision frequencies [5] and therefore yields better results. However, large inelastic contributions like excitation, ionization and/or dissociation must be considered. Consequently, Druyvesteyn distributions are only of value in discharges with insignificant inelastic contributions. Such

way, advanced modeling of the EEDF is required. The EEDF can be calculated numerically as long as elastic and inelastic cross sections for electron collisions of all contributing gas molecules are available (see Section 3.1).

1.3 Chemical processes in the volume and on the surface

Plasmas are sophisticated from physical point of view, especially, when reactive atoms or molecules are present and chemical pathways strongly feedback the physical processes. Such way, the plasma parameters, i.e. the electron and ion densities, mobilities, etc., vary due to fragmentation and combination reactions, and according to the properties of the new species formed. The chemical properties are discussed in the following sections.

1.3.1 Chemical reaction kinetics

Chemical reaction data commonly lists the (standard) enthalpy change of formation for the considered molecule (synonyms: (standard) enthalpy of formation, (standard) heat of formation). When preceded by "standard", it is referred to standard conditions (1013.25 hPa, 298 K), which are generally marked by the index "0". The formula sign is $H_f^{(0)}$. It is referred to the most stable forms of the parent elements under standard conditions, which, *by definition*, have $H^0 = 0$ kJ mol⁻¹. The (standard) reaction enthalpy change of formation (synonyms: (standard) reaction enthalpy) is calculated from the enthalpies of formation of the products and reactants by Hess's law:

$$\Delta H_r = \sum_{\text{products}} n_i H_f^{(i)} - \sum_{\text{reactants}} n_i H_f^{(i)} \quad (1.32)$$

where n_i are the stoichiometric coefficients. The algebraic sign determines whether the reaction is exothermic (-) or endothermic (+). As it is

$$dH = \delta Q + V dp, \quad (1.33)$$

ΔH_r is also termed heat of reaction in case of $dp = 0$.

In Table 1.2, $\Delta H_f^{(0)}$ of several species considered in CHF₃ plasmas are listed. Reaction enthalpies ΔH_r can then be calculated easily. A compound is more stable the lower its enthalpy, a reaction is more exothermic the lower its reaction enthalpy. Although the reaction enthalpies indicate whether a

reaction is thermodynamically favorable or not, the reaction rates finally determine whether a reaction occurs or not. The rates strongly depend on reaction pathways (contrary to the reaction enthalpy): a highly exothermic reaction results in large amounts of excessive heat, which must be abducted - or back reaction or fragmentation may result. Steric hindering is another effect which may result in a low reaction rate.

Table 1.2: Enthalpies of formation

molecule	H_f^0 in kJ/mol
H ₂	0
H	218.0
F ₂	0
F	78.9
HF	-272.5
C (graphite, cr)	0
CF	240.6
CF ₂ (¹ A ₁) (sing.)	-191.3 [8]
CF ₂ (¹ B ₁) (trip.)	28.5 [8]
CF ₃	-467.4
CF ₄	-933.0
CH	594.1
CHF	163.2
CHF ₂	-247.7
CHF ₃	-697.6
C ₂ F ₃	-216.3
C ₂ F ₄	-674.5 [8]
CF ₂ – CF ₂	473.1 [8]
C ₂ F ₅	-891.2
C ₂ F ₆	-1342.6

Data from [9] if not stated differently.

In plasmas like in all other systems, the kinetics of chemical processes can have very different appearances. They have in common a dependence on the concentrations of the reactants as well as on rate coefficients. Those depend on collision rates, cross sections, and further terms. Often, but not always, kinetics can be described by a system of equations like

$$\frac{dc_i(t)}{dt} = k_i \prod_j c_j^{n_j}(t) \quad (1.34)$$

where the respective species concentrations are c_i . The product \prod_j includes the concentrations of all species involved in the reaction. As three-body collisions are already quite rare, especially in low-pressure systems, it is $j \leq 3$. The exponential index n_j is the reaction order with respect to the concentration of species j . The sum $\sum_j n_j = n$ is the reaction order n of the total reaction. It must be mentioned that in many cases, the stoichiometry is not automatically reflected in the n_j : e.g. branching reactions, radical reactions and competing processes must be considered also [10]. Such way, the reaction orders and thus the reaction rates become dependent of the reaction pathway. As a result, reaction orders of a component can be a non-natural or even negative number. Finally, k_i is the rate coefficient (also: reaction rate) for the component i , which is often temperature and pressure dependent. An alternative and much more common notation is the use of k_n , reflecting the reaction order n of the total reaction instead of using the component i as an index. Consequently, the units of $k_{n=0,1,2}$ are $\text{cm}^{-3}\text{s}^{-1}$, s^{-1} , and cm^3s^{-1} , respectively².

Standard cases of reaction orders and solutions of Equation (1.34) are shown in Table 1.3. In this table, it is further assumed that the reaction order n_j of each species participating is a natural number.

Table 1.3: Reaction orders, differential equations, and solutions

reaction order n	general d. e.	solution
0	$\frac{dc_i(t)}{dt} = k_0$	$c_i(t) = k_0 t$
1	$\frac{dc_i(t)}{dt} = k_1 c_i(t)$	$c(t) = c_0 e^{k_1 t}$
2	$\frac{dc_i(t)}{dt} = k_2 c_i(t) c_j(t)$	dim.: $c(t) = \frac{1}{k_2 t + c_0^{-1}}$

dim.: dimerization

An common example of a process of 0th order is catalytic dissociation if the catalytic area is the limiting factor. Radioactive decay is often used as an example for first order processes; here, c_0 denotes the starting concentration. Second order processes are much more complex, even when it is assumed that $n_j \in \mathbb{N} \forall j$. In Table 1.3, the example of a single-species dimerization reaction is given as a solution. It illustrates well that reaction order and number of species involved are not necessarily identical. Another trivial solution is obtained in case that one reactant exists in much higher concentration than its reaction partner. Accordingly, the kinetics are determined

² k_1 is also termed frequency, e.g. collision frequency, recombination frequency.

by the species which is faster consumed:

$$\frac{dc_i(t)}{dt} = kc_i(t) \underbrace{c_j(t)}_{\approx \text{const.}} . \quad (1.35)$$

The reaction still requires two reactants, meanwhile the kinetics formally only depend on one species having $n_j = 1$, which results in a first-order process behavior. As the original kinetic equation before simplification described a second-order process, the resulting form is *pseudo*-first order. The solution is an exponential function. Second-order processes often occur in a plasma.

The excessive heat of reaction can be either released by radiation, it can increase the internal energy (translation, rotation, vibration, electronic excitation), or a collision partner is required to prevent re-dissociation. The different possibilities are discussed in detail by Levine and Bernstein in [11]. As a consequence, some two-body reactions in the plasma require a collision partner, such, they are practically three-body reactions. In the gas phase, such reactions are pressure dependent and also depend on the matrix gas species below a threshold pressure [12–14], whereas they can be enhanced at the walls, which act as third body.

1.3.2 Chemical kinetics in plasmas

1.3.2.1 Chemical kinetics in the plasma bulk

In the gas phase, fragmentation via electron impact creates ground state neutrals, ions as well as radicals and metastables.

$$\left. \frac{dc_m(t)}{dt} \right|_{diss} = k_2 c_m(t) \underbrace{n_e}_{const.} \quad (1.36)$$

with c_m being the monomer concentration and n_e as electron density. Fragmentation of a monomer gas is a second-order process, but it appears as a pseudo-zeroth or a pseudo-first order process, as the electron density can be considered constant. In the first case, the plasma power is low (energy deficient regime) and monomer supply is not the limiting factor for fragmentation. The background of the energy-deficiency is a low (but constant) electron density, resulting in rates being small compared to the amount of monomer available. The second order formation becomes effectively a

pseudo-zeroth order process and the concentration increases linearly in time. In the second case, the monomer concentration decreases significantly due to consumption by fragmentation (monomer deficient regime). A pseudo-first order equation results.

In hydrofluorocarbon plasmas, the reactions of bound or unbound hydrogen with bound or unbound fluorine play an very important role. This is illustrated in Figure 1.3, where several extraction processes, leading to unsaturated bonds, are shown. One of the major products besides species with unsaturated bonds (which may oligomerize) is hydrofluoric acid (HF). Breaking of this and other molecules by electron impact (dashed arrows) results in plasma-parameter dependent formation of oligomer and finally polymer.

Such way, the chemical rates depend on the energy distribution of the electrons as well as the cross sections for dissociation of the considered molecule. For the particular case of CHF_3 , the rates are determined by help of numerical simulations in Section 3.2.3. The fragmentation of molecules in the plasma is opposed by recombination processes and branching reactions in the gas phase. As all kind of processes occur instantaneously, it can be sophisticated or even impossible to break down the kinetic pathways.

1.3.2.2 Chemical kinetics in the plasma presheath and sheath regions

In the plasma presheath and sheath regions of rf discharges, ions can have a strong influence on chemical processes. Compared to the plasma bulk, ions can only be accelerated in the electric field in the presheath to be able to exit the plasma bulk. For further details, see Section 1.2.3. The resulting high energetic ions can impact and fragment molecules in the gas phase close to the electrodes and sputter wall material or deposit.

1.3.2.3 Chemical kinetics on reactor walls

Surface processes differ from gas phase processes. Reactions which require a third body (like $\text{CF}_3 + \text{F}$ combination, (R 5)) can be enhanced at the chamber walls due to energy absorption by the wall material. Also physisorption (condensation, sticking) of molecules on the surface prior to chemical reaction can enhance the rates.

Reactions of surface atoms with plasma species can occur as well. In this case, the reaction kinetics are determined by the free active sites on

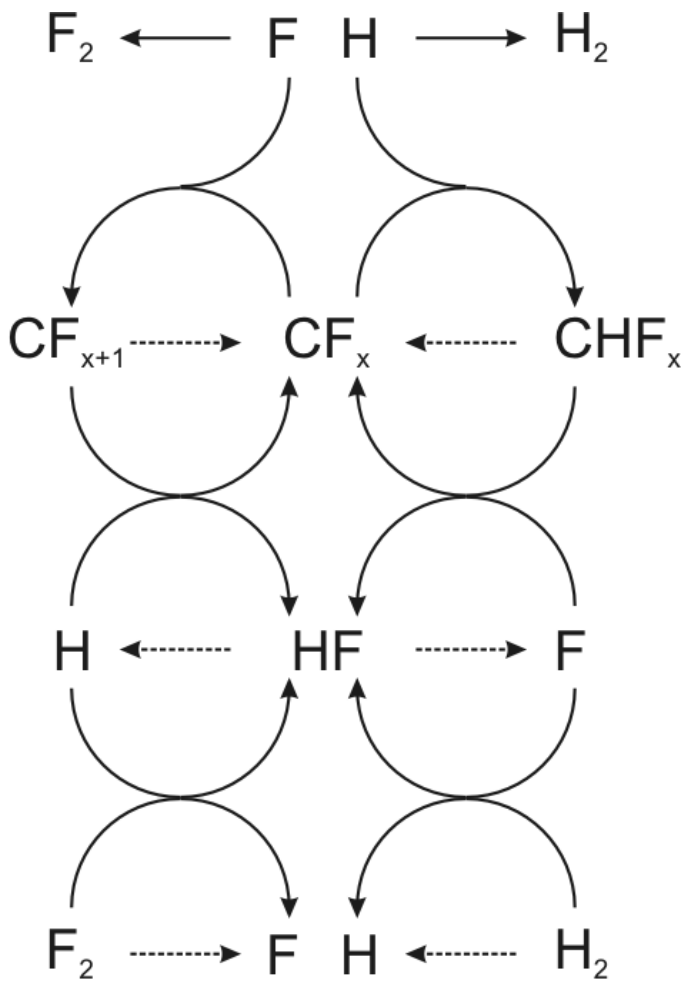


Figure 1.3: Reaction routes involving hydrogen and fluorine in hydrofluorocarbon plasmas. Solid lines: chemical reactions. Dashed lines: electron-induced dissociation processes. Both H- and F-atoms are responsible for abstraction of ligands from carbon, resulting in formation of the stable molecule HF and carbon radicals (here CF_x). The latter are a basis for macromolecule formation. After [15].

the surface. This type of reaction is in terms of adsorption terminology referred to as chemisorption. Physi- and chemisorption are macroscopically distinguished by the binding energy, which is commonly lower than 80-100 kJ/mol for physisorption.

The overall mass flux balance is

$$\Gamma_{\text{incident}} = \Gamma_{\text{adsorbing}} + \Gamma_{\text{bs}}, \quad (1.37)$$

where *bs* stands for directly backscattered particles³. Mass loss from the polymer due to sputtering or chemical release of molecules has to be considered as well:

$$\Gamma_{\text{adsorbing}} = \Gamma_{\text{polymer}} + \Gamma_{\text{released}}. \quad (1.38)$$

Here, Γ_{polymer} is the part of $\Gamma_{\text{adsorbing}}$ which results in the formation of stably bond polymer. It is calculated from the experimental deposition rate. Those particles which are released from the deposit during the polymer formation and reenter the gas phase are forming the flux Γ_{released} .

1.3.3 Fluorocarbon reactions

In fluorocarbon discharges, radicals can be formed either by electron impact dissociation and electron dissociative attachment (see Section 1.2.4), hydrogen or fluorine activated dissociation, atom transfer reactions and eliminations, further by collisions with ions, and by radiation. A survey of possible reactions is given in [9]. The reaction pathways for the production and reaction of radicals are manifold (see Section 3.3), therefore, only the processes traceable by the methods used in this work are discussed in the following.

1.3.3.1 Single-carbon radicals

Completely stripped carbon is created in fluorocarbon plasmas in comparable low amounts. It is traceable by optical emission spectroscopy.

A radical which is present in high amounts is CF (fluoromethylidene), having one dangling bond in its ground state. A reaction of it which is well studied is the reaction with atomic fluorine to form CF₂, which is a single step combination with a pressure dependent reaction rate, indicated by "M" which stands for the necessity of a third collision partner. Pressure dependent rate coefficients are herein given for a pressure of 80 Pa and were

³The backscattered molecules may be as well neutralized ions or fragments of incident species, which do neither physi- nor chemisorb.

calculated by the Troe formalism [12] with parameters given in the cited literature.



with $\Delta H^0 = -516.8 \text{ kJ mol}^{-1}$ and $k = 6.2 \times 10^{-15} \text{ cm}^3\text{s}^{-1}$ [13]



with $\Delta H^0 = -359.0 \text{ kJ mol}^{-1}$ and $k = 3.9 \times 10^{-12} \text{ cm}^3\text{s}^{-1}$ [4]



with $\Delta H^0 = -271.6 \text{ kJ mol}^{-1}$ and $k = 1 \times 10^{-12} \text{ cm}^3\text{s}^{-1}$ [13]



with $\Delta H^0 = -161.8 \text{ kJ mol}^{-1}$ and $k \approx 10^{-11} - 10^{-10} \text{ cm}^3\text{s}^{-1}$ (estimate in [4]).

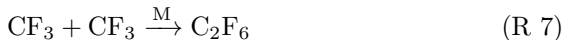
The next species in this series is CF_2 (difluorocarbene) which is discussed separately in the subsequent section. The series of single carbon radicals is completed by CF_3 , which is also highly reactive. It is a precursor of e.g. CF_4 , C_2F_5 , C_2F_6 . CF_4 is formed by



with $k_2 = 1.7 \times 10^{-12} \text{ cm}^3\text{s}^{-1}$ [14]. The reaction rate was found to be pressure dependent according to the literature. The reaction is highly exothermic ($\Delta H^0 = -544.5 \text{ kJ mol}^{-1}$). C_2F_5 results from



with a chemical rate of $k = 8 \times 10^{-13} \text{ cm}^3\text{s}^{-1}$ and $\Delta H^0 = -232.5 \text{ kJ mol}^{-1}$. Finally, C_2F_6 is produced e.g. by



with $\Delta H^0 = -407.8 \text{ kJ mol}^{-1}$ and $k = 2.1 \times 10^{-12} \text{ cm}^3\text{s}^{-1}$ [14].

1.3.3.2 Difluorocarbene

Carbene chemistry is an interesting field in organic chemistry due to the reaction paths of these molecules. They play an important role in the

chemistry of fluorocarbon plasmas and are often termed to be connected to oligomerization and polymer growth.

Carbenes are molecules in which the name-giving carbon atom possesses two single bonds and two unbound valence electrons. The binding partners can be atoms or molecules. Carbenes can possess very different reactivities, especially when the electronic ground states are compared. This is basically due to the fact that the two electrons can either be unpaired in a triplet state (spins parallel) or paired in one common orbital as a spin singlet state (antiparallel spins) [16]. Whether a spin triplet or a singlet is the energetically favored ground state is determined by the substituents. For example, ground state CH_2 is a spin triplet whereas CF_2 is a spin singlet. Besides the electronegativity of the substituent, also the size of the substituent is a deciding factor. The geometry of the carbenes differs as well, it is obvious that the triplet state is a sp^3 hybrid and the singlet state forms a sp^2 .

Though sometimes mistakenly stated, ground state CF_2 is therefore not a (bi-)radical at all. Nevertheless, singlets can undergo reactions as well and therefore, concentrations chemically diminish as well: as stated in the literature, difluorocarbene (singlet) is a reactive molecule [17, 18]. Besides high-rate reactions with radicals, it also adds e.g. to methyl substituted olefins (=alkenes) [19] as well as to perfluoroolefins. Chain extension reactions by addition of CF_2 to unterminated polymer chains are of high relevance for oligomer formation as found theoretically by Lau *et al.* for $(\text{CF}_2)_n$ chains [8]. The reaction enthalpy per CF_2 addition was constantly -203.8 kJ/mol, independent of the chain length. This was attributed to a lack of interaction of the chain with the bond formation occurring at the chain end. Such, chain extension by addition to unterminated molecules is of general relevance and one of the key processes in oligomer formation. Another important reaction is dimerization, which leads to the development of the (1,2)-biradicaloid $\cdot\text{CF}_2 - \text{CF}_2\cdot$ [20]. This molecule can further undergo extension reactions with difluorocarbene [8], or dimerize to tetrafluoroethylene ($\text{CF}_2 = \text{CF}_2$). The latter molecule was found to be highly stable, such that dimerization represents a terminal reaction under many conditions. The dimerization rate has been reported to be merely pressure dependent [17, 21, 22].

The dimerization rate coefficient is



with a chemical rate of $k = 4 \times 10^{-14} \text{ cm}^3\text{s}^{-1}$ [13, 23] in low pressure plasmas, and $\Delta H^0 = -291.9 \text{ kJ mol}^{-1}$ in general.

1.3.3.3 Ion-chemical reactions

In addition to the above radical-dominated chemistry, ion chemistry is taking place in discharges as well.

Cationic-anionic recombination can lead to the formation of reactive neutral species. In addition, ion-neutral reactions may take place. Therefore, several mechanisms play a role: besides collision-induced dissociation (CID), dissociative charge transfer (DCT) is of great importance, but also electron detachment (ED) can lead to fragmentation.

Some calculated reaction rate data according to Font *et al.* [24] are listed in Table 1.4 for reaction channels involving CF_x -neutrals.

Table 1.4: Ion reaction channels and rates

reaction	k_2
$\text{CF}_2^+ + \text{CF}_3 \rightarrow \text{CF}_3^+ + \text{CF}_2$	1.48×10^{-9}
$\text{CF}_2^+ + \text{CF} \rightarrow \text{CF}_3^+ + \text{C}$	2.06×10^{-9}
$\text{CF}_2^+ + \text{C} \rightarrow \text{CF}^+ + \text{CF}$	1.04×10^{-9}
$\text{CF}^+ + \text{CF}_3 \rightarrow \text{CF}_3^+ + \text{CF}$	1.71×10^{-9}
$\text{C}^+ + \text{CF}_3 \rightarrow \text{CF}_2^+ + \text{CF}$	2.48×10^{-9}
$\text{C}^+ + \text{CF} \rightarrow \text{CF}^+ + \text{C}$	3.18×10^{-9}
$\text{F}^+ + \text{CF}_3 \rightarrow \text{CF}_2^+ + \text{F}_2$	2.09×10^{-9}
$\text{F}^+ + \text{CF}_2 \rightarrow \text{CF}^+ + \text{F}_2$	2.28×10^{-9}
$\text{F}^+ + \text{CF} \rightarrow \text{C}^+ + \text{F}_2$	2.71×10^{-9}
$\text{C}_2\text{F}_4^+ + \text{F}^- \rightarrow \text{CF} + \text{CF}_2 + \text{F}_2$	8.20×10^{-8}
$\text{C}_3\text{F}_5^+ + \text{F}^- \rightarrow \text{C}_2\text{F}_4 + \text{CF}_2$	8.00×10^{-8}
$\text{CF}_3^+ + \text{F}^- \rightarrow \text{CF}_2 + \text{F}_2$	8.70×10^{-8}
$\text{CF}_2^+ + \text{F}^- \rightarrow \text{CF} + \text{F}_2$	9.10×10^{-8}
$\text{CF}^+ + \text{F}^- \rightarrow \text{CF} + \text{F}$	9.80×10^{-8}

Rate coefficients are given in cm^3s^{-1} .

Experimental data on ion-neutral reactions are only available at several stages of phenomenological observation up to tentative cross sections, see e.g. [24–26]. Especially the abundance and composition of neutrals has been, up to the authors knowledge, not yet been determined experimentally.

The relevance of these gas-phase processes to the present work is difficult to estimate. In the very most models, ion-neutral reactions are not considered. The error by doing so may be low, as the positive-negative ion recombination rate coefficients are commonly larger by almost two orders of magnitude. Due to the lack of experimental confirmation of the exact

reaction routes, the above ion-neutral processes were not considered in this study as well. Ion-ion recombination is well known [27, 28] and included in the chemical modeling in Section 3.3.

1.3.3.4 Ion-surface interactions

At the electrodes and walls, chemical rates of neutral reactions like recombination, oligomerization, and polymerization can be enhanced due to sticking or consumption of excessive heat of reaction. Reactions of adsorbed species are affected and promoted by ions: Neutralization processes at the electrodes can be of importance for the production of gaseous neutrals [29]. Ions can further enhance etching or polymer deposition. Besides the ion energy, this depends mainly on the electrode material or, in case of polymer deposit on the electrodes, the particular cross sections for ion-impact induced "activation"⁴ or dissociation. The enhancement of polymer deposition is mainly due to the creation of radical sites ("dangling bonds") [30].

1.3.3.5 Additional chemical reactions

In addition to the previous processes, argon metastables can induce dissociation as well. The rate coefficients are around $k = 4 - 8 \times 10^{-5} \text{ cm}^3/\text{s}^{-1}$ [31]. Argon metastable densities can be quite large and this dissociation channel can become important.

Neutral-neutral collision-induced dissociation is possible as well. A theoretical study on argon collisions with CF_4 resulted in significant dissociation processes with a threshold of $E_{kin} = 6 \text{ eV}$ [32]. Fast neutrals can result e.g. from ion-ion recombination.

⁴Term often used for creation of radical sites on surfaces.

Chapter 2

Experimental setup and measurements

2.1 Plasma reactor and measurements of the electrical discharge parameters

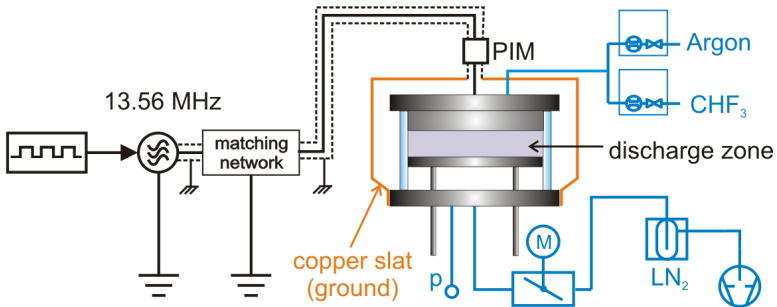


Figure 2.1: Plasma setup as used for the experiments, not true to scale.

One of the plasma setups used is shown in Figure 2.1. The glass cylinder in this figure is simplified as the four flanges, allowing to attach optical windows, Langmuir probes, etc., are not shown. The gas was supplied via mass-flow controllers attached to a MKS 647c multigas controller and equally distributed via a shower-like distributor. The exhaust gas was pumped out via a cooling trap and a rotary vane pump. The pressure was measured with a MKS 626 pressure transducer (baratron type). The pressure was regulated by a butterfly valve which was automatically controlled by a MKS 651c pressure controller. The power was supplied by a 600 Watt Dressler Cesar 136 rf generator with a 13.56 MHz sinus exit waveform in combination with a Dressler VM 1500 AW impedance matching network. In order to further eliminate disturbances by reflections and standing waves of overtones between the matching network ("matchbox") and the reactor, a rf pass and blocking filter (Manitou Systems, suppression of frequencies

> 13.56 MHz) was placed at the exit of the matchbox (not shown in the figure). By external triggering of the rf generator, rectangular envelopes of the radio frequency down to the microsecond range can be obtained. The lower electrode was grounded via 4 copper slats arranged in 90° against each other with respect to the symmetry axis of the reactor. Voltage, current, and impedance were probed by a UI probe¹ (Scientific Systems Plasma Impedance Monitor, PIM). As UI probe measurements can be corrupted by large stray electric fields, the discharge voltage was additionally checked by a high-voltage probe (Tektronix P 6015, 1000x) attached to a digital oscilloscope (Tektronix TDS 3032 B). Electron density measurements were performed with a Plasma Consult MWI 2650 microwave interferometer. Therefore, sender and receiver were placed in horizontal line-of-sight arrangement parallel to the electrodes, passing the microwave through the center of the discharge. In addition, the optical emission in the UV range was measured line-integrated along the axial direction of the plasma reactor. Such, the electron density distribution within the discharge can be estimated.

Table 2.1: Variables for plasma experiments

name	var.	range	sc	unit
Ar flow	F_{Ar}	60	60	sccm
CHF_3 flow	F_{CHF_3}	5-15	10	sccm
power	P	5-35	20	W
pressure	p	60-100	80	Pa
pulse per.	T	0.1-1000	100	ms
duty cycle	dc	10-100	35	%

sc - value under standard conditions

In general, to study the kinetics of particles in the discharge and the discharge characteristics, several parameters were varied as listed in Table 2.1. **In the whole subsequent text, the value of a variable is the one listed under standard conditions in the table, if not explicitly noted differently.**

For the electrical and optical measurements, a setup with an electrode diameter of 29.8 cm was used. For mass spectroscopy, a similar arrangement with electrodes of 20 cm in diameter was used. The discharge gap d (spacing between the electrodes) was 45 mm in both cases. In the subsequent paragraphs, cylindrical coordinates according to Figure 2.2 are used.

¹syn.: VI probe

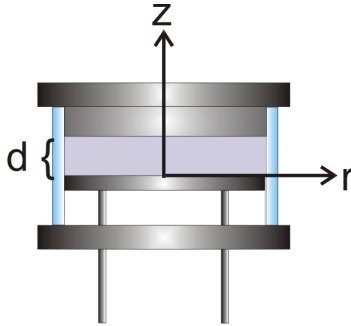


Figure 2.2: Geometry of the plasma setups used for the experiments, not true to scale.

2.2 Laser-induced fluorescence

2.2.1 Setup of LIF

Laser-induced fluorescence is one of the most important tools in plasma diagnostics. This technique allows to determine the absolute concentrations of transient and stable species with an excellent spatial and time resolution. Contrary to line-integrated methods such as UV, Vis, or IR absorption, real three-dimensional density measurements can be carried out. Two different setups are technically realized: conventional crossed-beam setups and acquisition techniques allowing to obtain two-dimensional fluorescence images.

- The conventional crossed-beam technique, using a focused laser beam and a detection device with zero-dimensional resolution (e.g. a photomultiplier tube) is still the most applied method as it requires low-cost components. The detection is either performed directly by collecting the fluorescence light and focusing it to the entrance of the detector, or after dispersion through a spectrometer. In the latter case, the molecule can be identified by its characteristic spectral emission pattern by comparison to calculated spectra. However, this technique has several disadvantages: studies of anisotropic density distributions require to carry out complete acquisition series in each position. In addition, the movement of optical components can falsify the results, as this setup is extremely sensitive to misalignment. This affects both scans in variable positions as well as scans with variable excitation wavelengths (movement of mirrors, beam splitters etc. in the laser).

This problem can be only overcome partially by measurements with a calibration gas.

- Planar laser-induced fluorescence allows the investigation of highly nonuniform radical and metastable distributions in e.g. fluorocarbon discharges [33–38]. In this case, the laser beam is broadened and the fluorescence emission of the excited species is collected by a camera. Although it is the most complete setup for spatial resolution, the amounts of data are too large to be evaluated when systematical parameter studies are performed.

As a compromise between these two techniques, linear laser-induced fluorescence² (LLIF) was used in this work. As common, the laser and the detection system were aligned perpendicular to each other. The laser beam was coupled into the recipient through quartz windows in Brewster angle. Laser excitation was carried out with a NdYAG pumped OPO³ laser system (Ekspla NT 342-1-UV). The laser emission can be tuned between 210-380 nm and 420-2300 nm with a line width (fwhm) $\Delta\lambda < 5 \text{ cm}^{-1}$. The emission is pulsed with a pulse duration of 6 ns at 10 Hz maximum repetition rate. The laser pulse energy depends on the wavelength as well as on the pumping energy from the NdYAG. In the UV emission range which was mainly used, between 0.3 and 1 mJ are emitted per pulse⁴.

The fluorescence light was detected through a quartz window by means of an intensified CCD (ICCD) detector, see Figure 2.3. Therefore, an Andor iStar 734 generation II with 1024x1024 pixels was used in two ways: First, attached to a 750 mm Dong-Woo spectrometer, second, in imaging mode with a quartz lens objective (Nikon UV Nikkor, 105 mm). In front of the objective, a UV transmission filter (UR-2) was attached to reduce the background signal originating from the plasma emission. The detection time (gate width) was 30 ns. Such, the fluorescence emission was about 1-2 orders of magnitude larger than the plasma emission. The starting point for data acquisition was chosen to be shortly after extinction of the laser emission. This was controlled via the detection delay in the ICCD, which allows to shift the detection time frame relative to the trigger signal coming from the laser with a 25 ps resolution between 0 ns to 25 s.

²This term refers to the detection and not to the laser excitation regime.

³OPO-optical parametric oscillator

⁴In pulsed systems, it is common to measure the energy submitted per pulse instead of power for obvious reasons.

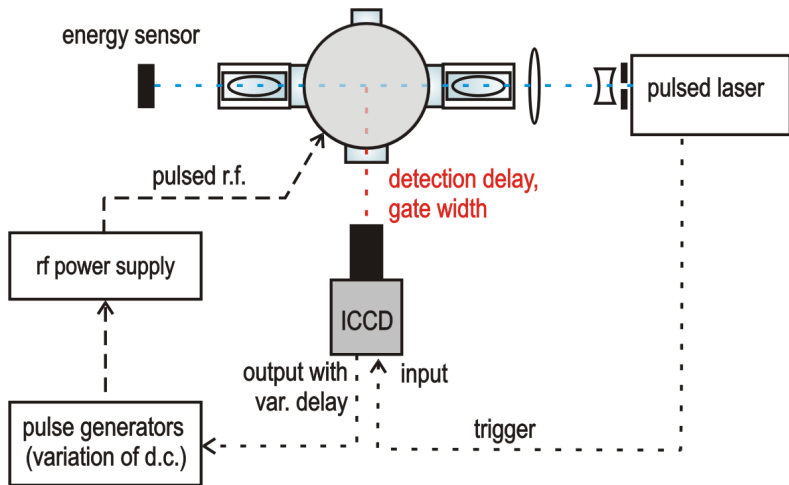


Figure 2.3: Setup as used for LIF. The picture shows direct fluorescence detection in the camera mode. For the spectral resolution mode, a spectrometer is attached to the ICCD. Lens and aperture systems allow to control the beam width and beam intensity.

To perform measurements within a plasma pulse, the trigger output (output A at the camera) allows to generate trigger pulses with trigger delays Δt between 0 ns and 25 seconds with a 16 ns resolution. The trigger pulse, coming from the ICCD with a fixed length in the nanosecond range, had to be adopted to the required plasma pulse length. This was done in two steps. First, the pulse was transformed from the nanosecond range to the hundred-microsecond range by a positive-flank triggered PM 5715 pulse generator (1-50 MHz, Philips). The output signal of the PM 5715 was used to trigger a PM 5716 pulse generator (1-50 MHz, Philips), generating long trigger pulses in the range of milliseconds to seconds⁵.

With the objective, PLIF images can be acquired (see Figure 2.4). It is seen from the fluorescence signal (bright stripes) that the investigated plasma species are laterally equally distributed in the center of the reactor, i.e. $I(r, z) = I(0, z)$. This way, the LIF measurements can be reduced to one dimension without loss of relevant information, so full-horizontal binning was used for the subsequent density measurements. In this way,

⁵Without the pretransformation step, the electronics of the pulse generators failed to create such long pulses due to the extreme difference between trigger pulse length and desired output.

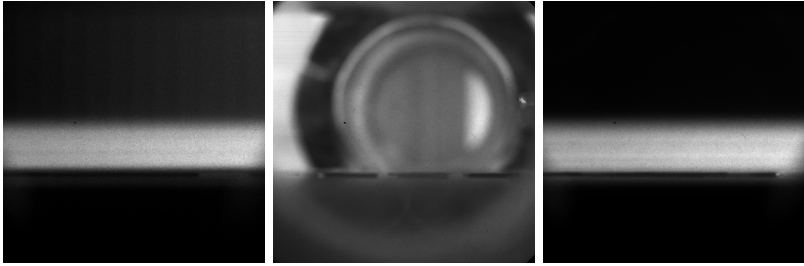


Figure 2.4: Middle: ICCD view insight the reactor. For orientation: On the lower electrode, three samples can be seen. The upper electrode is not in the field of view. Same field of view: left: the CF fluorescence within the laser beam (here: covering about $1/4$ of the discharge gap d) is seen as bright area. Right: CF₂ fluorescence. The fluorescence signals are laterally highly uniform.

the densities along the reactor axis (z -axis) were obtained (LLIF).

For the calibration of the LIF intensity and density, two methods are applied most often. One is the calibration by absorption measurements, which is possible as long as the absorbance is large enough and the absorption coefficients of the investigated molecules are known [39, 40]. The second method is based on comparative LIF measurements with an isoelectronic stable species. In case of CF, NO is used for this purpose [41]. In case of CF₂, benzene can be used [4]. In addition, correction curves for the axial profiles have to be determined by scanning the density with another method, e.g. the conventional crossed-beam technique.

The procedures applied for calibration are described in detail in Sections 2.2.2 to 2.2.4.

2.2.2 Calibration of CF densities

In order to obtain the CF density, UV absorption measurements [39] as well as comparative LIF experiments with NO [41] were carried out in the past. Both methods require quantum-mechanical simulations of the rovibrational spectrum and the transition probabilities. In this work, attempts to determine the absolute density of CF failed as the absorption was too low. For this reason, the LIF method had to be adopted to the LIF laser setup which was used.

2.2.2.1 Background of the calibration method

In the literature, calibrations by comparative LIF measurements with NO were carried out by Cunge *et al.* [41], using a dye laser system and performing calculations of the rovibrational LIF spectra. By the Equations (2.1) to (2.3), which are deduced from the equations in [41], the number density of CF can be calculated from the NO density. The fluorescence emission is given by

$$I_{em} = K(\lambda_A)R_A(\lambda_A)F_A(laser)N_A, \quad (2.1)$$

where K is the detection efficiency (given by the optical setup as well as the detector quantum efficiency), λ_A is the detection wavelength, and R_A is the fluorescence branching ratio for this specific wavelength. N_A is the number density of the detected species. When an integral measurement of the fluorescence emission spectrum is carried out, the branching ratio can be omitted and (2.1) becomes

$$I = KF_A(laser)N_A. \quad (2.2)$$

For single-wavelength excitation, the density ratio of a species A in the state a and species X in the state x is then given by

$$\frac{N_A}{N_X} = \frac{K(\lambda_X)R_X(\lambda_X)F_X(laser)I_A}{K(\lambda_A)R_A(\lambda_A)F_A(laser)I_X}, \quad (2.3)$$

This can be further simplified by normalizing the spectral response of the detection system K . The term $F_A(laser) \propto B_{\nu}^{\prime\prime} I_l(r, t)$ describes the excitation efficiency. It is a function of the excitation rates, given by $B_{\nu}^{\prime\prime} I_l(r, t)$, the Einstein coefficient for absorption times the laser intensity, and depends on several parameters. For pulsed lasers as used in LIF, the excitation efficiency is commonly described as a function of the laser emission energy per pulse, which is $E = \int I_l(r, t)dt$, instead of using the laser intensity. Three excitation regime can be distinguished: a linear regime of excitation where $F_A \propto E$, a regime of incoherent saturation ($F_A \propto \sqrt{E}$), and a regime of coherent saturation (i.e. F_A is nearly independent from the laser intensity). Experimentally, the regime of excitation is determined by varying the laser emission energy. In the present work as well as the work of Cunge *et al.* [41], the regime of linear excitation was chosen ($F_A \propto E$).

Cunge *et al.* [41] measured the fluorescence emission resulting from excitations of chosen, identical rovibrational states in the isoelectronic gases

CF and NO by excitation of a narrow-band dye laser system. By doing so, the branching ratios became identical, and Doppler profiles of the levels were identical as well. The density calibration was then carried out for $F_A = F_X$.

With an OPO laser as used here, the method of single state excitation is not applicable. In contrast to most dye lasers used, OPO laser systems emit laser beams with a much broader line width of about 5 cm^{-1} , which exceeds the line width of a single rotational transition, and further exceeds the spacing between rotational transitions in CF and NO. Such way, excitation occurs from multiple levels instead from a single rotational level. The transitions are convoluted by the spectral line profile of the OPO laser beam. Convolution is generally given by

$$(f * g)(t) = \int_D f(t - \tau)g(\tau)d\tau \quad (2.4)$$

for the one-dimensional case (see [42, 43]). In the present application, the convolution function f is the line profile, which is Gaussian, and g is the distribution of the rotational states. D is the domain of the functions. By integrating the above function over t , one obtains

$$\begin{aligned} \int_{-\infty}^{\infty} (f * g)(t)dt &= \int_{-\infty}^{\infty} \int_D f(t - \tau)g(\tau)d\tau dt & (2.5) \\ &= \int_{-\infty}^{\infty} \int_D \frac{1}{\sigma\sqrt{2\pi}} e^{-\frac{(t-\tau)^2}{2\sigma^2}} g(\tau)d\tau dt \\ &= \int_D g(\tau) \underbrace{\int_{-\infty}^{\infty} \frac{1}{\sigma\sqrt{2\pi}} e^{-\frac{(t-\tau)^2}{2\sigma^2}} dt}_{=1} d\tau. & (2.6) \end{aligned}$$

In other words, the area under a complete transition band is conserved when it is convoluted by a normalized function. Such, for a OPO system, it is disadvantageous to scan a small range of rotational levels within a vibrational state under these circumstances, as slightest deviations from the spectral Gaussian beam profile or a wavelength mismatch can hardly be identified, and Einstein coefficients for absorption can differ by one order of magnitude when rotational levels are considered. Instead, the precision can be enhanced significantly by scanning a whole vibrational band and comparing the integral intensities according to (2.6). Here, a broad laser line profile is advantageous because the scan of a range of 3 nm can be accomplished with approximately 30 acquisitions. The Einstein coefficients for absorption

of the rotational levels are convoluted as well and can be averaged to one single Einstein coefficient for the whole vibrational transition for each CF and NO. Then, as CF and NO are isoelectronic, and LIF excitations occur from the ground state under the present conditions, it is possible to calculate the relative numbers of electrons by comparing the integral excitation scans for $F_A = F_X$ within the same LIF regime as long as e.g. saturation effects are avoided. For the calculation of the density, the population of the vibrational states must be known, which is also the case for the method of Cunge *et al.*

With both methods, the $B_{\nu''}^{\nu'}$ need to be known as well. In the present work, the database of the spectral simulation program LIFBASE 2.0.60 [44] was used. LIFBASE allows to simulate absorption and emission spectra, also under LIF excitation, and further to include the effects of line broadening, saturation, and thermal and non-thermal population distributions. Here, the software was used to simulate excitation scan spectra of the $A - X(0, 0)$ and $A - X(1, 0)$ bands of CF and NO, respectively. The input parameters of this simulation are shown in Table 2.2. The overall simula-

Table 2.2: Input parameters for LIFBASE

parameter	value
instrumental resolution in Å ^a	0.5
lineshape	Gaussian
T in K	300
gated detection ^b	total integration
fluorescence detection ^c	full
LIF regime ^d	linear

a: fwhm of laser beam

b: time frame for detection

c: spectral range of detection

d: as determined from measurements

tion of the fluorescence emission spectrum only shows transitions from the vibrational ground state occur at 300 K as expected (Figure 2.5).

The method of the integral measurement has several advantages:

- Compared to single line comparative measurements, the problem of line-splitting due to spin-orbit coupling is not present in the integral measurement. Furthermore, the population of electrons in different rotational states due to thermal excitation, which always requires fur-

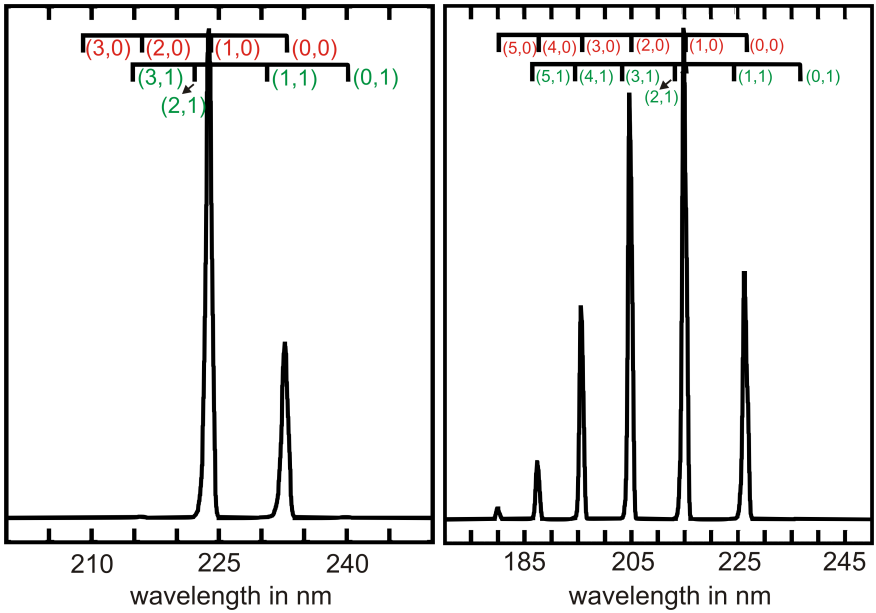


Figure 2.5: Calculated excitation scans in CF (left) and NO (right), obtained with LIFBASE. Calculation parameters see Table 2.2.

ther investigation of the temperature distribution, has much less influence due to the integration over the whole band, as it involves the complete number of electrons in the ground state. Furthermore, a mismatch of the laser excitation wavelength has no effect at all.

- Compared to a broad band excitation, the power input can be much better controlled in the whole range of excitation wavelengths and saturation effects as well as cascading can be avoided.

2.2.2.2 Calibration of the CF density

Experimentally, the CF fluorescence signal was measured upon variable excitation wavelength in the range from 222 to 224.5 nm with 0.1 nm resolution. The transition $A - X(1, 0)$ between the ground state $A^2\Sigma$ and the excited state $X^2\Pi$ was induced by that way. The spectral fwhm of the laser beam was $\Delta\lambda = 0.5$ nm. In addition, the excitation energy was varied to find the regime of linear excitation efficiency. For the calibration measurement, NO was let in the reactor without any discharge. The excitation wavelength was varied and the $A - X(0, 0)$ transition of NO between 225 and 227.5 nm was scanned.

The spectra are shown in Figure 2.6 for CF and NO. The laser excitation regime is linear as seen by the laser-intensity normalized emission signals which are identical for both laser energies. Deviation of some data points in the NO spectrum at the left end are due to changes in the alignment in this measurements mode (see Section 2.2.4). The simulated spectra from LIFBASE were then put to an absolute intensity scale and integrated. With the Einstein coefficients for absorption, $1.414 \times 10^{10} \text{ m}^2\text{J}^{-1}\text{s}^{-1}$ for CF $A - X(1, 0)$ and $1.081 \times 10^9 \text{ m}^2\text{J}^{-1}\text{s}^{-1}$ for NO $A - X(0, 0)$, the density of CF under standard conditions at the end of the plasma-on time was obtained. This was done by comparing the integral emission intensities of both molecules, each normalized to the laser energy per pulse as shown in Figure 2.6 and using $F_{CF} = F_{NO}$ in Equation (2.3). Such, the density of CF resulted to $3.3 \times 10^{12} \pm 10\% \text{ cm}^{-3}$.

2.2.3 Calibration of difluorocarbene densities

2.2.3.1 Background of the calibration method

Absorption measurements are commonly used as a complementary technique to LIF measurements as it provides absolute species concentrations.

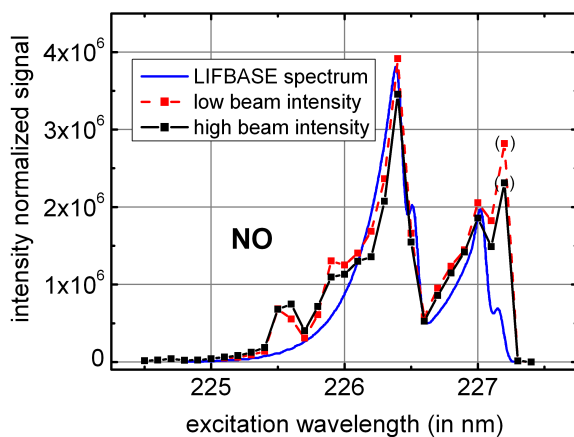
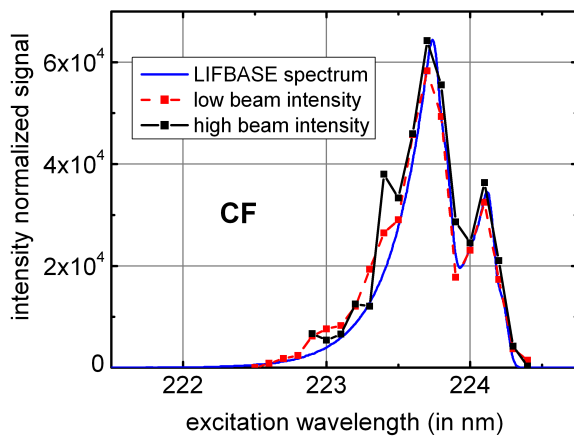


Figure 2.6: Excitation wavelength scans of CF (top) and NO (bottom) at low and high laser beam intensities. The data were acquired in spectral mode; deviations from the fit are due to changes in the optical pathway. The LIF regime is linear.

In this case, the absorption of photons by molecules is measured. Depending on the species, these measurements are usually performed in the electromagnetic spectrum ranging from microwaves [45] over IR [46] and Vis to the UV region [40, 47, 48].

Absorption is described by the extinction law according to Lambert-Beer:

$$I(\lambda) = I_0(\lambda) \exp(-\sigma Nd) \quad (2.7)$$

$$\rightarrow N = \ln \frac{I_0(\lambda)}{I(\lambda)} \frac{1}{\sigma d} \quad (2.8)$$

Therefore, the absorption cross sections σ must be known. With advanced modeling, involving the molecular constants, also the vibrational and, in case of high temperatures within the plasma, the rotational temperature of the species can be determined [40] from the band structure and the vibrational line width, respectively.

2.2.3.2 Difluorocarbene density calibration by absorption

For the CF_2 absorption measurements, UV light from a Hereaus deuterium lamp was collimated and transmitted through the plasma recipient. The transmitted light was collected on the opposite side with a lens focused to a quartz optical fiber and detected with the ICCD after dispersion in the spectrometer. In the experiments, a grating with 300 lines/cm was used. The gate width of the ICCD was commonly 100 μs , allowing to resolve the temporal development of the metastable species in pulsed discharges with a high time resolution. In addition, the whole UV/Vis range was scanned for extinction by other species. It turned out that only the extinction by CF_2 had a measurable effect in the transmission spectrum.

In the UV region, the typical absorption bands of CF_2 appear which are shown in Figure 2.7. For the determination of absolute densities from the absorption, the absorption coefficients from King *et al.* [47], Sharpe *et al.* [48], and Bulcourt *et al.* [40] were taken into consideration. King *et al.* published absorption spectra and Franck-Condon factors based on experimental data in 1979, followed by Sharpe *et al.* in 1987 who published experimentally determined absorption cross sections. Bulcourt *et al.* performed additional *ab-initio* calculations in order to theoretically substantiate and/or correct the previous publications. The absorption spectra of the latter two publications looked slightly different for reasons as discussed in [40], whereas a

good agreement to King’s data concerning the envelope was found.

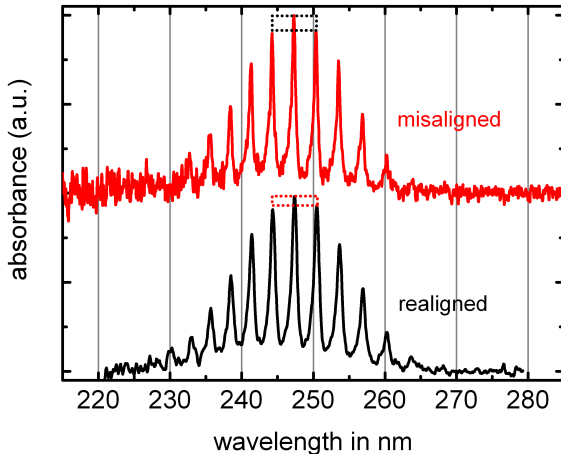


Figure 2.7: Difluorocarbene absorption spectra showing the effect of realignment, see marked region of interest.

In the present case, in some experiments (red curve in Figure 2.7), spectra looked like those measured by Sharpe *et al.* [48]. In the marked region of interest, one can see that the relative height of the maximum peak differs from the relative height seen in the black curve. On a first glance, this might be interpreted as different distributions of the vibrational temperature. The optics, however, turned out to have been slightly misaligned in case of the first case, such that the optical path for measurements with and without plasma inside the reactor differed. This is due to the diffracting optical properties of the plasma. After realignment, spectra as depicted in Figure 2.7, black line, result. This data can be fitted by the cross sections published in the newer work of Bulcourt *et al.* [40]. From the apparent vibronic structure it can be concluded that the vibrational temperature of the observed states, T_{vib} , is in thermal equilibrium at about 300 K. The absorption peak shapes, which consist of convoluted rotational transitions, were not fitted. It was found, however, that the relative peak heights as well as the fwhm of the absorption peaks remained invariant if spectra were acquired in pulsed discharges (standard conditions) at different stages of the plasma pulse, including the off time. Such, the vibrational as well as the

rotational temperature are constant, and both are therefore assumed to be at room temperature.

A background continuum is observed especially in the black spectrum, which was observed and discussed in the literature as well. In the present work, by means of high resolution scans, this offset could be removed (as exemplary shown in Figure 2.7, red curve). Such, in this work, the background continuum can be attributed to overlapping lines when the resolution is insufficient. Again, as convolution conserves peak areas (Equation (2.6)), the low-resolution measurements are sufficient for density measurements under present conditions. This allows a significant reduction of the acquisition time for studies of density developments in pulsed discharges.

Finally, the CF_2 density in the center of the reactor was measured to be $7.9 \pm 0.6 \times 10^{13} \text{ cm}^{-3}$.

2.2.4 Calibration of the density profiles by LIF

Linear laser-induced fluorescence requires image calibration. This is due to the optical setup, starting from the laser-beam profile over to lens systems and windows as well as the ICCD pixel sensitivities. Once calibrated, raw data can be directly converted to density profiles (see Section B).

Two methods were realized to obtain density profiles, both are based on the conventional crossed-beam LIF technique. Therefore, the excitation laser beam was reduced to <3 mm in diameter and height-scanned across the axial z -direction of the discharge chamber through the center of the reactor ($r=0$). The optical setup was kept fix and the reactor was moved relative to the optics. In one series of measurements, fluorescence spectra were acquired at each position by the ICCD camera attached to the spectrometer. In the second series, the fluorescent molecules were imaged with the ICCD camera directly via the objective.

The first method of acquisition, further referred to as the spectral mode, allows to identify the species by the specific emission spectrum. As a disadvantage, it is extremely sensitive against changes in the alignment and can further not distinguish between direct and reflected fluorescence emission. This is especially problematic when measurements close to the electrodes are performed⁶. The second method, referred to as the imaging mode, does not allow the identification of the emitting species. But this is not of importance as long as the excitation wavelengths are chosen such that only one

⁶For this reason, many authors do not inform about the densities closer than a few millimeter to the electrodes, or take a mathematical interpolation.

species is excited at once. The method is further insensitive against changes in the optical alignment and, in addition, reflections from the electrodes or other components can be easily identified. This way, the scanning of the densities close to the electrodes can be performed with high precision.

For a density profile calibration, the optical transmission efficiency of the reactor optics needs to be corrected. This was done by filling the reactor with nitric oxide and performing height scans without plasma excitation. The resulting emission yield the normalization curve for the optical transmission. Second, a calibration plasma is ignited producing the species of interest. Height scans are then performed for these species, which, together with the optical correction curve, yield the density distribution.

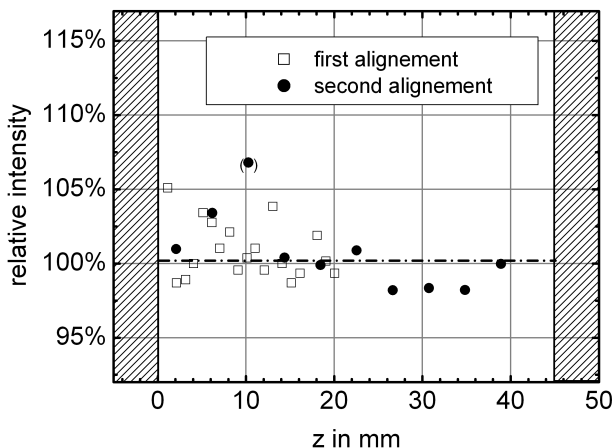


Figure 2.8: The density calibration profile of the CF radical as obtained in the fluorescence imaging mode. The data were acquired under standard conditions.

The CF density profile after calibration is shown in Figure 2.8. Here, only data from the imaging mode are shown as the spectral mode data showed more uncertainty. As can be seen, the profile is nearly flat, CF is equally distributed along the z-axis.

For CF_2 , the results of a corrected height concentration profile as measured in spectral mode is shown in Figure 2.9. Here, excitation scans were carried out at three different wavelength, 234 nm, 234.3 nm, and 261.5 nm. By doing so, the transitions around $A - X(0, 11, 0)$ and $A - X(0, 1, 0)$ were

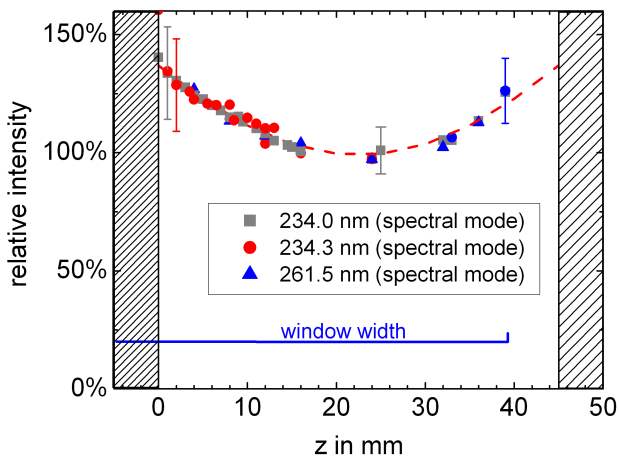


Figure 2.9: The density profile of CF_2 as obtained in the spectral mode. The data were acquired under standard conditions.

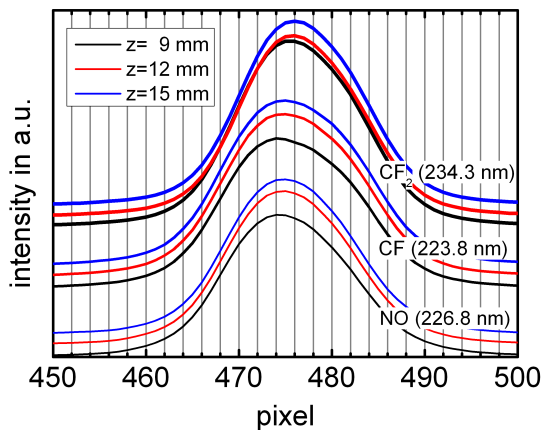


Figure 2.10: Effect of excitation wavelength and axial position of the beam on the envelope of the measured signal (imaging mode). Notice the drift especially of the center maximum.

excited. The absolute calibration error from the spectral mode data is large. It turned out that even though the axial position was not changed during the calibration measurements unless all examined species were scanned, a permanent realignment for each species and position would have been necessary. The discrepancy between the laser beam positions in dependence of wavelength and reactor height is illustrated in Figure 2.10. In this figure, the imaged profiles at different axial positions and for different excitation wavelengths (exciting CF_2 , CF , or NO) are shown. In the ideal case, as the laser and the camera are both not moved relative to each other, the position of the fluorescence image on the camera chip should be invariant. It is, however, seen that the center positions of the beam images slightly move, which is due to changes in the pathway of the detection system. Furthermore, in the ideal case, the position of the beam image on the camera chip should not depend on the excitation wavelength. But here, a dependence on the excitation wavelength is observed by excitation of the different molecules. This can be mainly attributed to changes in the optical pathway of the excitation system, namely mirrors, beam splitters, BBO crystals, and the OPO in the laser. Due to these effects illustrated in Figure 2.10, an error of about 10 % resulted per 5 mm when performing height scans in the spectral mode. Such, realignment was necessary each 5 mm to correct differences in the optical pathway from the windows etc..

In the imaging mode (Figure 2.11), the absolute error was much lower in the range of about 2% in the plasma bulk. At the electrodes, some uncertainty arises due to grazing incidence and the error is about 5%. Again, the excitation scans were carried out at 234 nm, 234.3 nm, and 261.5 nm to excite the transitions around $A-X(0, 11, 0)$ and $A-X(0, 1, 0)$. The obtained profiles were identical.

For comparison of both calibration methods, the results are both depicted in Figure 2.12. The profiles obtained in the imaging mode provides higher precision, so the data were adopted for the calibration, whereas spectral data were discarded.

2.3 Mass Spectrometry

Quadrupole mass spectrometry (QMS) is a technique which is often used to study the production of species in a plasma. Ionized mass fragments are detected by mass dispersion in a complex quadrupole field. The ions can be either extracted from the plasma or are produced in the mass spectrometer

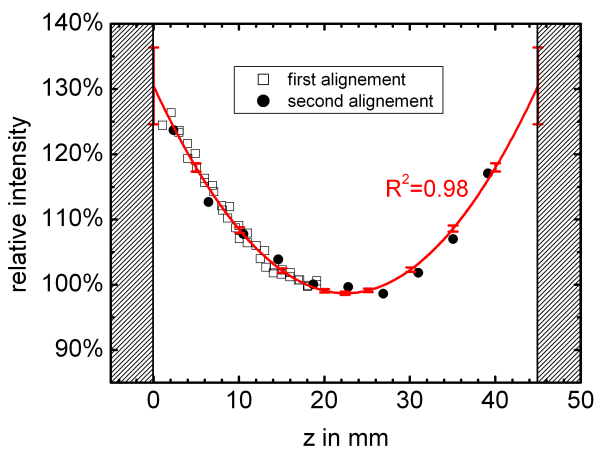


Figure 2.11: CF₂ density profile as obtained in the imaging mode. The data were acquired under standard conditions at the end of the plasma-on time.

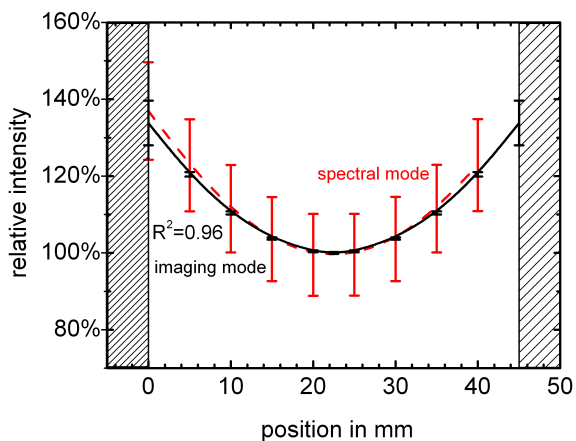


Figure 2.12: The concentration profiles as obtained in the fluorescence imaging mode (black) and the spectral mode (red). The data were acquired under standard conditions at the end of the plasma-on time.

by electron-collision induced ionization or electron attachment within the mass spectrometer.

In fluorocarbon plasmas, mass spectrometry has been applied by many groups. Besides measurements accompanying optical methods [49, 50] and detection of large molecules by attachment mass-spectrometry [51–54], intensive studies of radical formation were carried out as well [54], using threshold-ionization measurements. The fact that radicals mostly possess lower threshold energies in their cross sections is used in this case. In the present work, molecules were extracted by pumping through an orifice and subsequently ionized in the mass spectrometer.

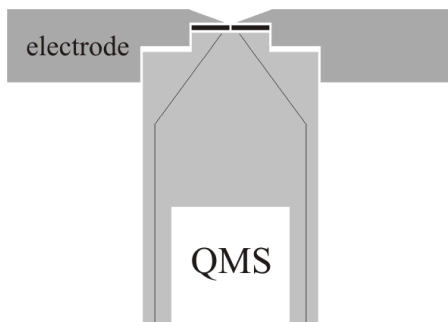


Figure 2.13: Schematic setup of mass spectrometry. The MS is attached to the lower, grounded electrode of a parallel-plate reactor. The orifice is $50\ \mu\text{m}$ in diameter.

The scheme in Figure 2.13 shows the arrangement which was used. A quadrupole mass spectrometer (QMS, type HAL IV, Hiden, 300 amu scan range) was attached to a parallel plate reactor. The orifice of the Pt aperture had a $50\ \mu\text{m}$ diameter and was positioned in the center of the grounded electrode of the reactor. The mass transmission efficiency of the orifice was not measured. The QMS was pumped by a turbomolecular pump and heated continuously to 360 K in order to reduce condensation at the walls. For ionization of the incident particles, a fixed electron energy of 70 eV was applied. The ions were detected with the Faraday cup.

2.4 Characterization methods for plasma polymer

The thickness was measured with a Sentech SE 801 spectroscopic ellipsometer within a wavelength range of 280-850 nm. The fitting of the data was carried out with a Cauchy model of the surface optical parameters.

For the determination of the surface tension⁷, contact-angle measurements were performed with four different liquids, bi-distilled water, benzyl alcohol (>99%, Merck Schuchardt, Germany), di-iodmethane (>99%, Aldrich Chemie, Germany), and 1-bromonaphthaline⁸ on a home-build contact-angle measurement setup. The surface tension was calculated by the solving Young's equation according to the Owens-Wendt method [56]. Care was taken that the minimum drop base diameter was at least 5 mm to assure the validity of the data [57].

The chemical composition of the polymer film was measured by x-ray photoelectron spectroscopy (XPS) on an Axis Ultra spectrometer (Kratos Analytical Ltd., GB). The samples were irradiated with monochromatic Al K $_{\alpha}$ radiation (1486.6 eV, 140 W). Low-energy electron flooding was used for charge compensation during scanning to prevent or at least reduce charging: charging occurs on insulating substrates due to the loss of electrons by photoemission⁹. Detail scans were acquired for each element with a pass energy of 40 eV in 0.1 eV steps at a take-off angle of 90°. The resolution of the spectrometer is about 0.71 eV fwhm for Ag3d5/2 under these conditions. A detailed deconvolution of the Si2p, C1s, O1s, and F1s photoelectron spectra was carried out with the program CasaXPS ver. 2.3.14. Therefore, all spectra were calibrated relative to the aliphatic C1s component at 284.6 eV in accordance with the other elemental peak positions of oxygen and silicon. Spectra were interpreted according to the literature [61–65].

In order to study inherent chemical reactions within the polymer film,

⁷The identification of Gibbs or Helmholtz free energy per unit area, or (free) surface energy per unit area with the surface tension, is strictly speaking incorrect for multicomponent systems according to Ip and Toguri [55]. For data resulting from contact-angle measurements in this work, the correct term surface tension is used. When referring to literature, the authors' term will be used.

⁸The data of 1-bromonaphthaline was later omitted as it turned out that a reaction/decomposition at the surface took place.

⁹Otherwise, differential charging may result, especially on samples with different local conductivities (like partially coated surfaces in this work), and accordingly, the photoelectron emission energies of the same chemical bond differ depending on their origin [58–60].

electron spin resonance/electron paramagnetic resonance (ESR/EPR) measurements were carried out with a Magnetech Miniscope MS 200 spectrometer (X-Band, lower limit 10^{11} spins).

Chapter 3

Modeling of the plasma

This chapter contains several stages of plasma simulations.

In Section 3.1, electron-molecule interactions are simulated and discussed. This includes the determination of the EEDFs as well as the electron density. Rate coefficients for neutral dissociation, ionization dissociation, and attachment are determined. In addition, the electron mobility as one of the most important variables in modeling is obtained from the simulation. The effect of variable cross section data sets and other input variables is discussed as well. The results of this section are used for the subsequent plasma particle dynamics simulation in Section 3.2.

In Section 3.2, the electrical parameters of a plasma are modeled. Those parameters include e.g. the mean electron energy, which, at the end of the section, is used to calculate the electron-molecule interaction rates in dependence of the plasma power.

3.1 Modeling of electron-molecule interactions with BOLSIG+

As stated in Section 1.2.4, the dissociation of molecules by electron-impact is strongly depending on the EEDF. A very coarse approach is commonly carried out by assuming a Maxwellian distribution of the electron energy; a refined approach is that of using a Druyvesteyn distribution. But the real particle dynamics are much more complex and simplifications are often not justified.

EEDFs of Maxwellian type (as used e.g. by Bose *et al.* [67, 68]) and simulated BOLSIG+ distributions in a radio frequency plasma are shown exemplarily in Figure 3.1. The Maxwellian curves represent the case that inelastic collisions are negligible compared to elastic collisions. The Maxwellian and non-Maxwellian EEDFs approach each other at large mean electron ener-

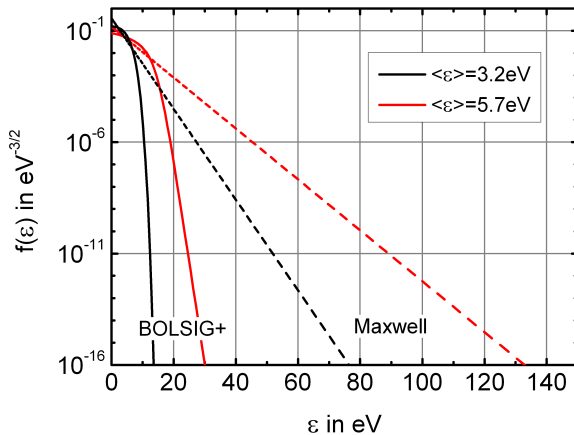


Figure 3.1: Simulated EEDFs including electron-molecule and electron-electron collisions at 13.56 MHz excitation (solid line), compared to Maxwellian distributions (dashed lines) with same mean electron energy $\langle \epsilon \rangle$. Cross section data from Kushner and Zhang [66].

gies $\langle \epsilon \rangle$. However, for common low pressure plasmas with $\langle \epsilon \rangle$ in the range of some eV, the population of electrons may differ by more than ten orders of magnitude above the threshold energy of inelastic collision processes (typically >10 eV). Such, by assuming a Maxwellian distribution, the rates of these processes are overestimated by several orders of magnitude. Consequently, a numerical simulation of the electron-molecule interactions with respect to dissociation processes must be carried out.

Several numerical approaches were published for the determination of the electron-energy distribution function in presence of electron-neutral collisions, and the most common ones are discussed in [69]. The software used in the present work, BOLSIG+ [70], is a time-dependent two-term Boltzmann equation (BE) solver. This approach is based on the assumption that the ions and electrons in the plasma can be described by a fluid model. The first moments of the Boltzmann equation (1.12) for transport are taken into account, which are the continuity equation, the momentum equation, and the energy equation. Here, a two-term approximation of the velocity-space spherical-harmonics expansion is applied to simplify the solution process. The approximation includes an isotropic part f_0 and an anisotropic part,

f_1 , as well as a dependence on the direction of the electric field direction. Furthermore, the electric field as well as collisions probabilities are assumed to be uniform in space. This way, the EEDF f is symmetric in velocity space with respect to the electric field direction. f can only vary along \vec{E} in the position space. Such, it is

$$f(\nu, \cos \theta, z, t) = f_0(\nu, z, t) + f_1(\nu, z, t) \cos \theta. \quad (3.1)$$

θ is the angle of the \vec{v} with respect to \vec{E} , z is the position along the field direction. It is known that static two-term Boltzmann approaches can cause wrong results [71, 72]: This occurs in case of total inelastic cross sections becoming as important as elastic ones, namely at large electron energies. This is partially overcome by using the time-dependent two-term approach by expansion of the anisotropic part f_1 such that

$$f(\nu, \cos \theta, z, t) = f_0(\nu, z, t) + f_1(\nu, z, t) \cos \theta \exp(i\omega t). \quad (3.2)$$

Compared to other higher order multi-term-approximations, two-term approximations yield results of similar quality: Hagelaar and Pitchford [7] stated that in the case that the two-term-approximation fails, other intrinsic approximations of fluid models also fail, making fluid models in general inapplicable under such conditions. Alternative methods like MC¹ and PIC² simulations can be also applied to the modeling of electron-molecule interactions, but in the case that fluid models are applicable, they do not significantly enhance the precision of the simulations.

The algorithm of BOLSIG+ is based on a finite-elements solver working with B-splines and described in more details in the literature [7]. For modeling, electron-collision cross sections of all participating atoms/molecules are required. In addition, estimated or measured electron densities and degrees of ionization are needed. Several different conditions can be considered, e.g. static as well as time-dependent models, oscillating fields, and electron-electron collisions.

¹Monte-Carlo simulation

²particle-in-a-cell simulation

3.1.1 Influence of cross sections on the electron-molecule interactions

For CHF_3 , the electron-collision cross sections $\sigma(\epsilon)$ for dissociation and ionization are controversially discussed and the absolute values published differ by about half an order of magnitude in some cases [66, 73–80]. The influence of this uncertainty on the plasma chemistry was examined by Bose *et al.* [67].

The cross section data set for CHF_3 , published by Kushner and Zhang [66], as well as data from Morgan *et al.* [77] and Voloshin *et al.* [80] are compared in the following. The elastic momentum transfer and inelastic collision cross sections are shown in Figure 3.2. The first cross section data set is based on data fitting by scaling the cross sections of Goto *et al.* [73]. Kushner and Zhang added two inelastic dissociative features around 11 eV, which were both not confirmed by the other authors. One of this features was interpreted as a low-lying neutral dissociation into $\text{CF}_3 + \text{H}$, the second add-on as an attachment process resulting in the formation of both one negative and one positive ion ($\text{F}^- + \text{CHF}_2^+$). According to Morgan *et al.* [77] (Figure 3.2, middle), the momentum transfer cross section shows a resonance structure around 10 eV. This finding was based on quantum-theoretical calculations. The cross sections were validated by swarm analysis of experimental data; attachment was ignored in this work. Based on Morgan’s work, Voloshin *et al.* carried out a quantum-vibrational analysis according to which the experimental findings being under discussion were partially identified as several vibrational transitions. In addition, the progressions of cross sections for higher electron energies were corrected. Contrary to Kushner and Zhang, no dissociation processes in the low-energy range were found. The resonance structure in the momentum transfer cross section of Morgan *et al.* was also not confirmed.

For argon, data from Yanguas-Gil *et al.* [81] were used as input for the solver. In total, it includes one elastic and 38 excitation and ionization channels. The summed cross sections are shown in Figure 3.3. This compilation, which is based on several previous publications as cited therein, is in good agreement with a recent review by Gargioni and Grosswendt [82].

Standard simulation parameters, based on electron density measurements in this work, are given in Table 3.1.

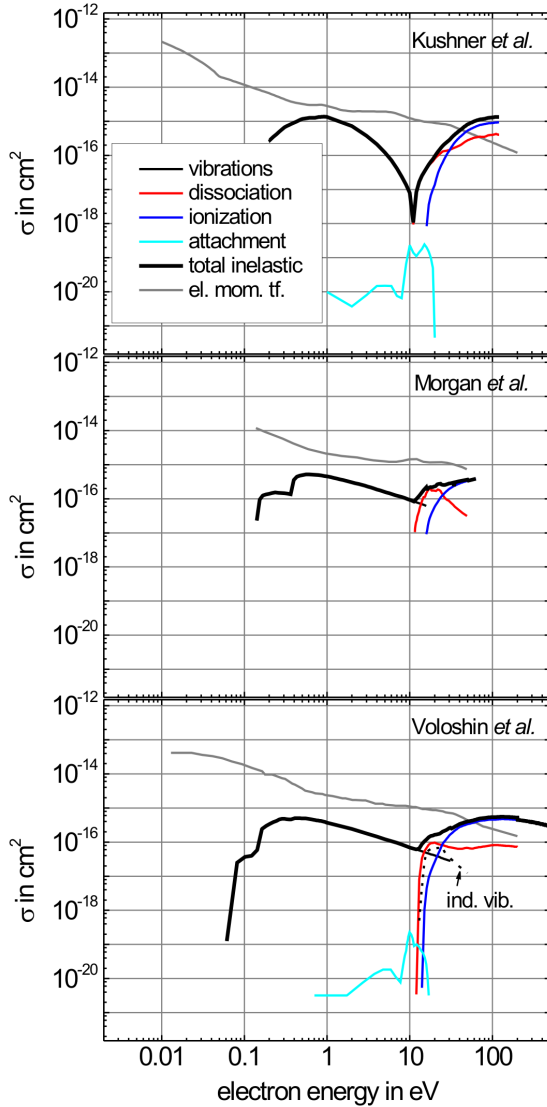


Figure 3.2: Total cross sections based on Kushner and Zhang (top), Morgan *et al.* (middle) and Voloshin *et al.* (bottom). Large differences can be observed in the range around 10 eV due to different data interpretation, see text.

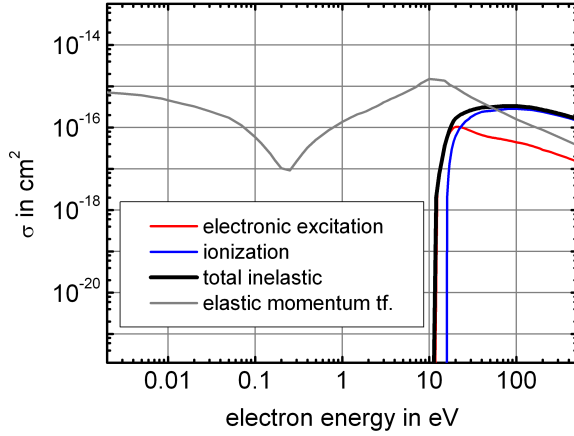


Figure 3.3: Electron collision cross sections of argon from Yanguas-Gil *et al.* [81].

Table 3.1: EEDF standard simulation parameters

parameter	value
Ar content	86%
CHF ₃ content	14%
angular excitation frequency (s ⁻¹)	8.5×10^7
neutral gas density @ 80 Pa (cm ⁻³)	1.98×10^{16}
electron density (cm ⁻³)	5×10^8
net ionization degree	$\approx 2.53 \times 10^{-8}$
reduced electric field in Td	1-1000

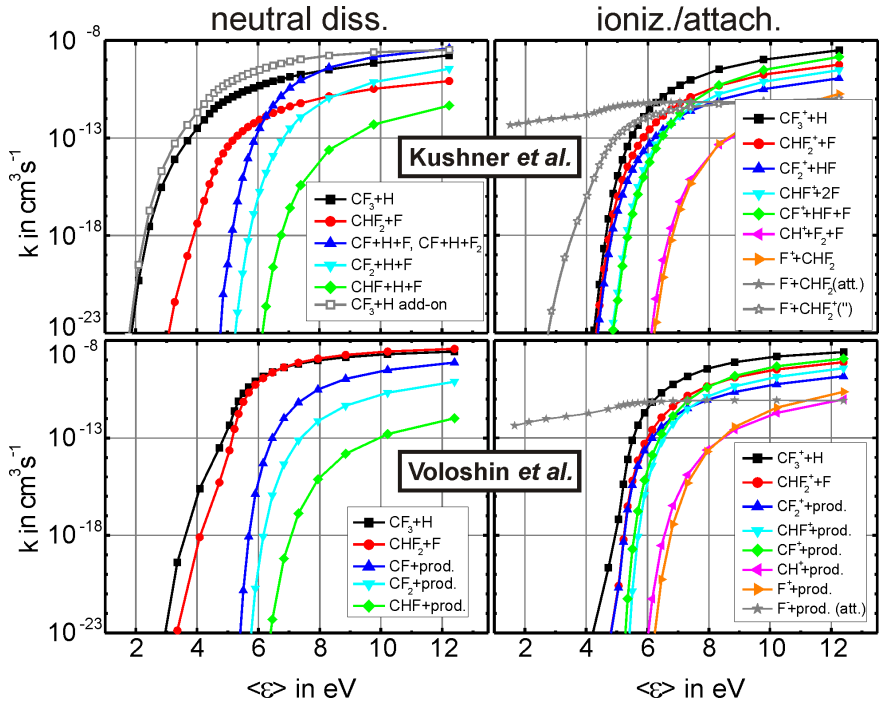


Figure 3.4: Rate coefficients for oscillating field conditions in dependence on the mean electron energy. Cross sections from Kushner and Zhang ([66], top) and Voloshin *et al.* ([80], bottom). Left: neutral dissociation, right: ionization and attachment coefficients.

3.1.1.1 Dependence of EEDF and rates on the cross sections

The results of the calculations based on the cross section data sets (Kushner and Zhang [66], Voloshin *et al.* [80], see Figure 3.2) are shown comparatively in Figure 3.4 in dependence on the mean electron energy.

- Qualitatively, a similar dependence of the rate coefficients on the mean electron energy is observed. CF_3 is throughout the major product from neutral feed gas dissociation (top line in both graphs), followed by CHF_2 and CF . CF_2 is also produced, but the rate constant is at least some orders of magnitude lower than the one of CF . Further fragmentation is obtained from ionization dissociation and electron-attachment dissociation (bottom line in both figures).
- Quantitatively, differences between the two data sets are observed due to the different interpretations of low-lying cross section features. The neutral dissociation data show bad agreement even after the removal of the 11 eV dissociation add-on. In case the additional attachment process around 11.5 eV in Kushner's data (hollow squares in the figure) is discarded, the calculated rate coefficients for the formation of ions show good agreement.

The electronic system is affected by the differences in the cross sections as well. Figure 3.5 shows the mean electron energies and electron mobilities vs. reduced electric field. However, the effect is less than 10% and turned out to be negligible. Such, the overall agreement between the two different cross section sets is fairly good when the ionization rates, the dependence of mean energy on E/N , and the mobility are considered. Contrary, the neutral dissociation rates show much larger deviations. As the quantum-mechanical calculations give a better theoretical background to the data published by Voloshin *et al.*, these cross sections were adopted to the present work.

3.1.2 Influence of additional parameters on the electron-molecule interactions

In addition to the cross sections, the ion and electron densities, the composition of the process gas, and the absolute pressure affect the particle dynamics of electrons in the discharge. To study the influence of these variables on the EEDF, these parameters were varied in additional runs of BOLSIG+.

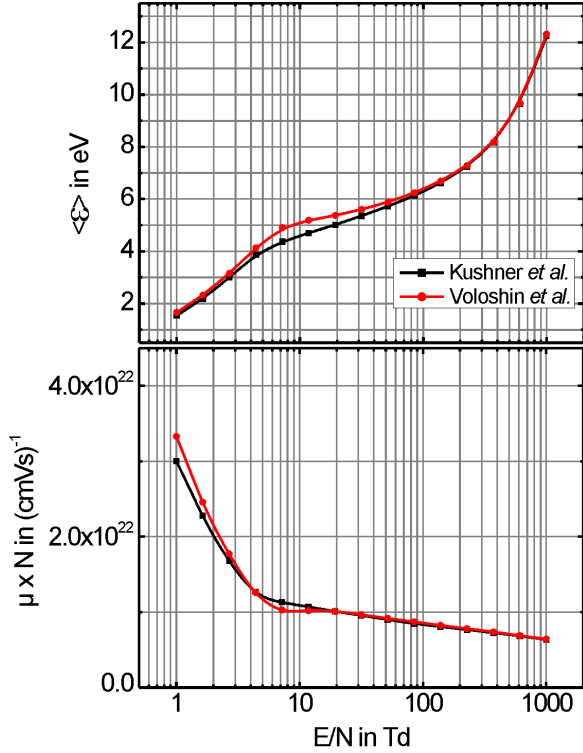


Figure 3.5: Top: Simulated mean energy $\langle \epsilon \rangle$ versus the reduced electric field, E/N , for conditions as noted in Table 3.1, based on different cross section data sets (Kushner and Zhang [66] / Voloshin *et al.* [80]). Bottom: Simulated electron mobility $\mu \times N$ versus the reduced electric field versus the reduced electric field, E/N .

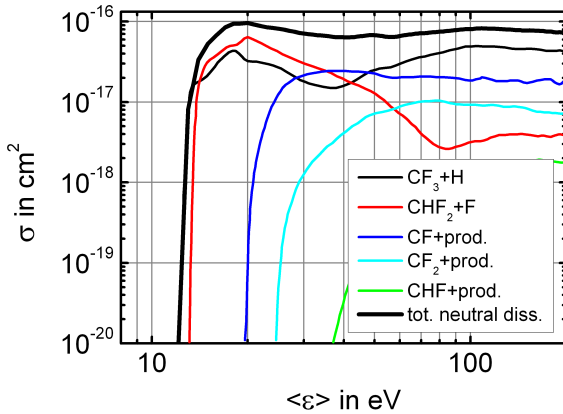


Figure 3.6: Neutral dissociation cross sections of Voloshin *et al.* [80]).

For this study, the cross section data published in [80] were adopted. The neutral dissociation cross sections are shown in detail in Figure 3.6.

3.1.2.1 Influence of plasma parameters

So far, only positive ions have been regarded. But it is known that the density of negative ions in pure rf discharges of CHF_3 can exceed the electron density by about one order of magnitude [83], and therefore, the degree of ionization can be about one order of magnitude larger than expected from electron density measurements. In BOLSIG+, this can be accounted for by setting the degree of ionization separately from the electron density. Upon the variation of the plasma density ($n_{\text{plasma}} = n_e + n_+ + n_-$) as shown in Figure 3.7, an increase in weight in the beginning as well as in the tail of the EEDF is observed in case that the plasma density is increased. The enhancement of the ion density, resulting from an increase in the degree of ionization, α , at unchanged electron density, causes the same increase. Such, the ion density is the major reason for this change in the EEDF compared to standard conditions. This result is comparable to simulations in argon in [7]. Contrary, the separate increment of the electron density n_e only by one order of magnitude does not show any difference compared to the standard conditions. The explanation for such behavior is an increase of the electron-electron collisions upon an increasing degree of ionization, repopulating the high-energy tail of the EEDF like observed in fluid-model

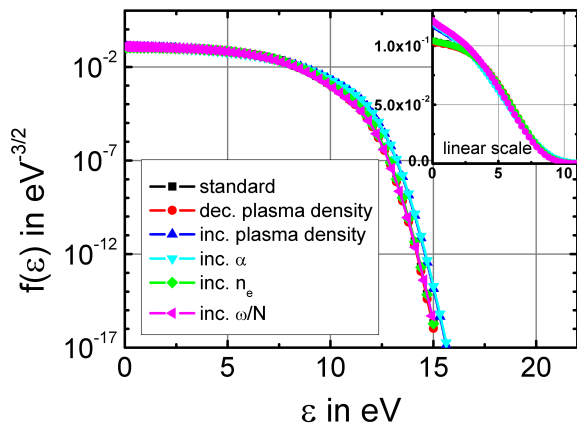


Figure 3.7: Electron energy distribution function $f(\epsilon)$ for several different conditions for $E/N= 4.28$ Td. Variation parameters: plasma density, degree of ionization, electron density, reduced excitation frequency. Standard stands for standard parameters as listed in Table 3.1, inc. and dec. stand for increase and decrease of the variable by an order of magnitude, respectively.

simulations of argon discharges [7]. Finally, the reduced frequency ω/n affects the EEDF as well, again in agreement with the literature for simulations of argon discharges [7]. In this case, only the low-energy part of the EEDF is enhanced: it is known that the EEDF shifts towards a Maxwellian for very high frequencies [5].

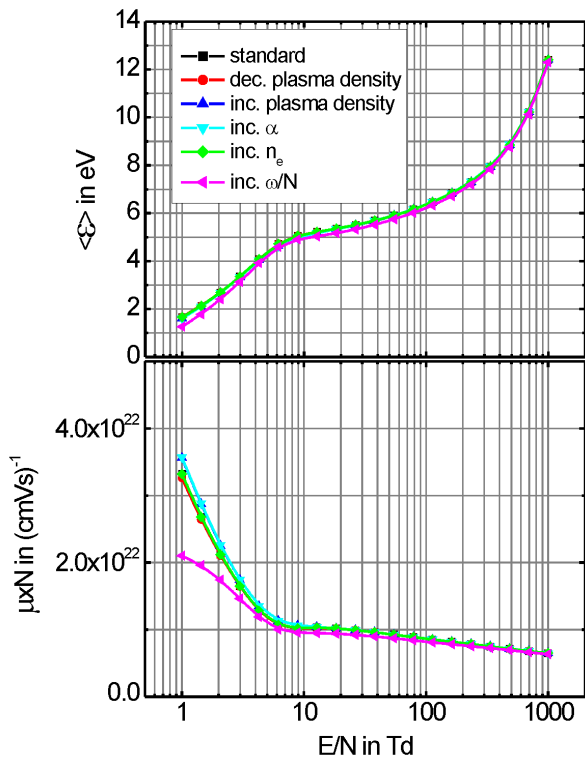


Figure 3.8: $\langle \epsilon \rangle$ and $\mu \times N$ versus the reduced electric field, E/N . Variation of plasma density, degree of ionization, electron density, reduced angular frequency.

As an input for further discharge simulations, the electron mobilities are of importance as well. With the same parameter set of Table 3.1 as a basis and the previous parameter variations, the mean electron energies $\langle \epsilon \rangle$ and electron mobilities μ_e were calculated in dependence of the reduced electric field, E/N and are plotted in Figure 3.8. The variation of the plasma param-

eters has hardly any effect on the dependence of $\langle \epsilon \rangle$ on the E/N as shown in the top graph. This can be attributed to the comparably low charge carrier density. Hardly any change in μ_e can be seen in the lower graph when n_e and the α are varied, except again in the low Townsend regime, where differences of about $\pm 30\%$ are observed when ω/N is increased by one order of magnitude. This may be related to the shifting of the EEDF towards an Maxwellian distribution when the frequency is increased.

3.1.2.2 Influence of gas composition

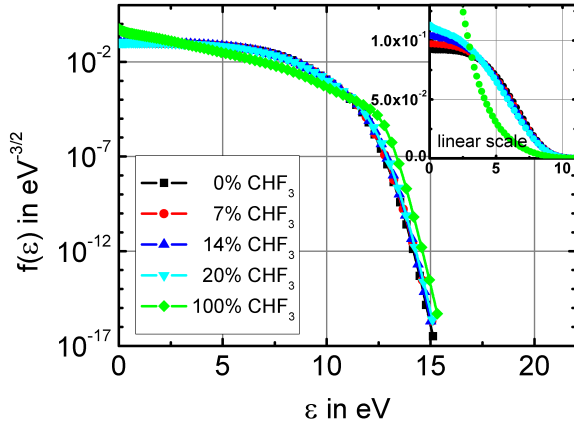


Figure 3.9: Electron energy distribution function $f(\epsilon)$ for several different conditions for $E/N = 4.28$ Td in a CHF_3/Ar gas mixture. Variation parameter: percentage of trifluoromethane.

As can be seen in Figure 3.9, the gas composition also has an influence on the EEDF, which is exemplary shown for $E/N = 4.28$ Td: In the series from pure argon to pure CHF_3 , $f(\epsilon)$ is enhanced for $\epsilon < 3$ eV as well as for $\epsilon > 11.2$ eV, while the intermediate population decreases. The change must be attributed to the different cross sections of argon, where there total inelastic cross section is zero below 11.55 eV, and trifluoromethane, which exhibits low energy vibrations and attachment processes.

The dependence of $\langle \epsilon \rangle$ on the reduced electric field, as shown in Figure 3.10, top, shows a decrease if the partial pressure of CHF_3 is increased. This is due to the overall higher energy consumption by fragmentation.

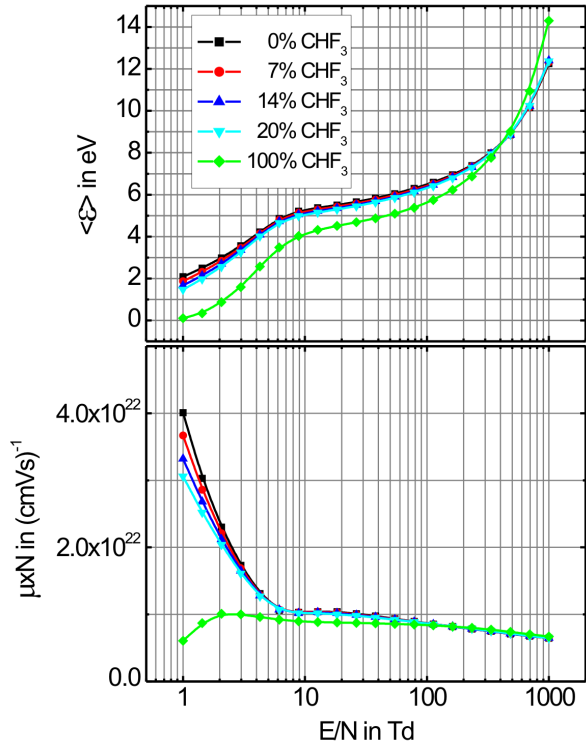


Figure 3.10: $\langle \epsilon \rangle$ and $\mu \times N$ in dependence of E/N (oscillating field) for various gas compositions.

The gas composition also has a slight influence on the mobility in the range of about 15% for concentrations between 0-20%, especially in the low field region, as shown in Figure 3.10, bottom. It becomes flat upon increasing the concentration of CHF₃. This is related to the inelastic cross sections of both molecules.

3.1.3 Parameter dependence of rate coefficients for electron-molecule interactions

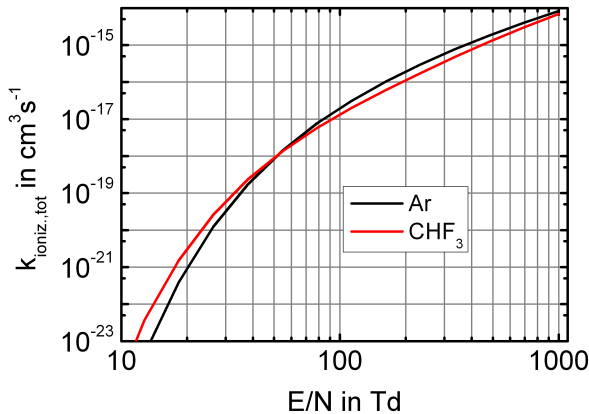


Figure 3.11: Total ionization rate coefficients of Ar and CHF₃ in dependence of E/N.

The dependence of the ionization rate coefficients of argon and CHF₃ on the E/N are plotted in Figure 3.11 for the parameters listed in Table 3.1. Differences between the rate coefficients of both species by maximum one order of magnitude are seen.

3.1.3.1 Effects of plasma parameters and partial pressure

The dissociation and ionization rates are only slightly affected by changes of the variation of gas composition, pressure, etc.. This is in agreement with the literature for such low degrees of ionization [7]. The results of the parameter variations in BOLSIG+ are not plotted here.

3.1.3.2 Effects by superelastic scattering

A point which was not yet accounted for is the presence of superelastic scattering. This is the collision of electrons with excited neutrals, especially metastables, resulting in relaxation of the neutrals and energy transfer to the electrons. Such way, superelastic scattering results in an enhancement of the high-energy tail of the EEDF. In argon, the concentration of metastables is known to be large [84–89]. In particular the $1s_5$ -state (Paschen notation) of the electronic $3s^23p^54s$ configuration is known to be highly populated, followed by the $1s_2$ -, $1s_3$ -, and $1s_4$ -states (4-10 times lower concentrations). Although metastables can be probed by LIF, the concentration could not be measured with the setup used in this work, as the laser system does not emit wavelengths between 355–410 nm. Several values are given in literature for the concentration of the $1s_5$ -state, ranging between $4.5 \times 10^{-9} - 3 \times 10^{-7}$ [88] in a microwave plasma up to $2.8 - 5.7 \times 10^{-6}$ [90] and 1.3×10^{-4} [91] in GEC reference cells at radio-frequency excitation.

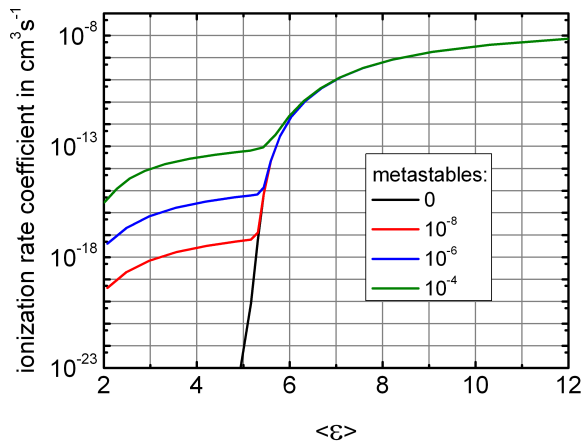


Figure 3.12: Simulation of the ground state ionization rate under variation of the metastable concentrations. Oscillating conditions. Cross section data as included in BOLSIG+.

To illustrate the consequences of metastables in a plasma, an additional simulation in BOLSIG+ was carried out. Therefore, cross section data supplied with the package was used. As an example, the ionization rate

from ground state argon is plotted in Figure 3.12. As can be seen, increased rates appear at low mean energies (<5.5 eV) due to the enhanced EEDF tail. For the present problem, this effect may be of less importance as the mean electron energy was around 5-6 eV, powers were low, and most discharges were pulsed.

3.2 Modeling of plasma particle dynamics in SIGLO-RF

For the modeling of the discharge, SIGLO-RF [92], a one-dimensional plasma simulation program, was used. The plasma is therefore considered to be a fluid system of ions and electrons. The ions can be separated into positive and negative ions if requested. The geometry of the discharge is limited to a cylindrical setup with two opposed equal-sized parallel electrodes. The discharge conditions correspond to those of a capacitively-coupled plasma (ccp, [6]). For the calculation, ion transport is described by a continuity equation and a drift-diffusion momentum transport. For the electron transport, a description by the first three moments of the Boltzmann equation is used. Such, the continuity, momentum transport and energy transport equations are solved. Here, again, a drift-diffusion approach is used for the momentum transport, and the diffusion coefficient D_e is determined from the Einstein relation³, Equation (1.17).

From the numerical calculation in SIGLO-RF, the positive and negative ion densities, the electron densities, and the mean electron energy are obtained with spatial and phase resolution. In addition, plasma and electrode currents as well as power consumption are calculated. More details on the capabilities of SIGLO-RF can be found in the literature [93, 94]. The program requires an input parameter file, which is subject of Section 3.2.1. The parameters are in general handed over in dependence on the reduced electric field, in this case as E/p .

Compared to other approaches based on Monte-Carlo (MC) and Particle-in-a-Cell (PIC) simulations, the program code yields results of same quality under most conditions. A limitation is that at low pressures, plasmas deviate from fluid behavior, and MC/PIC/hybrid simulations yield better results [94]. Nevertheless, this restriction is not relevant in the pressure range which was used here.

³The Einstein relation is valid for Maxwellian EEDFs, but also an acceptable approximation in many real discharge situations [7].

3.2.1 Input parameter file of SIGLO-RF

SIGLO-RF originally only allows to include data of one gas in the simulation. In addition, the program does not consider electron-electron collisions. However, these limitations can be overcome by adaptation of the input parameter file. As input data, the program requires the mean electron energy, electron and ion mobilities, and ionization and attachment rates, each of them in dependence of E/p . The energy loss rate in the discharge is calculated within the program [94]. Similar to E_c in Equation (1.26), this term is necessary to calculate the power dissipation in the plasma by inelastic collisions. In addition, recombination rates have to be included in case of electronegative gases.

3.2.1.1 Charge carrier mobilities

The electron mobilities were calculated with BOLSIG+ in Section 3.1. Such way, also electron-electron collisions are included in SIGLO-RF. The ion mobilities, however, can not be calculated by BOLSIG+. In general, the mobility of an ion in a neutral gas matrix depends on the ion energy, the neutral polarizability, the masses of both ion and neutral, and the gas pressure. In a zero-field approximation, i.e. for ion energies ≈ 0 eV, the ion mobility can be expressed by the Langevin equation [95]:

$$\mu_0 = \frac{13.56}{\alpha_d \mu_r}, \quad (3.3)$$

where α_d is the dipole polarizability of the neutral (here in \AA^3) and μ_r is the reduced mass. μ_0 is the zero-field mobility (in $\text{cm}^2(\text{Vs})^{-1}$) and referred to normal pressure. The Langevin equation was originally introduced for monoatomic systems at low temperatures ($T=0$ K). Despite of this theoretical limitation, a good agreement between calculated and experimental ion mobilities can be even obtained with molecular species at ambient temperature [95].

The validity of the zero-field approximation for the ion mobility in plasma discharges depends on the ion energy. In discharges like those studied here, ions in the plasma bulk are at room temperature (300 K, 25 meV). The energies of ions impinging at the electrodes are below 50 eV (Ar^+) and 100 eV (CF_3^+) [100]. In this energy range, ion-neutral collision cross sections are nearly constant, and the zero-field approximation can be applied. The mobilities were calculated accordingly for several ions and are listed

Table 3.2: Zero-field reduced ion mobilities in $\text{cm}^2(\text{Vs})^{-1}$

ion	m_{ion}	neutral	m_{neu}	α_d	μ_0^*	experimental
CF_3^+	69	CF_4	88	3.838	1.11	0.96 ± 0.04 [95]
F^-	19	CF_4	88	3.838	1.75	1.50 [96]
Ar^+	40	CHF_3	70	3.52	1.43	–
CF_3^+	69	CHF_3	70	3.52	1.23	–
CHF_2^+	51	CHF_3	70	3.52	1.33	0.53 ± 0.01 [95]**
CF_2^+	40	CHF_3	70	3.52	1.43	–
CF^+	31	CHF_3	70	3.52	1.56	–
C^+	12	CHF_3	70	3.52	2.26	–
F^-	19	CHF_3	70	3.52	1.87	–
Ar^+	40	Ar	40	1.6411	2.37	1.53 [97]
CF_3^+	69	Ar	40	1.6411	2.10	–
CF_3^+	69	Ar	40	1.6411	2.10	–
CHF_2^+	51	Ar	40	1.6411	2.24	–
CF_2^+	40	Ar	40	1.6411	2.37	–
CF^+	31	Ar	40	1.6411	2.53	–
C^+	12	Ar	40	1.6411	3.48	3.40 ± 0.08 [95]
F^-	12	Ar	40	1.6411	2.95	3.33-4.54 [98], [99]

*: calculated according to Equation (3.3)

** : strong discrepancy due to cluster formation suggested

in Table 3.2. It is found that all calculated zero-field mobilities of molecules and atoms are in the same range around $1.1 - 3.5 \text{ cm}^2(\text{Vs})^{-1}$, forming two subgroups. These subgroups depend on the neutral gas matrix (molecular ions in argon: $\mu_0 \approx 2.1 - 2.5 \text{ cm}^2(\text{Vs})^{-1}$, molecular ions in CHF_3 : $\mu_0 \approx 1.2 - 1.6 \text{ cm}^2(\text{Vs})^{-1}$). For monoatomic ions, the mobilities are slightly larger, but differ by less than 60% from those of molecular ions. In addition, the gas matrix composition only has a small influence as well. This is due to the low polarizability of fluorocarbons which is similar to the one of argon: The polarizability of trifluoromethane is only twice as large as the polarizability of argon. For comparison: other organic halides like chloroform, bromoform, and iodoform possess polarizabilities which are about 3-5 times larger than the one of argon [101].

The mobility of one ionic species in a gas mixture (a matrix composed of trifluoromethane and argon) is calculated by the reciprocal of the weighted mobilities in pure trifluoromethane and argon matrices. To obtain the average ion mobility of several ionic species in a gas mixture, as required in the input parameter file of SIGLO-RF, the ion mobilities need to be weighted by the partial pressures of the ions as well. This requires estimations about the ion appearances, which can be assessed from the rate coefficients determined in Section 1.2.4. Fortunately, as shown before, the ion mobilities are all in the same range, and errors can be therefore neglected⁴.

3.2.1.2 Production and loss channels of positive and negative ions

Further data are required for modeling, which are the production and loss rates of ions in the gas mixture. The production channels are ionization and attachment, the loss channels are ion-ion recombination as well as electron detachment.

The total rate coefficients for both ionization and attachment, $k_{tot,i/a}$ for the specific channels in argon and CHF_3 have to be weighted according to the gas composition, $k_{tot} = k_{\text{Ar}}p_{\text{Ar}} + k_{\text{CHF}_3}p_{\text{CHF}_3}$. The ionization and attachment rates are obtained from BOLSIG+ and are given in dependence on E/p .

Dissipation channels of ions are generally depending on the densities of the participating species. Furthermore, they depend on the particle energies.

⁴In SIGLO-RF, some simulations were carried out with the ion mobility as the only variation parameter. The results were invariant and are therefore not shown here.

Table 3.3: Ion dissipation channels

#	process	k in cm^3s^{-1}
1	i-i rec. in C_2F_6	1.5×10^{-7} [102]
2	i-i rec. in CF_4	$5 \pm 2 \times 10^{-7}$, 8.8×10^{-7} [28, 96, 103]
3	i-i rec. in CHF_3	3.9×10^{-6} [102]
4	$\text{Ar}^+ + \text{F}^- \rightarrow \text{Ar} + \text{F}$	10^{-7} [104]
5	$\text{F}^- + \text{CF}_x \xrightarrow{\text{M}} \text{CF}_{x+1} + \text{e}^-$	5×10^{-7} [96]
6	$\text{e}^- + \text{CF}_x^+ \rightarrow \text{CF}_{x-1} + \text{F}$	4×10^{-8} [105]

For purely ionic processes, the dependence on the ion energy can be neglected as the ion energy is low and the cross sections are about constant. The dissipation by ion-ion recombination is generally pressure dependent [27] as expected. In the low-pressure region, data are available for ion-ion recombination rates in several fluorocarbon gases as listed in Table 3.3 (channels 1-4). These values are larger than those obtained from theoretical calculations in [24], but are all in a similar range. In gas mixtures containing Ar, neutralization via $\text{Ar}^+ + \text{F}^-$ has to be considered as well. As input data for SIGLO-RF, the total recombination rate was again obtained by weighting the rates given in [102] and [104]. Associative collisional detachment (channel 5) and electron-ion recombination (channel 6) are also loss mechanisms. For associative collisional detachment, in [96], CF_3 was assumed to be the neutral fluorocarbon reactant. Based on simulation results in Section 4.2.3, the CF_3 density is similar to the one of CF and ranges around 10^{-6} cm^{-3} and yields an first-order rate ("detachment frequency") of about 10/s. The discharge simulation turned out to be highly insensitive against variation of this parameter, even after increasing it by a factor of 10.

In the case of electron-ion recombination processes, an energy dependence can be observed. The rates were estimated in the literature [105]. This process is dissociative and yields smaller molecules: $\text{e}^- + \text{CF}_x^+ \rightarrow \text{CF}_{x-1} + \text{F}$. Due to the large mobility of electrons, they are mostly lost by electron currents at the electrodes. This process is accordingly of minor importance, supported by simulation results upon variation of this rate (not shown), in agreement with the literature for $n_e < 10^{13} \text{ cm}^{-3}$ and $T_e > 1 \text{ eV}$ [5].

After determination of the input parameters, the input parameter file was written accordingly for each gas mixture. For the simulation, the elec-

trode spacing was fixed to 45 mm which is equal to the one of the experimental setup used. The frequency was set to 13.56 MHz, the pressure was set according to the ones used in the experiments. For performing a power series simulation, the voltage was set to values commonly between 60-150 V. In the experiments, pure argon and trifluoromethane plasmas were examined in the power range of 5-50 W. The pressures were chosen such that they could be compared to (experimentally) stable discharges at elevated pressures. For both argon and CHF₃, these were 30 and 60 Pa. The examined parameters for gas-mixtures of argon and trifluoromethane were in the range of:

- total pressure: 60-80 Pa
- partial pressure of CHF₃: 7-20 % of the total pressure
- power: between 5-50 W

3.2.2 Modeling results

An important detail for subsequent models results from the simulation in SIGLO-RF. The dependence of $\langle \epsilon \rangle$ on the plasma power, which is plotted for several pressures and gas flows in Figure 3.13, shows a slight decrease upon increasing the power. It is also seen that $\langle \epsilon \rangle$ is mostly lower with $F_{CHF_3}=15$ sccm than with 5 and 10 sccm. It is further seen that the pressure has hardly any effect. The differences resulting from gas flows and pressures may be attributed to the different charge carrier mobilities in the gas mixtures and the different neutral density, respectively. The dependence on the plasma power has important effects on the chemical reaction rates, which is discussed below. A general explanation for the dependence of $\langle \epsilon \rangle$ on the plasma power can not be given. Especially here, a plasma in an electronegative gas is present. Such way, the particle dynamics are highly sophisticated and numerical models are the only way to gain insight (see Section 1.2.2).

As a consequence, lower electron energies result in

- a decrease of the rate coefficients $k_{ioniz.,att.}$ for attachment and ionization (compare Figure 3.4),
- an increase of attachment versus ionization rates.

As a further consequence, the fast linear increase in ion density, which is observed in the low power/low voltage regime in Figure 3.14, changes its

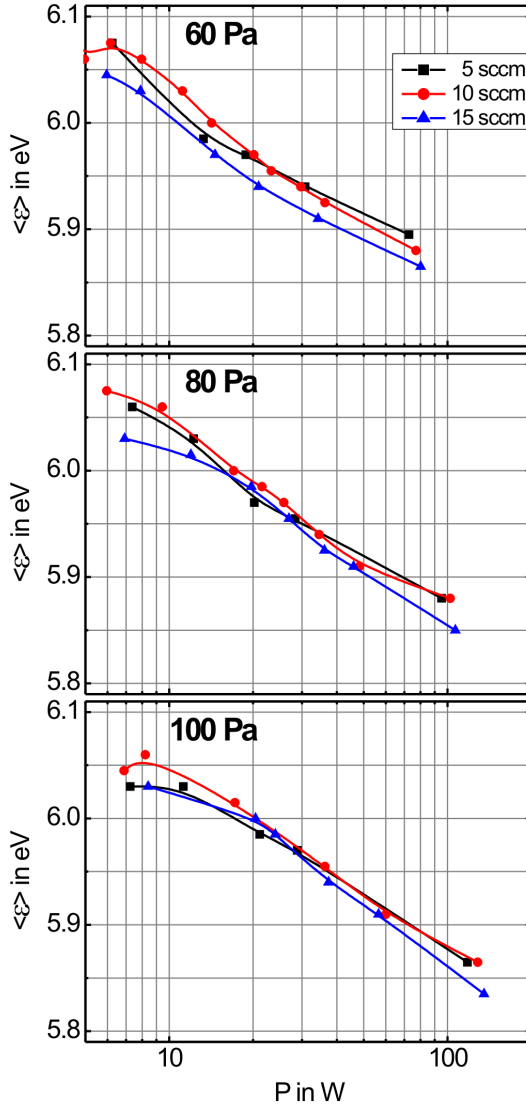


Figure 3.13: Plot exemplary showing the dependence of the mean electron energy $\langle \epsilon \rangle$ on plasma power.

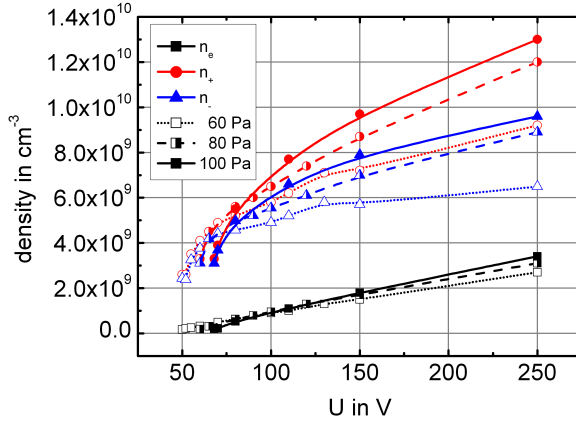


Figure 3.14: Charge carrier densities vs. discharge voltage for 60 (hollow), 80 (half filled), 100 Pa (full symbols). Notice the change in slope of the ion densities.

slope. A change in the slope of ion densities similar to here was published in [102]. Contrary to the decrease in $\langle \epsilon \rangle$, n_e increases about linearly with increasing discharge power. Such, the ratio n_-/n_e of negative ions to electrons increases and almost saturates at 60 – 75 V. The electron and ion densities increase when the pressure is increased. At higher pressures, the power consumption is higher which supports this result.

The resulting dependence of the plasma power on the discharge voltage is depicted in Figure 3.15 and shows an almost linear dependence for the three pressures.

In Figure 3.16, the current-voltage characteristics are shown. For all pressures, a strong increase in the low-voltage regime is observed, followed by a moderate linear increase at higher voltages. The overall increase in ions compared to electrons has an effect on the electron mobility as seen in Figure 3.14. Such, the current-voltage characteristics show changes in the slope in the same region of 60-75 V. But still, the characteristics are typical for an α -mode discharge [6].

For the proceeding of this work, the simulation results were adopted to chemical modeling.

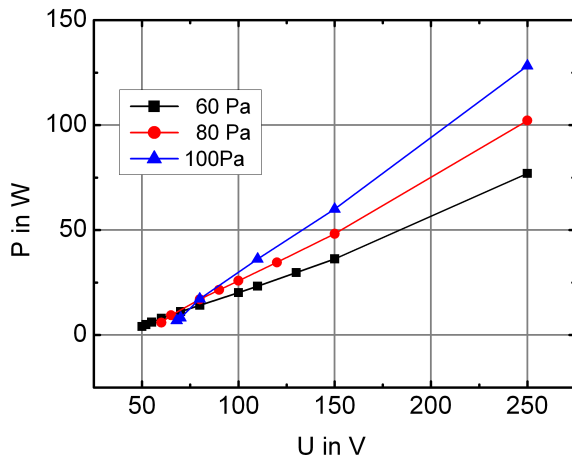


Figure 3.15: The power-voltage characteristics according to modeling.

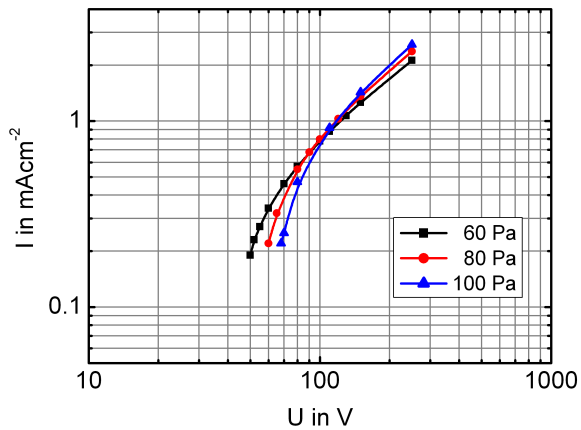


Figure 3.16: The current-voltage characteristics according to modeling. The dependence of the currents are typical for the ignition regime of an α discharge.

3.2.3 Dissociation rate coefficients under the experimental conditions

Making use of the SIGLO-RF model, the dissociation rates in CHF_3 plasmas were calculated. According to Section 1.2.4, the rate coefficients depend on the mean electron energy $\langle \epsilon \rangle$. $\langle \epsilon \rangle$ depends on the gas composition, but turned out to hardly depend on the degree of ionization and the electron density (Section 3.1). This was accounted for by using the different rate coefficients $k(\langle \epsilon \rangle)$ for each combination of partial pressures of CHF_3 and argon.

The electron density depends on the applied power, the gas composition as well as on the pressure. These results from BOLSIG+ and SIGLO-RF were used to determine the first-order rate

$$k_1 = k(\langle \epsilon \rangle) n_e(P, p_{\text{CHF}_3}, p_{\text{tot}}), \quad (3.4)$$

which is plotted for different pressures and gas flows in Figure 3.17. Therefore, the second-order rate coefficient, $k(\langle \epsilon \rangle)$, was obtained from fitting the results of BOLSIG+ from Section 3.1 and evaluation of the fitting function for $\langle \epsilon(P) \rangle$. $\langle \epsilon(P) \rangle$ was obtained from the results of SIGLO-RF (see Figure 3.13). The first-order rate k_1 was then finally calculated by multiplication with $n_e(P)$, a further result of SIGLO-RF (depicted in Figure 3.14).

The major trends are the same for all gas compositions and show a rate increase upon increasing plasma power. Slight differences are observed when either the absolute or the partial pressure are varied. However, for chemical reactions the gas phase, small differences in the rates of processes yielding hydrogen or fluorine can have significant effects. Such, additional information about the influence of power is obtained by plotting the decomposition ratio $r_{\text{CF}_3, \text{CHF}_2}$ of $\text{CF}_3 + \text{H}$ and $\text{CHF}_2 + \text{F}$ formation, see Figure 3.18. In general, it is found that the higher the power, the higher $r_{\text{CF}_3, \text{CHF}_2}$ which means that the formation of $\text{CF}_3 + \text{H}$ is more and more preferred upon increasing the power. This is based on the lower electron energies required for this dissociation channel, and the fact that the mean electron energy slightly decreases when the power is increased according to Figure 3.13. Furthermore, when the partial pressure of CHF_3 is increased, $r_{\text{CF}_3, \text{CHF}_2}$ decreases. This is due to lowering of $\langle \epsilon \rangle$ upon increasing F_{CHF_3} (Figure 3.13).

The dissociative ionization and attachment rates are plotted in Figure 3.19 versus P . They show a flow- and pressure dependence as well. It is worth mentioning that these rates are at least one order of magnitude lower

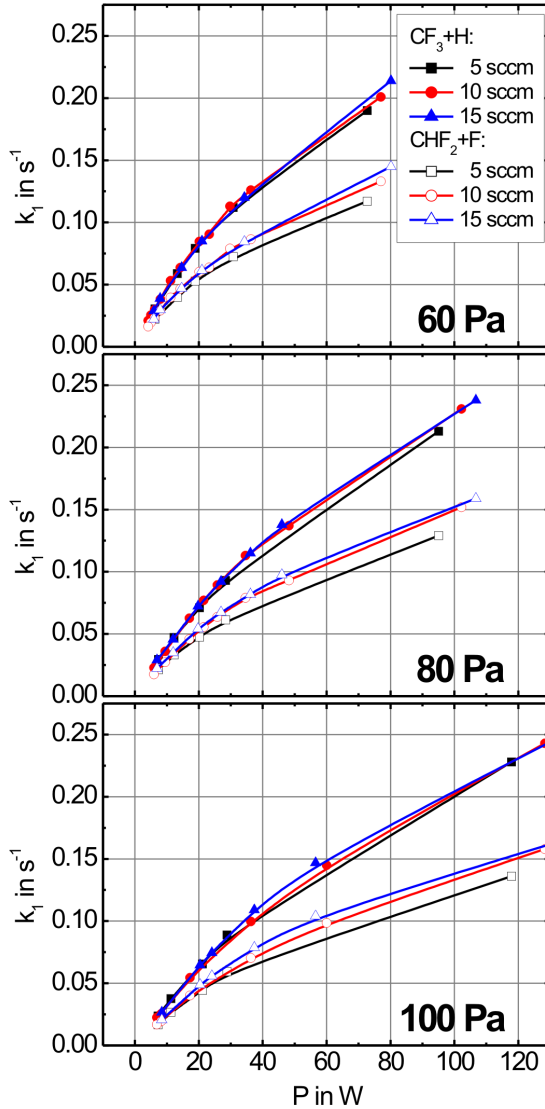


Figure 3.17: The major neutral dissociation channels of CHF_3 yield $\text{CF}_3 + \text{H}$ (full symbols) and $\text{CHF}_2 + \text{F}$ (hollow symbols). The rate k_1 increases when the plasma power is increased. Differences can be observed when the gas pressure is varied or the gas composition is changed. The flow of argon is constant in all cases.

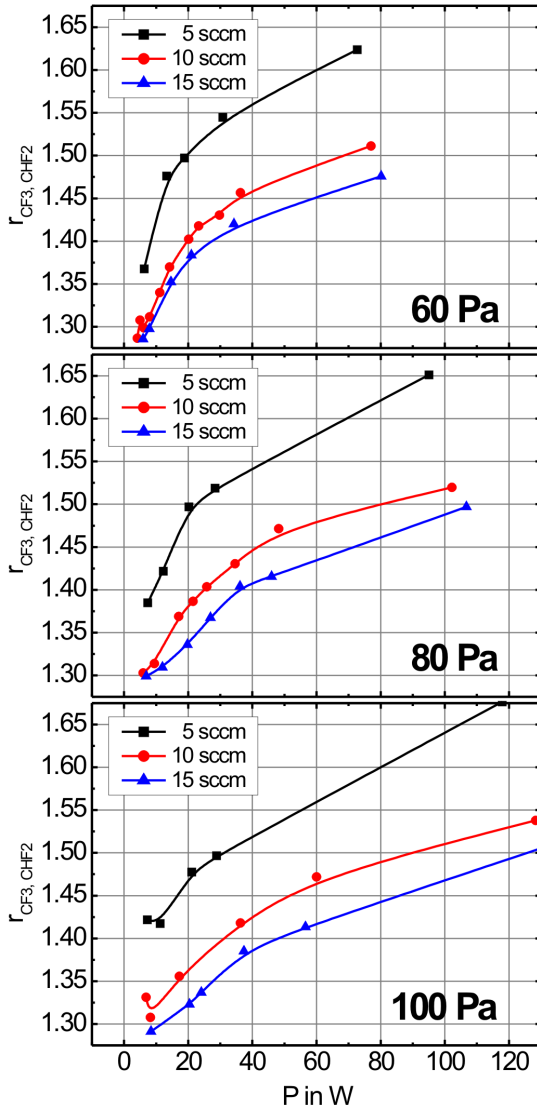


Figure 3.18: The ratio r of the major neutral dissociation channels shows a dependence on power as well as on the gas composition. The flow of argon is constant in all cases.

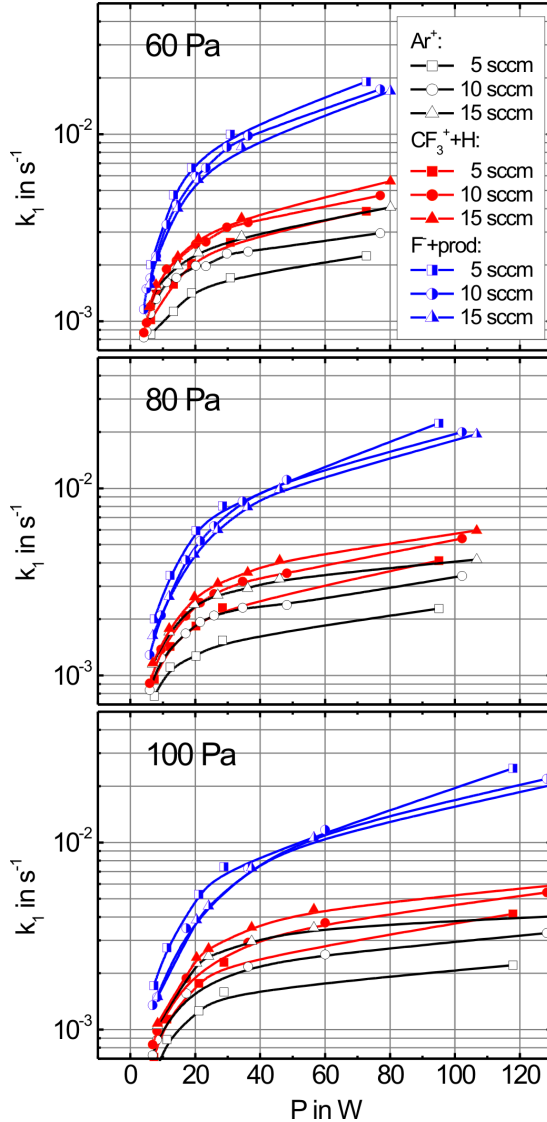


Figure 3.19: The major ionization channels of CHF_3 yields $\text{CF}_3^+ + \text{H}$ (full symbols, red). Electron attachment results in formation of $\text{F}^- + \text{prod}$. (half-filled symbols, blue). The flow of argon is constant in all cases; for completeness, the argon ionization rate is shown as well (hollow symbols, black). Rates lower than 10^{-4} s^{-1} are not shown.

than the neutral dissociation rates. For completeness, the ionization rate of argon is shown as well: although the rate is lower than the ionization rate of CHF_3 , the concentration of Ar^+ is probably larger than the one of CF_3^+ . This is due to the partial pressure of argon in the examined discharges, which is larger than the partial pressure of CHF_3 by a factor of 4-6.

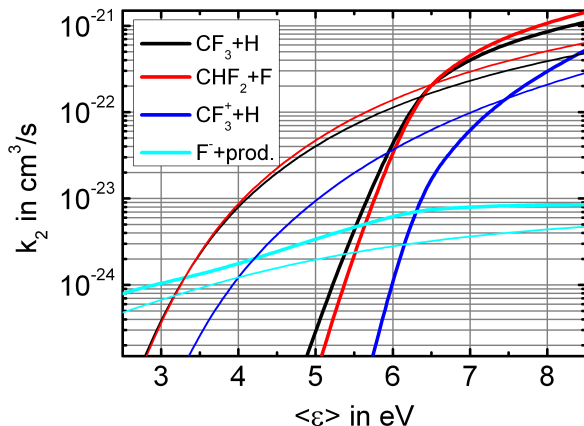


Figure 3.20: Electron-collision induced dissociation rates based on EEDFs modeled with BOLSIG+ (thick lines) and Maxwellian EEDFs (thin lines).

Comparative runs of the simulations with Maxwellian EEDFs were carried out as well. Due to the lack of inelastic processes in the Maxwellian model, the high-energy tail is well pronounced and drastically affects the data. Such, different rate coefficients as shown in Figure 3.20 result: besides different absolute values, also the relative strength of the channels is different. This concerns especially the neutral dissociation processes resulting in the formation of $\text{CF}_3 + \text{H}$ and $\text{CHF}_2 + \text{F}$, which are reversed in their order of appearance in the Maxwellian case. Several authors published modeling with Maxwellian EEDFs. But due to the restrictions of the Maxwellian model for this application, the results of simulations on this basis may include errors of several orders of magnitude.

3.3 Modeling of chemical processes in pulsed and continuous discharges

Chemical modeling of plasma discharges is still a difficult field. Up to now, the major problem is to get knowledge about the exact chemical rate coefficients, which are additionally often pressure dependent. Large sets of partial differential equations (PDEs) have to be solved. Plasmas with macromolecule formation (oligomerization) enhance the complexity additionally.

Some publications on this topic were taken as a stimulus for the chemical reaction modeling performed in this work. In the 1980's, Plumb and Ryan [13] published modeling of a $\text{CF}_4 + \text{O}_2$ discharge. In 2001, Ho *et al.* published modeling on etching discharges in C_2F_6 and CHF_3 [105]. In both publications, only etching species were taken into consideration which were formed by both electron-collision induced dissociation and chemical reactions. Sort of a break-through in macromolecule-forming plasmas was the comprehensive publication of Burgess *et al.* on thermochemical kinetic data of hydrofluorocarbons [9], which found e.g. entry in the works of Schabel *et al.* [15] and Voloshin *et al.* [80]. Schabel, Peterson, and Muscat published their work on macromolecule formation in CF_4 -plasmas with a H_2 admixture. Dimerization of CF_2 was not considered, which may have resulted in significant errors as the dimer C_2F_4 represents a "dead end" for chemical reactions according to current understanding [8]. For $C_{n \geq 3}$ backbones, only pure fluorocarbons were considered. The same accounts for the present work because of the lack of knowledge of rate coefficients for the formation of hydrofluorocarbon oligomers. In 2007, Voloshin *et al.* published chemical simulations on CHF_3 discharges [80]. In their publication, less hydrofluorocarbon reactions were taken in consideration than in Schabel's work.

3.3.1 Dissociation and reaction processes

For the present study, in total 122 reaction channels from the literature were included in a Comsol Multiphysics simulation. Reaction-diffusion processes were include as well. The reaction channels are listed in Tables 3.4 to 3.8. It must be noticed that even though some rates are lower than $k_2 = 10^{-15} \text{ cm}^3\text{s}^{-1}$, the respective channels can play an important role as long as the concentrations of the reacting species are large. Vice versa, large rate coefficients do not necessarily mean that the processes are of relevance to

Table 3.4: Reaction channels considered in chemical modeling: Dissociation and ionic channels

no.	educts	products	k_2
1.	$C_2F_3 + e^-$	$CF + CF_2 + e^-$	2.5×10^{-9} *
2.	$C_2F_4 + e^-$	$CF_2 + CF_2 + e^-$	2.5×10^{-9} [80]
3.	$C_2F_5 + e^-$	$CF_3 + CF_2 + e^-$	4.1×10^{-11} [80]
4.	$C_2F_6 + e^-$	$2CF_3 + e^-$	4.1×10^{-11} [80]
5.	$C_2HF_5 + e^-$	$CF_3 + CHF_2 + e^-$	4.1×10^{-11} *
6.	$C_3F_6 + e^-$	$C_2F_4 + CF_2 + e^-$	4.1×10^{-11} [80]
7.	$CF_2 + e^-$	$CF + F + e^-$	7.5×10^{-11} [15]
8.	$CF_3 + e^-$	$CF_2 + F + e^-$	2.3×10^{-10} [15]
9.	$CHF_2CHF_2 + e^-$	$CHF_2 + CHF_2 + e^-$	4.1×10^{-11} *
10.	$CHF_3 + e^-$	$CHF_2 + F + e^-$	sec. 3.2.3
11.	$CHF_3 + e^-$	$CF_3 + H + e^-$	sec. 3.2.3
12.	$H_2 + e^-$	$H + H + e^-$	5.4×10^{-10} [80]
13.	$HF + e^-$	$H + F + e^-$	4.7×10^{-9} [80]
14.	$C_2F_6 + e^-$	$C_2F_5 + F^-$	2.0×10^{-9} [15]
15.	$C_3F_8 + e^-$	$C_3F_7 + F^-$	1.2×10^{-9} [15]
16.	$C_4F_{10} + e^-$	$C_4F_9 + F^-$	1.3×10^{-9} [15]
17.	$CHF_3 + e^-$	$CHF_2 + F^-$	sec. 3.2.3
18.	$C_2F_6 + e^-$	$CF_3^+ + CF_3 + e^-$	1.5×10^{-9} [15]
19.	$C_2F_6 + e^-$	$CF^+ + CF_3 + 2F + e^-$	6.2×10^{-11} [15]
20.	$C_2F_6 + e^-$	$CF_2^+ + CF_3 + F + e^-$	1.7×10^{-11} [15]
21.	$C_3F_8 + e^-$	$CF_3^+ + C_2F_5 + e^-$	1.2×10^{-10} [15]
22.	$C_3F_8 + e^-$	$CF^+ + C_2F_5 + 2F + e^-$	1.4×10^{-11} [15]
23.	$CF + e^-$	$CF^+ + e^-$	8.3×10^{-8} [15]
24.	$CF_2 + e^-$	$CF_2^+ + e^-$	5.6×10^{-10} [15]
25.	$CF_2 + e^-$	$CF^+ + F + e^-$	4.9×10^{-10} [15]
26.	$CF_3 + e^-$	$CF_3^+ + e^-$	7.8×10^{-10} [15]
27.	$CF_3 + e^-$	$CF_2^+ + F + e^-$	2.8×10^{-10} [15]
28.	$CF_3 + e^-$	$CF^+ + 2F + e^-$	6.8×10^{-11} [15]
29.	$CHF_3 + e^-$	$CHF_2^+ + F + e^-$	sec. 3.2.3
30.	$CHF_3 + e^-$	$CF^+ + HF + F + e^-$	sec. 3.2.3
31.	$CHF_3 + e^-$	$CF_3^+ + H + e^-$	sec. 3.2.3
32.	$Ar^+ + F^-$	$F + Ar$	1.0×10^{-7} [104]
33.	$CF_2^+ + F^-$	$F + CF_2$	9.1×10^{-8} [24]
34.	$CF_3^+ + F^-$	$F + CF_3$	1.0×10^{-7} [104]
35.	$CF^+ + F^-$	$F + CF$	9.8×10^{-8} [24]
36.	$CHF_2^+ + F^-$	$F + CHF_2$	1.0×10^{-7} *

*: see text; k_2 in cm^3s^{-1}

Table 3.5: Reaction channels considered in chemical modeling: neutral reactions

no.	educts	products	k_2
37.	$C_2F_5 + CF$	$\rightarrow C_3F_6$	1.0×10^{-12} [80]
38.	$C_2F_4 + CF_2$	$\rightarrow C_3F_6$	5.8×10^{-20} [15]
39.	$C_2F_5 + CF_2$	$\rightarrow C_3F_7$	2.0×10^{13} [15]
40.	$C_3F_7 + CF_2$	$\rightarrow C_4F_9$	2.0×10^{-13} [15]
41.	$C_4F_9 + CF_2$	$\rightarrow C_5F_{11}$	2.0×10^{-13} [15]
42.	$CF + CF_2$	$\rightarrow C_2F_3$	1.0×10^{-12} [13]
43.	$CF_2 + CF_2$	$\rightarrow C_2F_4$	3.3×10^{-14} [9, 13]
44.	$CF_3 + CF_2$	$\xrightarrow{M} C_2F_5$	8.9×10^{-13} [13]
45.	$CHF + CF_2$	$\rightarrow CHF_2CF_2$	1.7×10^{-11} [9]
46.	$CHF + CF_2$	$\rightarrow C_2F_2 + HF$	1.5×10^{-11} [9]
47.	$CHF + CF_2$	$\rightarrow CF_2CF + H$	1.3×10^{-17} [9]
48.	$CHF_2 + CF_2$	$\rightarrow CHF_2CF_2 + F$	6.6×10^{-12} [9]
49.	$CHF_2 + CF_2$	$\rightarrow C_2F_4 + H$	3.3×10^{-12} [9]
50.	$C_2F_3 + CF_3$	$\rightarrow C_3F_6$	1.3×10^{-11} [80]
51.	$C_2F_4 + CF_3$	$\rightarrow C_3F_7$	5.5×10^{-15} [106]
52.	$C_2F_5 + CF_3$	$\rightarrow C_3F_8$	1.9×10^{-11} [15]
53.	$C_2HF_5 + CF_3$	$\rightarrow C_2F_5 + CHF_3$	1.0×10^{-20} [9]
54.	$C_3F_7 + CF_3$	$\rightarrow C_4F_{10}$	1.9×10^{-11} [15]
55.	$C_4F_9 + CF_3$	$\rightarrow C_5F_{12}$	1.9×10^{-11} [15]
56.	$CF_3 + CF_3$	$\xrightarrow{M} C_2F_6$	2.1×10^{-12} [14]
57.	$CH_2F_2 + CF_3$	$\rightarrow CHF_2 + CHF_3$	8.3×10^{-21} [9]
58.	$CHF_2 + CF_3$	$\rightarrow C_2HF_5$	2.2×10^{-11} [9]
59.	$CHF_2 + CF_3$	$\rightarrow C_2F_4 + HF$	1.0×10^{-13} [9]
60.	$CHF_2CHF_2 + CF_3$	$\rightarrow CHF_2CF_2 + CHF_3$	2.0×10^{-21} [9]
61.	$CF_3 + CHF$	$\rightarrow CHF_2CF_2 + F$	1.0×10^{-11} [9]
62.	$CHF + CHF$	$\rightarrow C_2HF + HF$	2.9×10^{-11} [9]
63.	$CHF + CHF$	$\rightarrow CH_2CF_2$	8.6×10^{-12} [9]
64.	$CHF + CHF$	$\rightarrow CHF_2CF + H$	2.6×10^{-16} [9]
65.	$CHF_2 + CHF$	$\rightarrow CHF_2CHF + F$	6.6×10^{-12} [9]

Table 3.6: Reaction channels considered in chemical modeling: neutral reactions, continued

no.	educts	products	k_2
66.	$\text{CHF}_2 + \text{CHF}$	$\rightarrow \text{CHF}_2\text{CF}_2 + \text{H}$	3.3×10^{-12} [9]
67.	$\text{C}_2\text{HF}_5 + \text{CHF}_2$	$\rightarrow \text{CF}_2\text{CHF} + \text{CH}_2\text{CF}_2$	1.7×10^{-20} [9]
68.	$\text{C}_2\text{HF}_5 + \text{CHF}_2$	$\rightarrow \text{C}_2\text{F}_5 + \text{CH}_2\text{CF}_2$	1.7×10^{-20} [9]
69.	$\text{CF}_3 + \text{CHF}_2$	$\rightarrow \text{CHF}_3 + \text{CF}_2$	1.7×10^{-12} [9]
70.	$\text{CHF}_2 + \text{CHF}_2$	$\rightarrow \text{CHF}_2\text{CHF}_2 +$	2.9×10^{-11} [9]
71.	$\text{CHF}_2 + \text{CHF}_2$	$\rightarrow \text{CH}_2\text{F}_2 + \text{CF}_2$	3.4×10^{-12} [9]
72.	$\text{CHF}_2 + \text{CHF}_2$	$\rightarrow \text{CHF}_2\text{CF}_2 + \text{HF}$	5.6×10^{-13} [9]
73.	$\text{CHF}_2\text{CHF}_2 + \text{CHF}_2$	$\rightarrow \text{CHF}_2\text{CF}_2 + \text{CH}_2\text{CF}_2$	2.6×10^{-20} [9]

k_2 in cm^3s^{-1}

the model. From this point of view, it is difficult to estimate the importance of a channel. As cut-off criterion, a rate $k_2 < 10^{-21} \text{ cm}^3\text{s}^{-1}$ was defined for the data from [9]. The process rate coefficient of channels 5 and 9 were adopted from the process channel 4, assuming similar cross sections for both molecules. The ion-ion recombination rate coefficient of channel 36 was adopted from channel 34.

3.3.2 Additional effects of ions on the plasma chemistry

As can be seen in Figures 3.17 and 3.19 in Section 3.2.3, the first-order dissociative ionization rates are lower compared to those obtained from neutral dissociation. These channels could be, however relevant, so they were tentatively included in the models. The inclusion of ionic channels was carried out by the requirement of quasi-neutrality of the plasma, i.e. $n_+ = n_- + n_e$. Ion-electron neutralization was neglected in the model. Furthermore, detachment processes are of minor importance according to Section 3.2. Such way, the steady ion density in the plasma of about 10^{10} cm^{-3} is reached after a time τ of typically less than some microseconds so that, after the equilibrium is reached, the attachment rate must be neutralized by the recombination rate. The dynamics can be then simplified to

- constant dissociative ionization and attachment rates, k_{ion} and k_a ;
- ion-ion recombination rates, which must fulfill $k_{i-i-r} = k_a$ for $t \gg \tau$.

Table 3.7: Reaction channels considered in chemical modeling: F- and H-atom reactions

no.	educts	products	k_2
74.	$C_2F_3 + F$	$\rightarrow C_2F_4$	1.0×10^{-12} [80]
75.	$C_2F_4 + F$	$\rightarrow CF_3 + CF_2$	5.0×10^{-11} [9]
76.	$C_2F_5 + F$	$\rightarrow CF_3 + CF_3$	2.2×10^{-11} [80]
77.	$C_2F_6 + F$	$\rightarrow CF_3 + CF_4$	1.0×10^{-11} [80]
78.	$C_2HF_5 + F$	$\rightarrow C_2F_5 + HF$	6.3×10^{-12} [9]
79.	$C_3F_6 + F$	$\rightarrow CF_3 + C_2F_4$	2.0×10^{-11} [80]
80.	$C_3F_6 + F$	$\rightarrow C_2F_5 + CF_2$	2.0×10^{-11} [80]
81.	$CF + F$	$\xrightarrow{M} CF_2$	6.2×10^{-15} [13]
82.	$CF_2 + F$	$\xrightarrow{M} CF_3$	5.1×10^{-13} [13]
83.	$CF_3 + F$	$\xrightarrow{M} CF_4$	1.7×10^{-12} [14]
84.	$CH_2F_2 + F$	$\rightarrow CHF_2 + HF$	6.7×10^{-12} [9]
85.	$CHF + F$	$\rightarrow CF + HF$	5.0×10^{-11} [80]
86.	$CHF_2 + F$	$\rightarrow CF_2 + HF$	5.0×10^{-11} [9]
87.	$CHF_2CHF_2 + F$	$\rightarrow CHF_2CF_2 + HF$	1.3×10^{-11} [9]
88.	$CHF_3 + F$	$\rightarrow CF_3 + HF$	1.5×10^{-13} [9]
89.	$CHF_2CF + F$	$\rightarrow CHF + CF_2$	1.7×10^{-11} [9]
90.	$CHF_2CF_2 + F$	$\rightarrow C_2F_4 + H$	3.3×10^{-12} [9]
91.	$CHFCHF + F$	$\rightarrow CHF_2CF_2 + H$	6.6×10^{-11} [9]
92.	$F + F$	$\xrightarrow{M} F_2$	1.2×10^{-17} [107]
93.	$CF_2 + F_2$	$\rightarrow CF_3 + F$	2.0×10^{-15} [9]
94.	$C_2F_5 + H$	$\rightarrow C_2F_4 + HF$	6.0×10^{-12} [9]
95.	$CF + H$	$\rightarrow CH + F$	1.9×10^{-11} [9]
96.	$CF_2 + H$	$\rightarrow CF + HF$	4.1×10^{-11} [9]
97.	$CF_2CF + H$	$\rightarrow C_2F_2 + HF$	7.3×10^{-11} [9]
98.	$CF_2CF + H$	$\rightarrow CHF_2CF_2$	2.1×10^{-11} [9]
99.	$CF_2CH + H$	$\rightarrow C_2HF + HF$	7.3×10^{-11} [9]
100.	$CF_2CH + H$	$\rightarrow CH_2CF_2$	2.1×10^{-11} [9]
101.	$CF_3 + H$	$\rightarrow CF_2 + HF$	9.1×10^{-11} [9]
102.	$CF_3CH_2 + H$	$\rightarrow CH_2CF_2 + HF$	1.0×10^{-10} [9]
103.	$CH_2CF_2 + H$	$\rightarrow CF_2CH + H_2$	2.5×10^{-21} [9]
104.	$CH_2F_2 + H$	$\rightarrow CHF_2 + H_2$	6.2×10^{-18} [9]
105.	$CHF + H$	$\rightarrow CH + HF$	4.9×10^{-10} [9]

Table 3.8: Reaction channels considered in chemical modeling: F- and H-atom reactions, continued

no.	educts	products	k_2
106.	$\text{CHF}_2 + \text{H}$	$\rightarrow \text{CHF} + \text{HF}$	1.1×10^{-10} [9]
107.	$\text{CHF}_2 + \text{H}$	$\rightarrow \text{CF}_2 + \text{H}_2$	1.8×10^{-14} [9]
108.	$\text{CHF}_2\text{CF}_2 + \text{H}$	$\rightarrow \text{CHF}\text{CF}_2 + \text{HF}$	1.0×10^{-12} [9]
109.	$\text{CHF}_2\text{CH}_2 + \text{H}$	$\rightarrow \text{CHF}_2\text{CH}_2 + \text{H}$	1.2×10^{-16} [9]
110.	$\text{CHF}_2\text{CHF} + \text{H}$	$\rightarrow \text{CHFCHF} + \text{HF}$	3.5×10^{-11} [9]
111.	$\text{CHF}_2\text{CHF} + \text{H}$	$\rightarrow \text{CH}_2\text{CF}_2 + \text{HF}$	1.3×10^{-11} [9]
112.	$\text{CHF}_3 + \text{H}$	$\rightarrow \text{CF}_3 + \text{H}_2$	5.2×10^{-19} [9]
113.	$\text{CHF}\text{CF} + \text{H}$	$\rightarrow \text{C}_2\text{HF} + \text{HF}$	7.3×10^{-11} [9]
114.	$\text{CHF}\text{CF} + \text{H}$	$\rightarrow \text{CHFCHF} +$	2.1×10^{-11} [9]
115.	$\text{CHF}\text{CF}_2 + \text{H}$	$\rightarrow \text{CF}_2\text{CF} + \text{H}_2$	1.2×10^{-21} [9]
116.	$\text{CHFCHF} + \text{H}$	$\rightarrow \text{CHF}\text{CF} + \text{H}_2$	1.2×10^{-21} [9]
117.	$\text{F}_2 + \text{H}$	$\rightarrow \text{F} + \text{HF}$	1.8×10^{-12} [9]
118.	$\text{H} + \text{H}$	$\rightarrow \text{H}_2$	1.8×10^{-16} [108]
119.	$\text{CF}_3 + \text{H}_2$	$\rightarrow \text{CHF}_3 + \text{H}$	3.9×10^{-19} [9]
120.	$\text{F} + \text{H}_2$	$\rightarrow \text{HF} + \text{H}$	2.5×10^{-11} [9]
121.	$\text{CH} + \text{HF}$	$\rightarrow \text{CF} + \text{H}_2$	5.0×10^{-11} [9]
122.	$\text{CHF} + \text{HF}$	$\rightarrow \text{CH}_2\text{F}_2$	1.9×10^{-13} [9]

k_2 in cm^3s^{-1}

In the argon-CHF₃ gas mixture, the major positive ions are argon ions, followed by CF₃⁺ and CHF₂⁺. Dissociative ionization yields additional amounts of H and F. Attachment, which results in the formation of F⁻, yields byproducts which are not well documented in the literature. Here, it is assumed that the major product is CHF₂ similar to the electron-collision induced dissociation producing CHF₂ + F. Ion-neutral reactions were not included for reasons stated in Section 1.3.3.3.

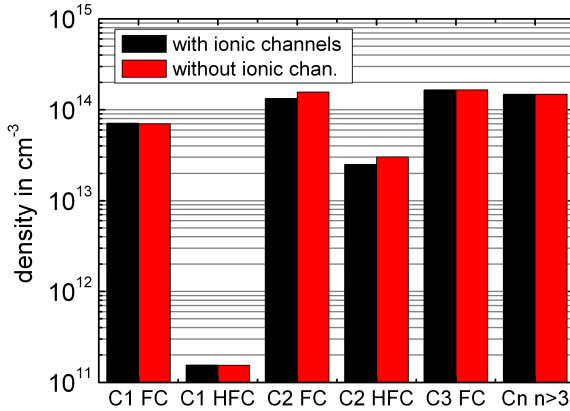


Figure 3.21: Numerical simulation of a plasma discharge (20 W, cw, 10sccm CHF₃, 60sccm Ar, 80 Pa). The number indicates the number of carbon atoms in the molecule. FC: pure fluorocarbons, HFC: hydrofluorocarbons.

The differences of whether ionic channels are included in the simulation or not are depicted in Figure 3.21. For C₁, only radicals were considered. For $n > 1$, saturated and unsaturated species were both included. The differences are in the range of about <20% peak for molecules C₂-backbones, whereas neither the single-carbon radicals nor oligomers with $n \geq 3$ are affected. In all cases, the ratio $r_{FC/HFC}$ is not affected as well. Due to the lack of precise knowledge about the byproducts resulting from dissociative attachment, the ionic channels were excluded for the subsequent simulations. The error by doing so is probably less than 10%, which is the percentage of the ionic dissociation channels compared to the neutral ones.

Chapter 4

Comparison between modeling and experimental results

The power-voltage characteristics resulting from the probe measurements are compared with those obtained from the particle dynamics simulations. Furthermore, the electron density and its dependence on plasma conditions is evaluated from both experimental and simulation results. A comparison to electron density measurements is included in order to check the validity of the simulations. Changes in the electrical parameters of the discharge, which are observed in the experimental data, are also discussed.

Small carbon species are monitored by laser-induced fluorescence, as they indicate on chemical processes within the discharges which may feed back the physical processes. Diffusion is observed and diffusion coefficients are determined from the experimental data and surface fluxes are identified. Mass spectrometry completes the experimental tracking of processes on a molecular scale. Accompanying chemical simulations of the discharge are partially based on results from the previous sections, but also experimental data. The chapter closes with a comparison between observed polymer deposition and chemical modeling to show the consistency of the obtained picture of the plasma.

4.1 Results of particle dynamics in simulation and experiment

The outcome from SIGLO-RF contains the attachment and ionization rates, the densities, potentials, fields, and currents in temporal and spatial resolution. The resulting mean electron energy can be used to estimate the rates of dissociation in the discharge from Chapter 1.2.4. In addition, the ion currents towards the electrodes allow to account for ion neutralization

and polymer sputtering as a potential source of reactive neutrals, which is of relevance in the interpretation of experimental results shown in Section 4.2. To probe the predictions of the model, the results are compared to measurements of the electrical parameters as well as optical emission data.

4.1.1 Comparison of electrical discharge characteristics

Experimental and simulated power-voltage (PU) characteristics of pure argon discharges are compared in Figure 4.1. The data were acquired by the UI probe and the high-voltage probe as described in Section 2.1. The characteristics show that by increasing the discharge voltage, the power increases. This is shown for 30 and 60 Pa.

At 30 Pa, an excellent agreement is found between the simulated values and voltages as obtained by high-voltage probe oscilloscope measurements. The UI probe shows deviations increasing especially at high voltages. These deviations result from errors in the phase lag measurement of about 2° in combination with the phase lag in the range of 86 - 87° . Experimentally, under such conditions, the power measurement even becomes sensitive to the position of cables etc..

In the data representing the discharge at 60 Pa, at about 80 V, the discharge rapidly switches to an abnormal glow around the edges of the electrodes, and the voltage drops to 72 V. By then decreasing the forward power, the initial curve is reached at about 60 V, resulting in a power-voltage hysteresis. As this phenomenon is related to the reactor setup, it can not be considered in the modeling with SIGLO-RF. Besides that, experiment and simulation show good agreement.

Next, experiments and simulations were carried out in a pure CHF_3 plasma. The results are plotted in Figure 4.2. The error-bars are much smaller than in the case of discharges in argon, which is due to a phase lag of 60 - 70° . The simulation at 30 Pa yields acceptable results, here, the PU characteristics are slightly above the predicted values, but are confirmed by the oscilloscope measurements. Contrarily, when the pressure is increased to 60 Pa, large deviations beyond the error bars are observed. Unlike to the discharges in pure argon, the high-voltage probe measurements this time confirm the PU data. Furthermore, the deviation between the simulated and experimental data is not constant in time. It is found that after ignition, a time-dependent change in the power-voltage characteristics occurs. Depending on the plasma conditions, it may take several seconds until a stable state is achieved. These data are plotted in Figure 4.3: the brown

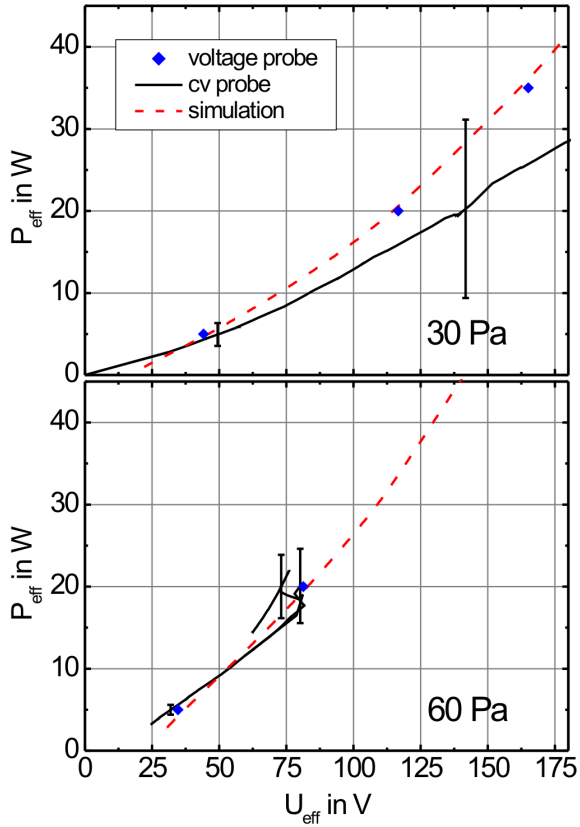


Figure 4.1: Comparison between experimental and simulated argon plasmas at 30 Pa (top) and 60 Pa (bottom). Large errors in experimental data result from a phase lag close to 90° , but oscilloscope measurements and simulations match up perfectly.

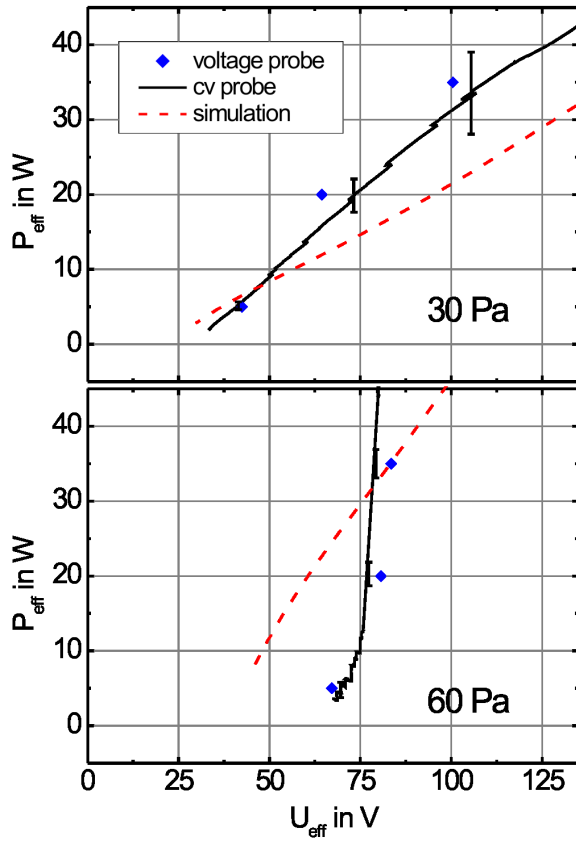


Figure 4.2: Comparison between experimental and simulated CHF_3 plasmas at 30 Pa (top) and 60 Pa (bottom). Differences between simulated and experimental data are seen. This is due to a time-dependence of the discharge characteristics, see text.

hollow circles correspond to the temporal progression. Here, an increase in the point density directly corresponds to the convergence of the data in time; the time-stepping is 100 ms between each point. In addition, a dotted line is added, connecting and extrapolating the initial points of the supplementary data. This line is only a guide to the eyes, showing the initial point locus. The values obtained upon slowly increasing the plasma power are plotted as black, solid line, and correspond to the steady-state characteristics.

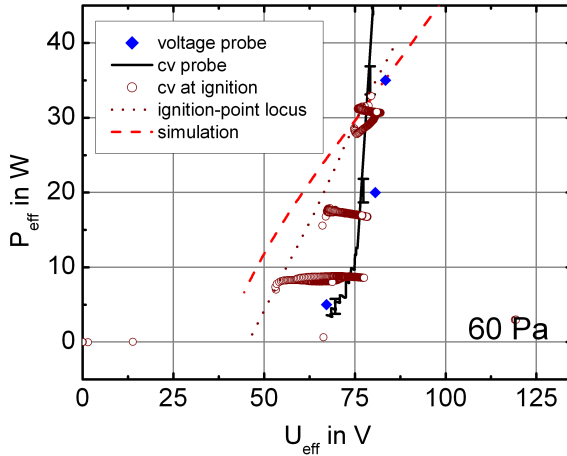


Figure 4.3: Temporal development of the plasma power vs. applied voltage, comparison between simulation and experiment. At the plasma ignition, a good agreement between simulation and experiment is seen (dashed and dotted line), while the measured steady-state characteristics deviate (black, solid line). Discharge in pure CHF_3 at 60 Pa.

Further comparative experiments and simulations were carried out at CHF_3 flows of 5 sccm (Figure 4.4), 10 sccm (Figure 4.5), and 15 sccm (Figure 4.6) at each three different pressures (60, 80, and 100 Pa). The argon flow was kept constant at 60 sccm. In general, the PU characteristics are time-dependent like in the case of discharges in pure CHF_3 .

Furthermore, the steady-state curve intersects the curve of ignition-point locus. At this intersection point, the power-voltage characteristics are time-independent. This point shifts towards higher voltages and higher powers when the pressure or the flow of CHF_3 are increased. Below the inter-

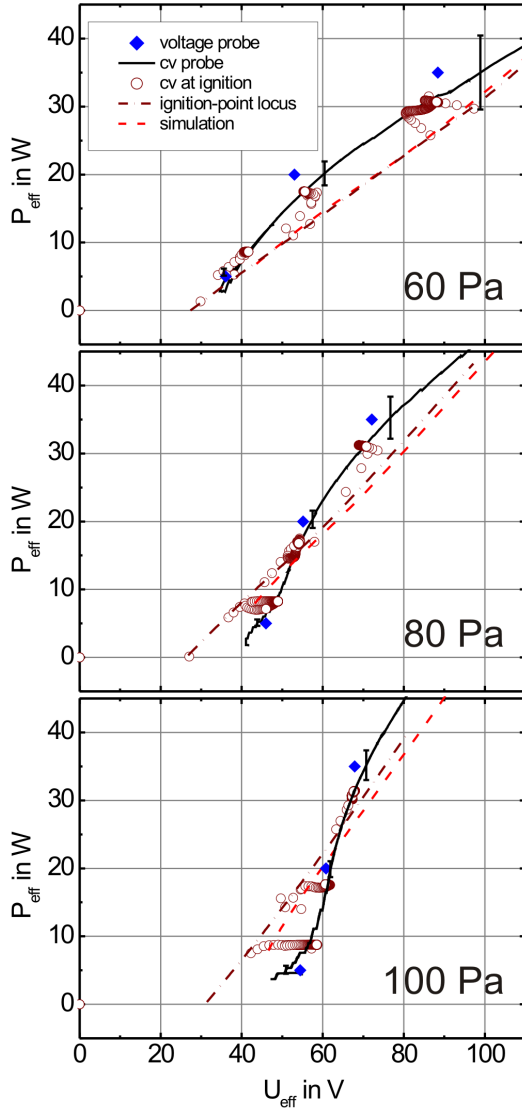


Figure 4.4: Plasma parameters at 5 sccm CHF_3 flow. Measured and simulated PU characteristics at 60, 80, and 100 Pa. For further details, see text.

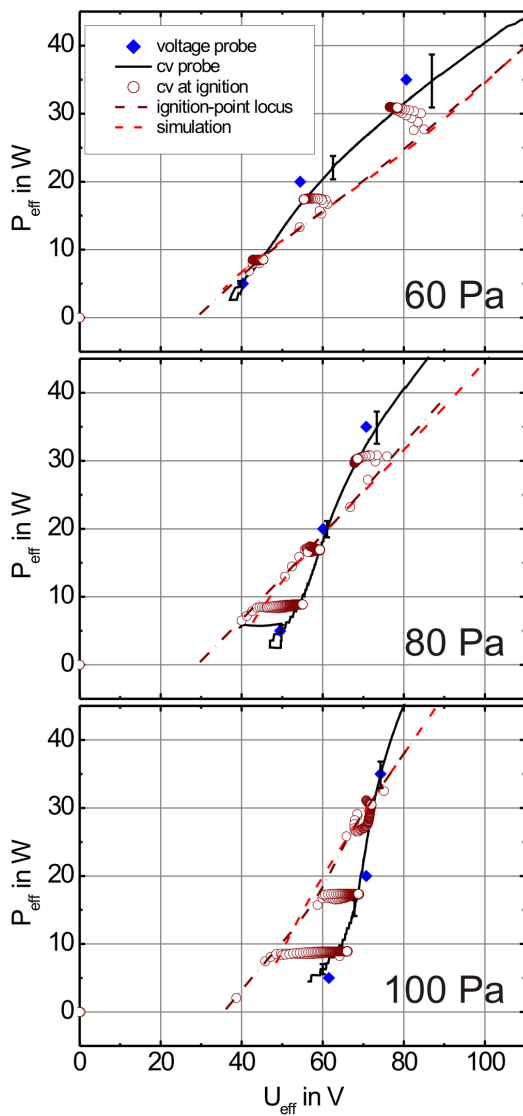


Figure 4.5: Plasma parameters at 10 sccm CHF_3 flow. Measured and simulated PU characteristics at 60, 80, and 100 Pa. For further details, see text.

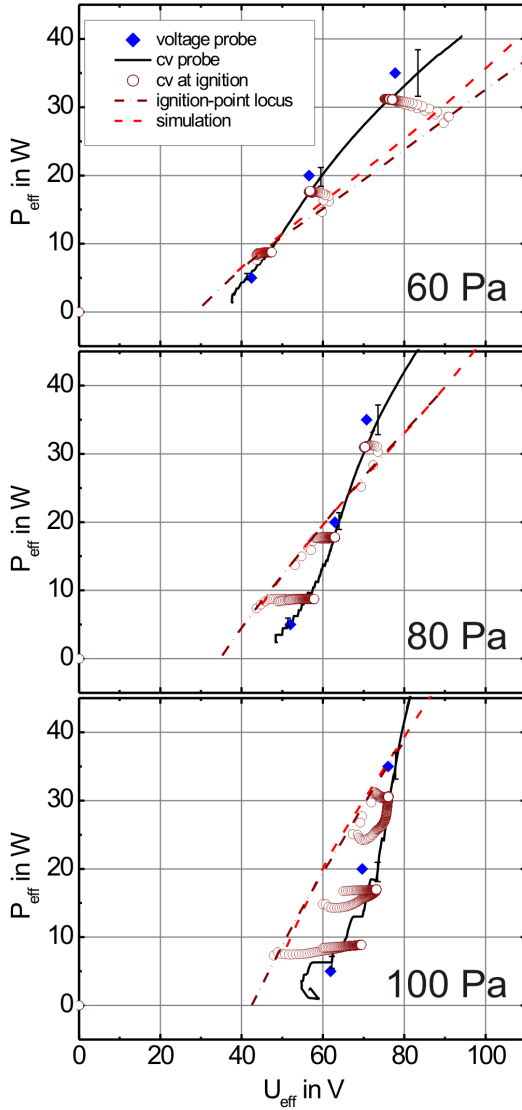


Figure 4.6: Plasma parameters at 15 sccm CHF_3 flow. Measured and simulated PU characteristics at 60, 80, and 100 Pa. For further details, see text.

section points, at constant powers, the discharge voltage increases during the plasma glow, in other words, the ohmic resistivity increases with time. Above the intersection point, the opposite is the case.

By microwave interferometry, it is found that the electron density is constant in time within the precision of the device (not shown). As the electron current is the major contributor to the electrode currents, most likely, time-dependent changes in the electron mobility are the reason for the time-dependence of the discharges characteristics:

$$j_e = n_e e v_d = \underbrace{n_e}_{const.} e \mu E \quad (4.1)$$

The mobility μ depends on the collision cross sections and local charge densities (ambipolar diffusion). On one hand, the time-dependent characteristics could be explained by the build-up of ion concentrations (both positive and negative ones) within the range of several seconds. On the other hand, the time scale of the observed changes is larger than expected from simulations in SIGLO-RF: In the simulations, an equilibrium of electrons as well as both negative and positive ions is already achieved in less than a millisecond. The time for building-up the steady-state ion densities, t_b , is according to simulations commonly less than 0.3 ms, which matches with a crude estimate from the rates and densities of about $t_b = 0.1$ ms (calculation basis: $k_{ioniz.} = 10^{-11} \text{ cm}^3 \text{ s}^{-1}$, $n_e = 5 \times 10^8 \text{ cm}^{-3}$, $n_n = 2 \times 10^{16} \text{ cm}^{-3}$, $n_i = 10^{10} \text{ cm}^{-3}$, $n_i = k_{ioniz.} n_n n_e t_b$). Moreover, the observed time scale is much more typical for chemical processes such as oligomerization and/or dissociation in a low-pressure plasma environment (milliseconds to seconds).

4.1.2 Comparison of the electron density and its distribution

During the ignition experiments discussed in the previous section it was found that the electron density is constant. Also in pulsed discharges, the steady-state value measured after a short ignition period turned out to be independent of the duration of the plasma-on time (not shown). Such, n_e was found not to be a function of the voltage applied to the electrodes, but to be a function of the plasma power, such that $n_e = n_e(P)$.

In Figure 4.7, simulated and measured electron densities are shown. The electron densities shown were measured in pulsed discharges with duty cycles of around 50% and $T = 100/500$ ms, and are plotted against the

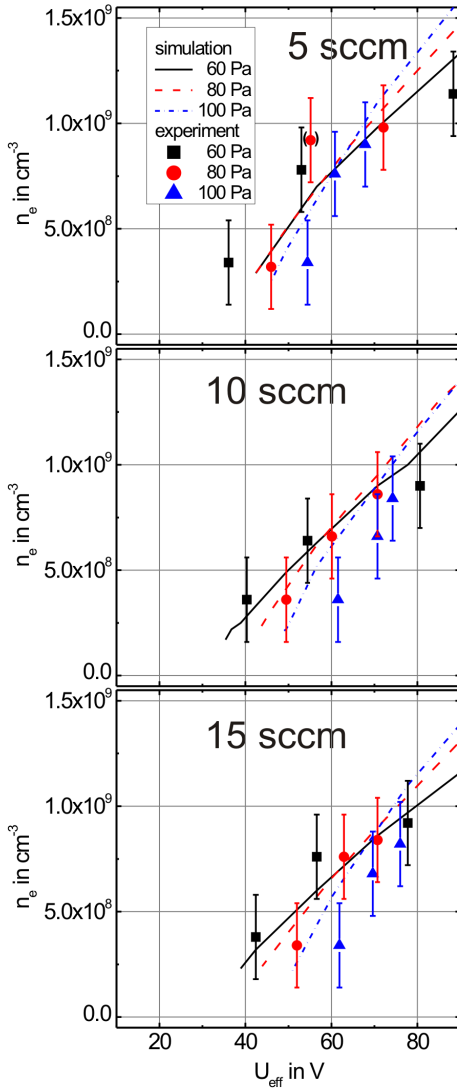


Figure 4.7: Comparison of the electron-density dependence on plasma power, simulated and measured. The argon flow was 60 sccm in all cases.

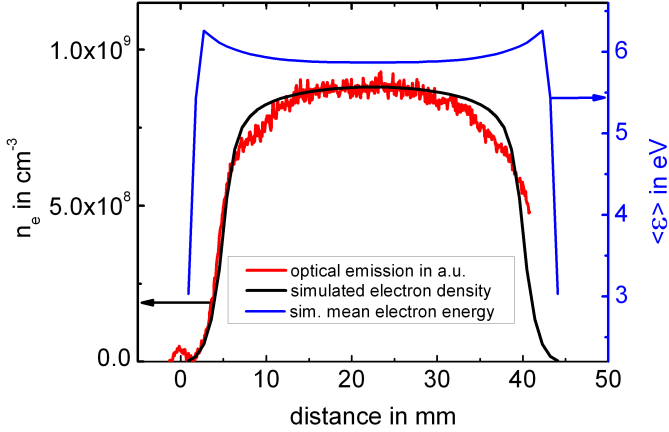


Figure 4.8: Optical emission data (acquired from background measurements for LIF, red) in comparison to the numerically determined axial electron density (black) and the mean electron energy, $\langle \epsilon \rangle$. See text.

corresponding cw discharge voltage. The data points of one series, from left to right, roughly correspond to 5, 20, and 35 Watt power. The differences between the simulated and experimental $n_e(P)$ arise partially from the time-dependent changes of the $P(U)$ characteristics, which are discussed in the previous section. Furthermore, the electron density was close to the lower detection limit of the interferometer. However, the general tendencies of the simulation can be also seen in the experimental data. These are the lowering of the electron density at high voltages upon increasing the CF_3 flow as well as the intersections of the different isobars. This is best seen in the data obtained at 10 sccm, when the 5 and 35 W data points, corresponding to the lowest and the highest voltages, are compared.

As a further comparison between simulation and experiments, axial-resolved optical emission measurements were performed in the UV range. Such, the complete height between the reactor electrodes were monitored. The optical emission intensity I is roughly given by

$$I(z) = \iint k_{ex}(\langle \epsilon \rangle) n_{em}(\vec{x}) n_e(\vec{x}) dx dy, \quad (4.2)$$

where $k_{ex}(\langle\epsilon\rangle)$ is the excitation rate coefficient and n_{em} denotes the density of the emitting molecule (or atom)¹. In the examined wavelength range, the major emitter is CF_2 . The density distribution $n_{em}(\vec{x})$ of CF_2 was determined in Section 2.2.4. The emission is assumed to be mainly due to electronic excitation by electron impact [109] and relaxation according to the selection rules. Such, the emission intensity mainly depends on the mean electron energy and the electron density. The comparison between simulated electron density and measured emission data is depicted in Figure 4.8, together with the simulated mean electron energy. It is seen that the simulated mean electron energy is about constant in the middle of the reactor, before shortly increasing and then sharply dropping towards the electrodes (located at 0 mm and 45 mm). In the range where $\langle\epsilon\rangle$ changes, no emission is observed. Such, the emission profile shown is not related to the distribution of the mean electron energy. Instead, a good agreement between the simulated electron density profile and the optical emission profile is seen.

Finally, for the comparison of simulated plasma parameters with experimental ones, Langmuir probe measurements were started. However, the probe measurements to determine $\langle\epsilon\rangle$ and $f(\epsilon)$ with a Hiden Espion Langmuir probe completely failed, even though cleaning cycles were carried out: depositing plasmas like CHF_3 plasmas are known to hardly allow probe measurements. This was examined in inductively-coupled plasmas (icp) by Hebner and Miller in [102]. In the capacitively coupled plasma (ccp) used here, even measurements in pure argon plasmas failed. It was found that results could be manipulated arbitrarily: Such, by variation of grounding and shielding, the electron temperature could be changed by 1 – 2 eV. This is attributed to stray fields. In other setups, Langmuir probes are much easier to apply: In a $\text{CHF}_3 + \text{CH}_4$ icp in a completely shielded bell-jar vessel, Langmuir probe measurements show an increase in the electron temperature upon increasing the power according to Gaboriau *et al.* [110]. But due to the completely different conditions in icps and other different geometries, results are by far not comparable to a ccp as used here. Much more, the simulation results resemble those obtained in argon by optical emission spectroscopy [111] (13.56 MHz, ccp) and hair-pin probe measurements [112] (80 MHz, ccp).

¹Quenching is not considered for simplicity. The lifetime τ of the excited state is assumed to be small, such that drift path $v \times \tau$ until emission occurs is negligible compared to the spatial resolution of the detector.

4.2 Gas phase kinetics of CF_x species

Space- and time-resolved densities of CF and CF_2 were observed by linear laser-induced fluorescence. In the following sections, the kinetics are presented exemplary for pulsed plasmas with gas flows of 10 sccm CHF_3 and 60 sccm argon at a pressure of 80 Pa. Energy was supplied by 20 W radio-frequency (rf). The pulsing was done with a duty cycle of 35% and a pulse period of 100 ms. The results are plotted in Figures 4.9 and 4.12 for CF and CF_2 , respectively. In both cases, about half of the reactor height was monitored. As shown before in Section 2.2.4, the density profiles (here obtained as height cross sections) are completely symmetric with respect to the reactor center plane at $z = 22.5$ mm and consequently, the measured half profiles represent the density profiles between the electrodes. The experiments were carried out with preconditioned reactor walls, i.e. after cleaning of the device in hydrogen and oxygen plasmas, the walls were exposed at least three minutes to the to-be-examined plasma prior to the measurements. If not stated differently, no substrates were used.

4.2.1 CF temporal and spatial development

From Figure 4.9 we conclude that the CF radical is created homogeneously in the gas phase within the first 10 ms of the plasma pulse. After the plasma is switched off, it decays very fast. The maximum production rate in the beginning of the pulse is around $8 \times 10^{14} \text{ cm}^{-3}\text{s}^{-1}$, the decay appears to be exponential ($c(t) = c_0 e^{-\kappa t}$ with $\kappa = 2.02 \times 10^4 \text{ s}^{-1}$).

During the plasma-on time, the density rises steeply within the first ten milliseconds of the plasma pulse. Roughly, the rising follows a $c(t) = c_0(1 - e^{-kt})$ law. The resulting rates are by far larger than those which result of primary dissociation from the particle dynamics simulation in Section 3.2.3, such that they must be attributed to chemical reactions. These reactions involve e.g. H-atom induced dissociation and require advanced modeling (see Chapter 3.3). Only in the early glow, a slight inhomogeneity in the density and a gradient towards the electrodes is noticed in Figure 4.10, which is presumably due to surface losses.

The afterglow kinetics of CF are governed by a fast and isotropic decay (Figure 4.11). It can be fitted by an exponential function at the early stage, such that the reaction rate would be of pseudo-first order. However, the kinetics are more complex. Several reactions can take place, which are introduced in Sections 1.3.3.1 and 3.3, and are modeled in Section 4.2.3.

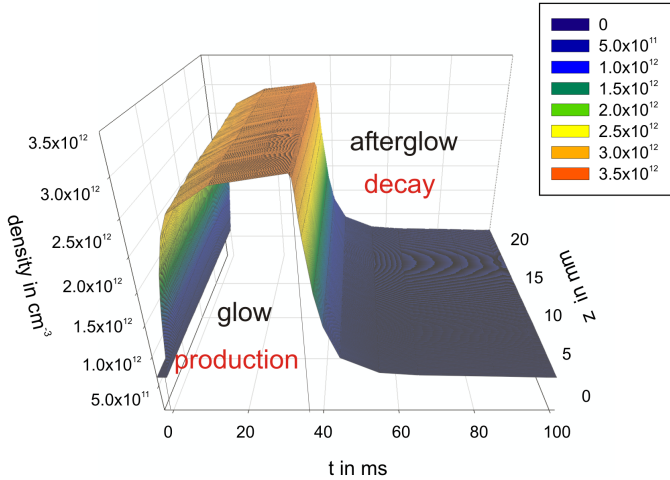


Figure 4.9: Space- and time-resolved development of the CF density as monitored by LLIF. Half-height of the reactor was scanned. In the plasma-on time ("glow"), the concentration rises isotropically within the first 10 ms. In the afterglow, the CF radical decays rather fast with an exponential-like function. The data were acquired under standard plasma conditions.

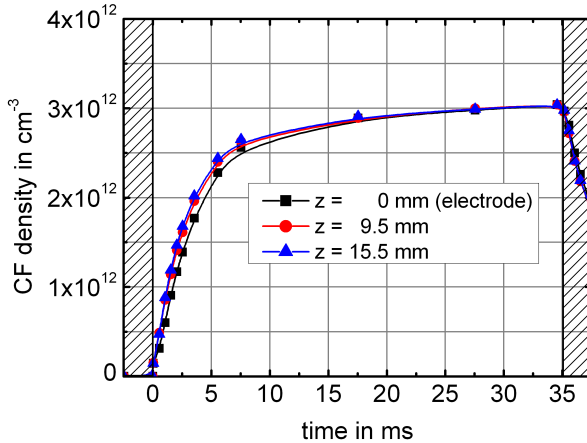


Figure 4.10: Cross-sectional plot of Figure 4.9 along the t-axis at different height. In the beginning of the discharge, a slight anisotropy is observed.

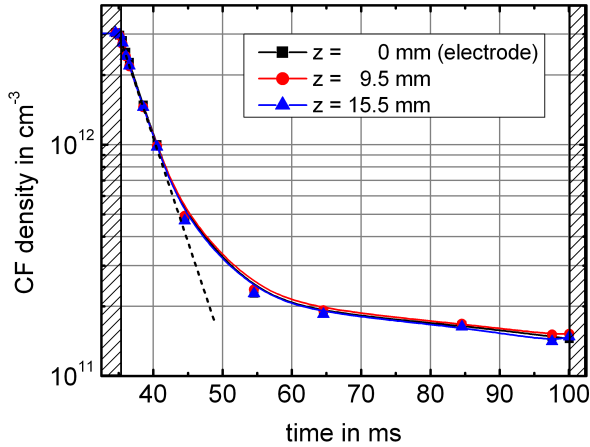


Figure 4.11: Semilogarithmic plot of the CF afterglow density. The initial decrease seems to be exponential, however, the kinetics are more complex. Data acquired under standard conditions.

4.2.2 Difluorocarbene temporal and spatial development

The metastable species CF_2 shows a more complex behavior, as can be seen in Figure 4.12. The density rises faster close to the electrode than in the plasma center. Thus, at the end of the glow, a profile results with a concave shape. It will be shown in Section 4.2.2.1 that the concavity results from diffusion processes. In the afterglow, reaction-diffusion kinetics are required to describe the temporal and spatial density distributions. In the early afterglow, a short over-shot is registered which is also documented in the literature [4]. Later on, the CF_2 density decays with non-exponential reaction kinetics, which are superimposed by diffusional processes. In the final state, the height cross section is nearly flat.

Time-resolved densities obtained by UV absorption and LLIF during a plasma pulse are shown in Figure 4.13 in comparison. The agreement between both methods is good, however, laser-induced fluorescence measurements are much less affected by errors (better signal-to-noise ratio) and allow much better spatial resolution in short acquisition times. For comparison: the measurement of the density in the center of the discharge with

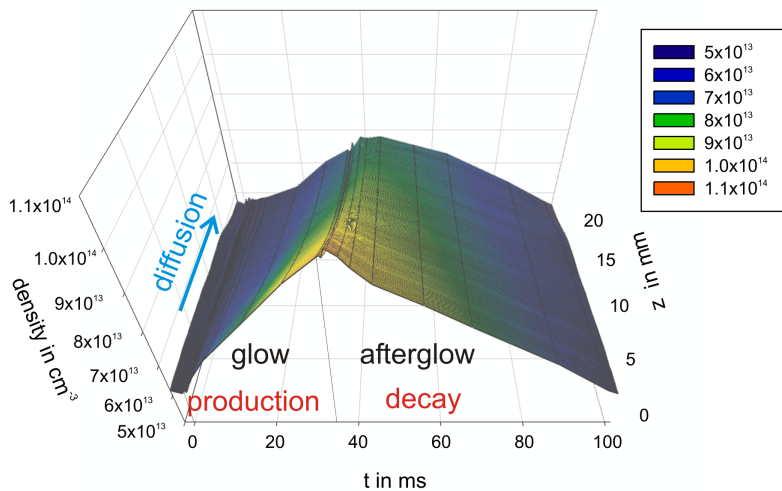


Figure 4.12: Space- and time-resolved development of the CF₂ density as monitored by LLIF. Half the height of the reactor was scanned. The electrodes are located at $z = 0$ mm and $z = 45$ mm (not shown). The data were acquired under standard conditions.

a 6 mm beam required approx. 900 s, whereas the LLIF measurement of a single density profile (theoretical resolution 60 μ m) required 20 s.

The density of CF₂ shows a strong increase mainly at the electrodes as shown in Figure 4.14. For the production of species after ignition, one might assume electron collision induced dissociation would be the source as stated in the literature for pulsed CF₄ plasmas [113]. However, the dissociation rates obtained in Chapter 3.2 are several orders of magnitude lower than the production rates measured here. In addition, the production rate is higher near or at the electrodes, and we suppose that CF₂ diffuses into the bulk plasma. Such, towards the center of the reactor, a concave profile results as seen in Figure 4.12. Compared to literature, such density profiles are often observed. Concave profiles were measured during the glow of fluorine-poor and fluorine-rich plasmas. The profile shape is attributed to strong fluxes of molecules from the electrodes into the plasma and/or volume loss processes. Convex shapes, which sometimes appear in the afterglow,

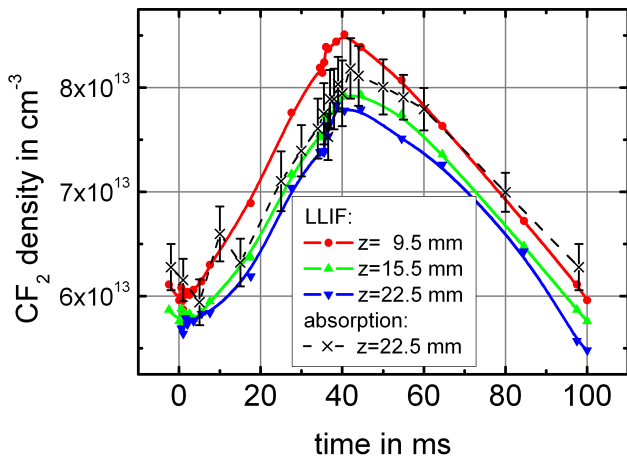


Figure 4.13: Time-resolved difluorocarbene absorption measurements in the center versus LLIF measurements at several different heights above the electrodes.

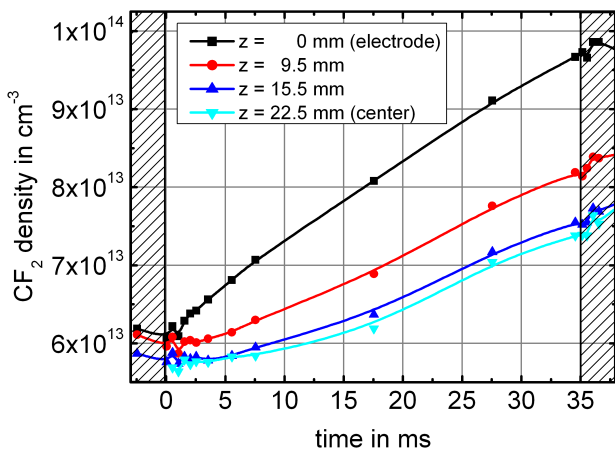


Figure 4.14: Cross sectional plot of Figure 4.12 along the t -axis at different height. Notice the fast density increase at the electrodes, which is about linear, and the delayed diffusion of species into the bulk.

are attributed to sticking to the surface and subsequent reactions. These profiles were measured under fluorine rich conditions (e.g. CF_4 discharges), which is neither observed nor the case here. The most origins of these processes have different characteristic time scales and are bound to several parameters. The reader is referred to Section 4.2.2.2 for more details. In the present study, we assume that wall production of CF_2 is the reason for the observed profiles.

4.2.2.1 Discussion of the gas-phase diffusion of CF_2 during the plasma-on phase

A CF_2 diffusion model was developed with two assumptions: first, the electrodes are the production region of the species as stated in the literature (see Section 4.2.6.2), second, reactions of CF_2 in the volume are considered to be isotropic and negligible compared to the wall production processes. It will be shown in Section 4.2.4.2 that this approach is justified. So pure diffusion as described by Fick's law can be assumed.

The axial density, expressed by the function $c(z, t)$, can not be solved analytically. Such, modeling was performed with Comsol Multiphysics 3.5, a solver for partial differential equations. The boundary conditions for the concentrations at the electrodes and in the volume are given by the following set of equations:

$$c(z, 0) = a(z - z_c)^2 + c_c \quad (4.3)$$

$$c(0, 0) = \underbrace{\left(\frac{az_c^2}{c_c} + 1 \right)}_{=a'} c_c \quad (4.4)$$

$$\begin{aligned} c(0, t) &= a' m_{a=0} t + c_c \\ &= m' t + a' c_0 \end{aligned} \quad (4.5)$$

An initial curvature ($a \neq 0$) of the axial density profile corresponds to persistent diffusion flows. As the time scales for diffusion processes are similar to the duration of the plasma pulse, the density profile could be largely affected. To account for this, an initial parabolic function is introduced for the density profile $c(z, t)$ in Equation (4.3). Here, z_c and $c_c(t)$ denote the center of the reactor and the center density, respectively. $c_c(0) = 1$ was set as initial condition in the simulations. The initial density at the electrodes is then given by (4.4). According to experimental results in Figure 4.14,

the density increases linear in time² with a function $m't$. The coefficient m' , as seen in Equation (4.5), depends on the initial profile curvature. The parameter a of the starting profile consequently affects the whole model. A value of $m_{a=0} = 1.02 \times 10^{15} \text{ cm}^{-3}\text{s}^{-1}$ resulted from fitting of the experimental data in Figure 4.14. The diffusion coefficient of CF_2 was obtained from literature data by using the Stefan relation (1.11) for the used gas composition and amounts $D = 0.88 - 1.09 \times 10^4 \text{ cm}^2\text{Pa s}^{-1}$. The value is larger than the diffusion coefficient in CF_4 [114, 115], $D = 0.83 \times 10^4 \text{ cm}^2\text{Pa s}^{-1}$. This is mainly due to the smaller collision cross section of argon.

Table 4.1: Simulation parameters for profile studies

simulation	a'
(a)	0.95
(b)	1
(c)	1.05
(d)	1.1

From the experimental data, a nearly flat starting profile was found, i.e. $a = 0$. But in order to study the effect of possible errors in the profile calibration on the spatial density development, a' was varied in a range from 0.95 to 1.1 (parameters of the simulation are given in Table 4.1). This corresponds to an error of -5% to +10% of the densities at the edges, which is comparable to the error bars in the experimental data (cf. Figure 2.11). The time-dependent development of the profiles is shown in Figure 4.15. In the plots, the initial densities are normalized with respect to the initial center density ($c_c(0) = 1$). The plots show data from 0 to 35 ms in time steps of 2.5 ms. In all plots, the concentrations increase monotonously at the electrodes, whereas in the center, the density first decreases in case of a convex starting profile (Figure 4.15, (a)). For a flat profile (graph (b)), the center density is constant for the first milliseconds. Afterwards, the diffusional flow $j = -D \frac{dp}{dx}$ reaches the center and the density increases. For starting conditions with a concave shape (graphs(c) and (d)), a diffusional flow is already present in the beginning and the center density increases immediately.

In order to determined which profile is appropriate, the time-dependent

²The flux of difluorocarbene will be introduced in the subsequent section after this phenomenological approach.

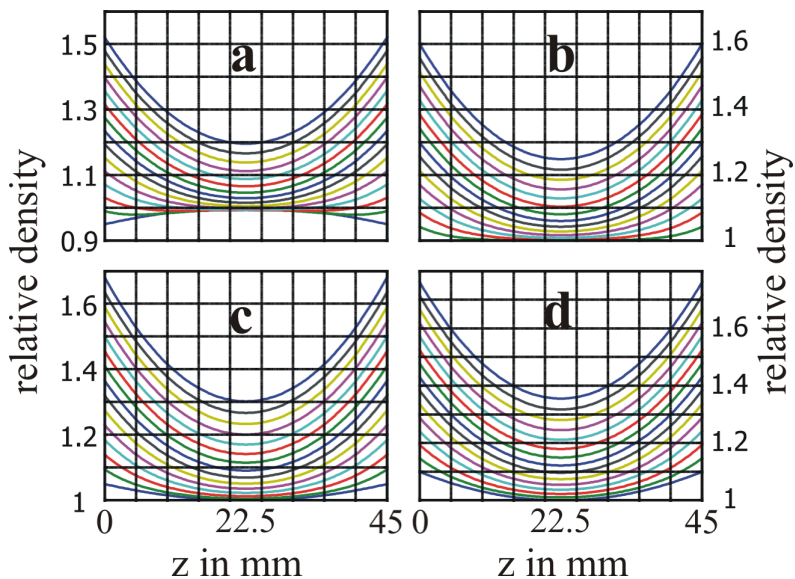


Figure 4.15: Time-dependent Comsol simulations for the profile development based on a pure diffusion model. The electrodes (located at 0 and 45 mm) act as sources. Parameters see Table 4.1. The initial center density is 1.

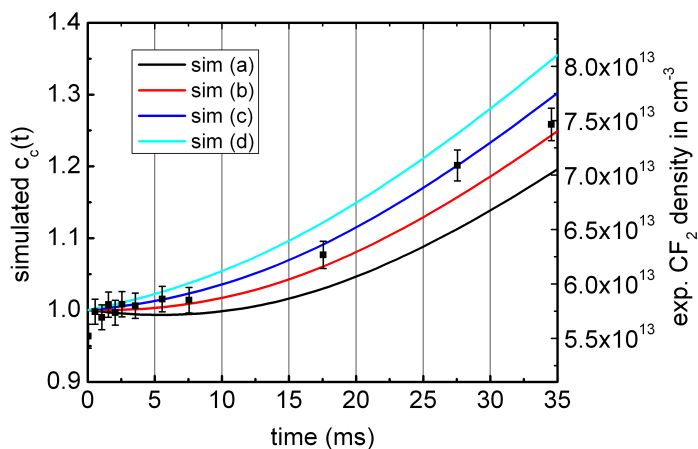


Figure 4.16: Experimental data of the center density in comparison to simulation results.

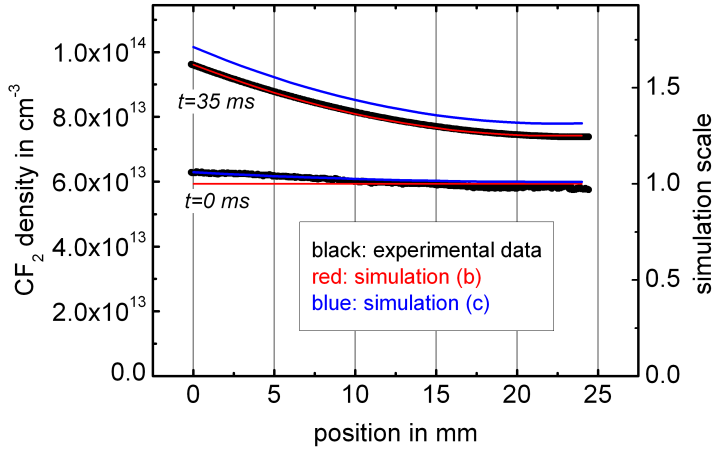


Figure 4.17: Comparison of experimental data of the initial and final CF_2 profiles to simulation results.

increase of center density $c_c(t)$ was compared to the experimental results, as depicted in Figure 4.16. Here, the red curve (b), corresponding to a flat initial profile, and the blue curve (c) for a slightly concave initial profile show the best agreement with the experimental data. Deviations may be due to chemical reactions taking place in the gas phase. The comparison of the simulated and measured initial and final density profiles is depicted in Figure 4.17. It confirms that the model parameters of the simulations (b) and (c) are appropriate to fit the experimental data within the whole reactor. The slight differences which are observed in the figure may be attributed to deviations from the linear fitting of the concentrations near the electrodes or effects arising from plasma chemistry.

The afterglow regime in the CF_2 density shows characteristic features (Figure 4.18). First, a short increase is observed, peaking at around 2-3 ms after the plasma is switched off. The increase is isotropic in the whole volume. After that, a pronounced decay is observed close to electrodes, whereas towards the center, continuous diffusion from the higher-populated sheath region partially opposes the chemical decay. It is not possible to perform meaningful fitting under these conditions without considering the complexity of plasma chemistry. Chemical modeling is required and more-

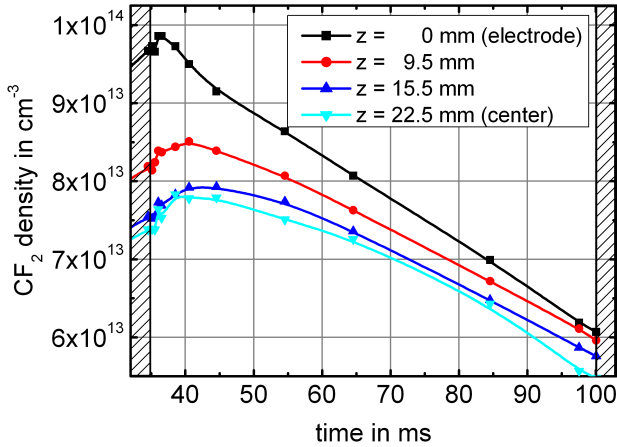


Figure 4.18: Afterglow decrease of the CF_2 density. The decay kinetics are a superposition of continuous diffusional flows towards the reactor center and chemical reactions. Data acquired under standard conditions.

over, diffusion kinetics have to be included as well, as a separation of both processes is not at all possible.

4.2.2.2 Diffusive flux of difluorocarbene

During the plasma glow, the increase of the concentrations close to or at the electrodes results in the observed concave profiles. Such, the diffusion fluxes $\Gamma(z, t) = -D \text{grad} \rho(z, t)$ from the electrodes ($z = 0, 45$) as the physical origin of diffusion have to be calculated for each data set in order to determine the underlying processes. In order to batch-process the calculation of the diffusional flows from the experimental data³, a generalized approximation for the concentration gradients is necessary. Therefore, the concentration gradients of the simulations shown in Figure 4.15 are plotted in Figure 4.19. The gradients show a slightly curved profile within some milliseconds after plasma ignition due to the complex, bend curvature of the density profiles as shown in Figure 4.15. But after the initial phase, the gradients can be approximated by a linear function with negligible errors, which, after

³In total, diffusion was determined from around 600-900 measured density profiles under different plasma conditions.

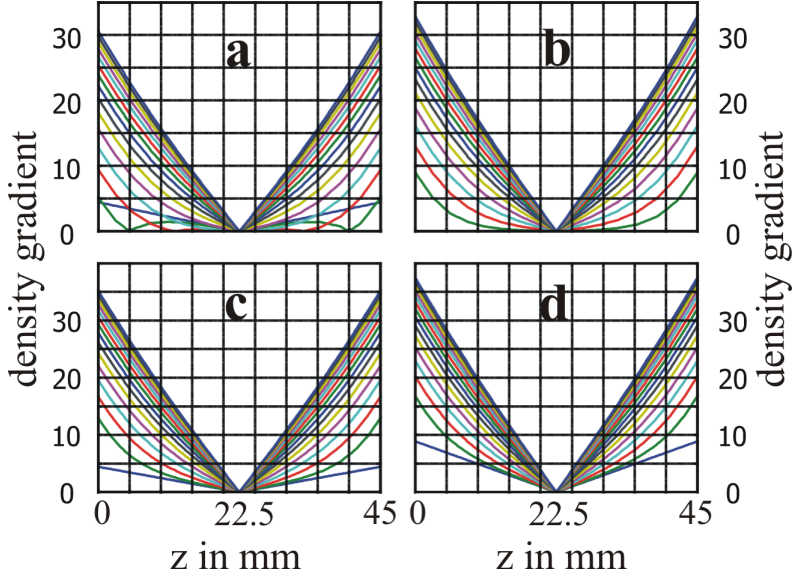


Figure 4.19: Concentration gradient plots of Figure 4.15. Parameters see Table 4.1.

integration, corresponds to parabolas as density profiles.

For the batch-processing, the gradients of the measured profiles were calculated and fitted linearly with $d\rho/dz = m(z - 22.5) + c$. The intersection of the linear regression with the ordinate as depicted in Figure 4.20 results in the flux after multiplication with D . The density profiles are supposed to be symmetric to the reactor center such that c is supposed to be zero. For regressions with $c \neq 0$, the intersection of a linear regression with equal m , but $c = 0$ was evaluated. The mean of both extrapolations was taken for the subsequent evaluation. The error bars correspond to the min/max values. To study the dynamics of the diffusion flow Γ_{CF_2} , the density profiles in pulsed plasmas were evaluated by the above methods.

For the plasma under standard conditions, the data are plotted in Figure 4.21. Here, it is seen that the flux increases during the plasma-on time and apparently starts to saturate. When the plasma is switched off, a short and steep increase is seen, followed by an exponential-like decay. The kinetics are further discussed with pulses of longer pulse periods, as the afterglow decay kinetics can be evaluated with higher precision. The dependencies of the flows on the plasma conditions in pulsed plasmas with $T = 500$ ms are

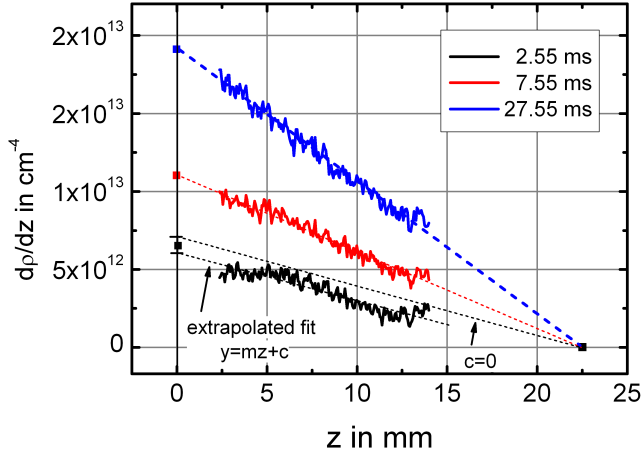


Figure 4.20: CF₂ density gradients in a plasma under standard conditions. The times given correspond to times after plasma ignition. The linear extrapolation of the gradients to the electrodes (here to the lower electrode at $z = 0$) allows the calculation of the diffusion flow starting in the electrode region. For more details, see text.

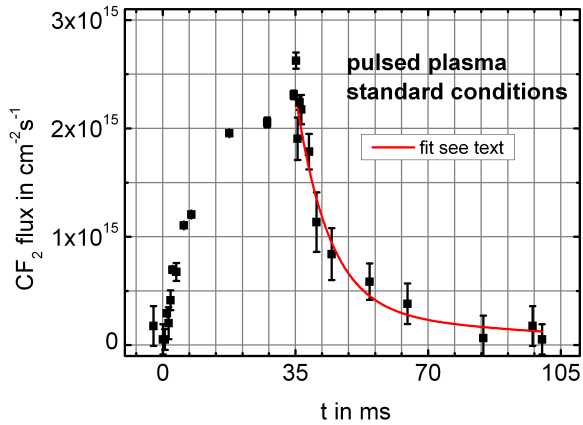


Figure 4.21: Γ_{CF_2} flux from the electrodes under standard plasma conditions. The afterglow kinetics are discussed in the text.

exemplary presented in Figures 4.22 and 4.23.

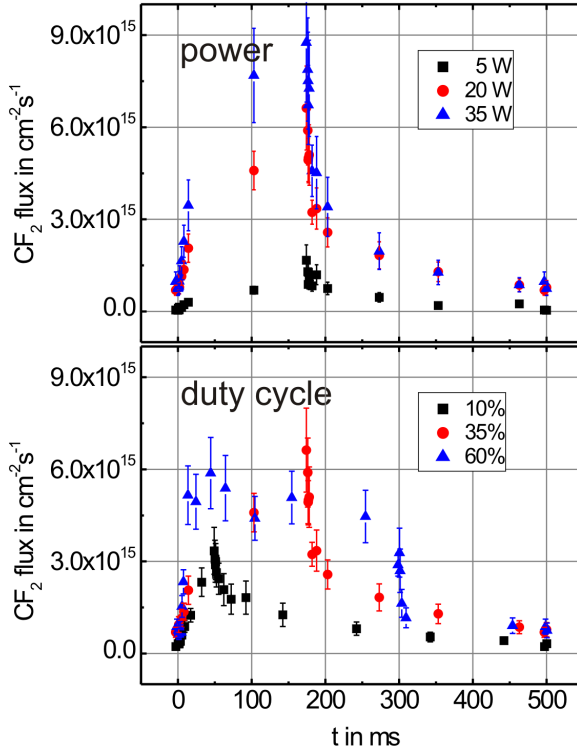


Figure 4.22: Γ_{CF_2} flux from the electrodes at variable power and duty cycle. F_{Ar} was constantly 60 sccm, the non-varied parameters were 20 W, 35%, 80 Pa, and $F_{\text{CHF}_3} = 10$ sccm.

As seen in Figure 4.22, top, the flux clearly depends on the plasma power: the higher the power, the higher the flux from the surface. The bottom graph shows that increasing the duty cycle results in a faster increase in Γ_{CF_2} .

According to the upper graph in Figure 4.23, a change in the monomer flow seems not to significantly affect the flux. At this point, it must be mentioned that this flow independence was not observed in all pulsed plasmas which were examined, especially in the low plasma power (5 Watt) regime. But deviations could be caused by ignition problems at these low

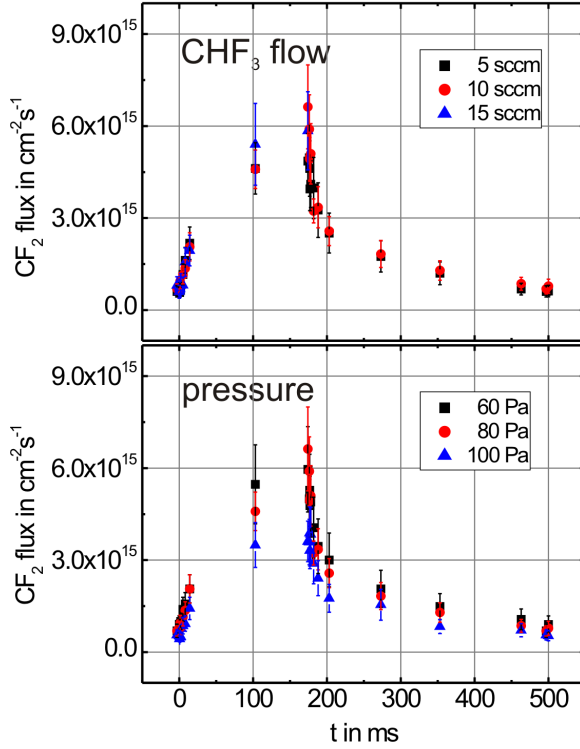


Figure 4.23: Γ_{CF_2} flux from the electrodes at CHF₃ flow and pressure. The argon flow was constantly 60sccm, the non-varied parameters were 20 W, 35%, 80 Pa, and 10 sccm.

powers and are therefore not further discussed. Furthermore, although the error bars are large, a trend towards a decrease in flux upon increasing the pressure can be seen in the top graph in Figure 4.23.

In general, Γ_{CF_2} increases during the plasma pulse and saturates after about 100 ms. In the afterglow, a decreasing, but continuous flux of difluorocarbene is observed. The physiochemical origin of these dependencies on the plasma conditions can not be identified at this point, a relation with the power available per molecule or atom, or electrode currents and/or radiation can be thought about at this point. More details can be found in Section 4.2.6.

The increasing flux during the plasma-on period does not follow any easily understandable scheme. However, the flux at the end of the glow depends on the surface coverage. For demonstration, experiments were carried out above blank and coated silicon wafers. Standard plasma conditions were applied and LLIF was carried out at $t = 34.5$ ms after the start of each pulse. The results are shown in Figure 4.24 - for comparison, data of CF are shown together with data of CF_2 . The kinetics of CF show a slight dependence on the surface coverage. As gas phase production is the source of the molecule (see Section 4.2.3), this dependence is probably only indirect via the dependence on one of the major precursors, namely CF_2 . Contrary to that, the density of difluorocarbene clearly depends on the surface coverage with plasma polymer. Above uncoated substrates, the density did not saturate even after 200 plasma pulses. After restarting the pulsing series with the wafer being precoated from the first sequence with about 1 nm plasma polymer, the steady state was reached after around 170 pulses, which then corresponds to a total polymer thickness close to 2 nm. In the final sequence with a starting thickness of slightly more than 2 nm, a steady state of the difluorocarbene density was reached already after 50 pulses. As the CF_2 center density mainly depends on Γ_{CF_2} , this flux and consequently the CF_2 production processes clearly depend on the surface coverage.

The afterglow flux in Figures 4.22 and 4.23 follows a specific decay scheme. It can be approximated by

$$\Gamma_{\text{CF}_2}(t) = a_1 e^{-(t-t_0)/t_1} + a_2 e^{-(t-t_0)/t_2} (+\Gamma_\infty) \quad (4.6)$$

(where Γ_∞ should be zero). Values for the parameters as listed in Table 4.2.

It is very important to notice that the use of a function like Equation (4.6) is only reasonable if both flux sources are *independent* of each other.

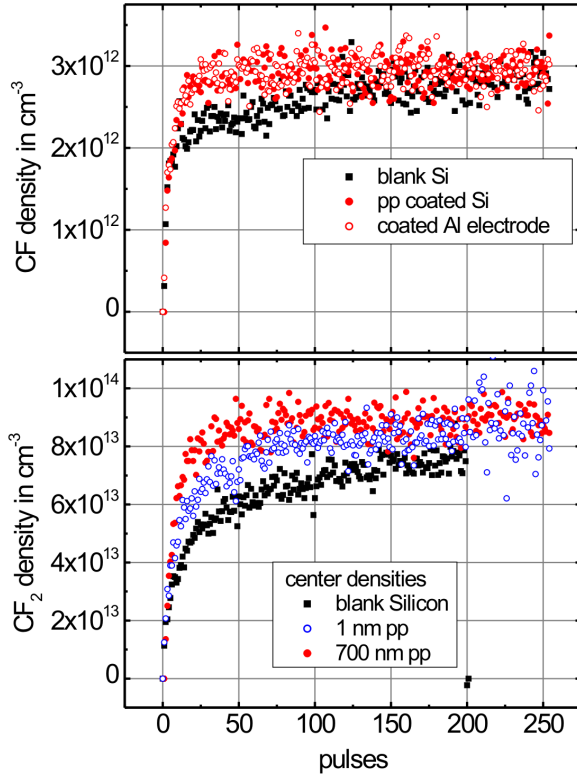


Figure 4.24: Graphs depicting the increases of the CF and CF₂ densities above blank and coated substrates in a series of plasma pulses.

Table 4.2: CF₂ afterglow flux, fitting parameters

v.p.	a_1^*	t_1 in ms	a_2^*	t_2 in ms
5 sccm	1.95 ± 0.98	11.97 ± 17.17	2.72 ± 0.95	215.17 ± 63.62
10 sccm	3.25 ± 1.10	5.21 ± 5.65	2.83 ± 0.66	239.42 ± 54.50
15 sccm	3.08 ± 0.93	12.08 ± 10.54	2.34 ± 0.87	260.92 ± 94.50
60 Pa	2.20 ± 1.13	8.59 ± 12.34	3.21 ± 0.97	233.65 ± 68.04
80 Pa	3.43 ± 1.41	4.59 ± 4.92	2.94 ± 0.77	229.10 ± 60.70
100 Pa	1.98 ± 1.12	10.1 ± 15.47	1.97 ± 0.99	256.04 ± 130.50
20 W	3.34 ± 0.28	5.25 ± 1.07	2.69 ± 0.14	249.65 ± 13.45
35 W	5.80 ± 0.22	9.14 ± 0.98	2.57 ± 0.14	281.27 ± 17.67
mean**	3.1 ± 1.2	8.4 ± 3.0	2.7 ± 0.38	245.7 ± 20.7

v.p.=variation parameter

* a_1, a_2 in $10^{15} \text{cm}^{-2} \text{s}^{-1}$

**errors calculated from standard deviation only.

Here, (at least) two sources are found, with characteristic decay times of 8.4 ± 3 ms and 245.7 ± 20.7 ms. Both sources have about similar strength ($a_1 \approx a_2$).

Alternative fitting with the 2nd order dimerization function according to Table 1.3 in Section 1.3.1

$$\Gamma_{\text{CF}_2}(t) = \frac{1}{k(t - t_0) + \Gamma_0^{-1}} + \Gamma_\infty,$$

which can have a similar appearance, does not describe the experimental data well. The values for the decay times were applied to several additional data sets with variations according to Table 2.1. The results of these peak fittings are not shown here, but all data could be fitted well with the above function (4.6) and the fitting parameters t_1 and t_2 given in Table 4.2. It was further found that, like seen in the fit parameters listed in Table 4.2, no significant and systematic changes of the a_2/a_1 -ratio in dependence of plasma conditions could be established, that means, the processes seem to be in general inherent to the system.

Consequently, we assume that at least two afterglow processes with quite different kinetics take place at the surface, which are probably also the origins of the difluorocarbene fluxes during the glow. But fitting of the glow data is much more complicated, as the processes and consequently the

flux limiting factor(s) in the beginning of the discharge is/are not known.

4.2.3 Modeling of kinetics of single-carbon species

In pulsed discharges, a simulation study was carried out to show the influence of variable duty cycle (10, 35, 60%) and variable pulse-periods ($T = 100, 500, 1000$ ms) on the density of chemical species. The other, following plasma conditions were kept constant, if not stated differently: 20 Watt power, 80 Pa total gas pressure, 60 sccm argon, 10 sccm CHF₃. The obtained kinetics are compared to the experimental results of the LIF measurements. By the chemical modeling, the chemical kinetics of small molecules as detected by LLIF allow to trace back the major processes taking place in the discharge. This is of relevance for the understanding of the time-dependent changes in the physical properties observed before in Section 4.1.

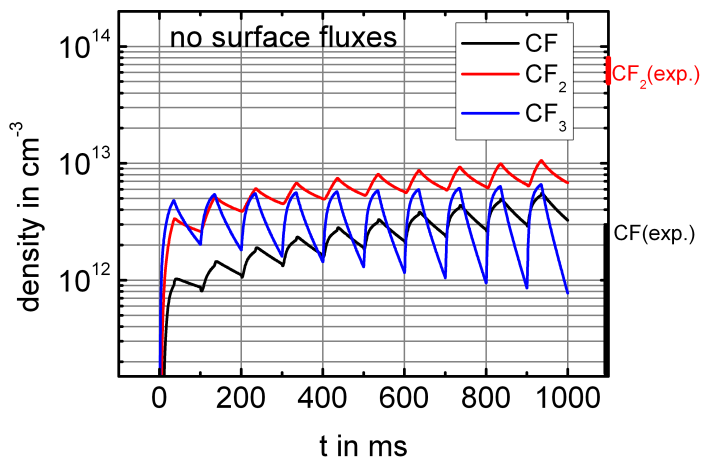


Figure 4.25: Pulsed plasma without surface fluxes. Black, solid line: CF; red, dashed: CF₂; blue, dotted: CF₃. The density is uniform within the plasma reactor.

The typical density profiles of CF₂ during a plasma pulse showed a strong inward diffusional flow of CF₂ (see Section 4.2.2). A model without inclusion of this flow is depicted in Figure 4.25. The CF density is close to the one observed in the experiments. The absolute density of CF₂ deviates from the measured one by one order of magnitude and further shows no

anisotropy. Including the diffusion flows obtained from profile fitting of the experimental data as performed in Section 4.2.2.2 results in a higher CF_2 density and in anisotropic density profiles (Figure 4.26, top). However, in this case, the CF_2 density is too high. The reason for this difference between the experiment and the simulation may be either the production of additional species e.g. at the electrodes or additional chemical processes taking place, or both of them.

4.2.3.1 Additional surface fluxes

As also stated in the literature, CF_3 radicals are produced at the surface under some conditions. For further details, see Section 4.2.6. These radicals affect the plasma chemistry, but their concentration could not be determined experimentally. To study the effect, these fluxes were tentatively introduced to the model by $\Gamma_{\text{CF}_3} = x \times \Gamma_{\text{CF}_2}$, $x = 0, 0.05, 0.5$ at the electrodes. The strongest changes are depicted in Figure 4.26. A flux $\Gamma_{\text{CF}_3} = 5\% \times \Gamma_{\text{CF}_2}$ results in a increase of the CF concentrations and same time in a decrease of the CF_2 density. This may be attributed to the competitive reactions of atomic hydrogen with CF_2 and CF_3 . As the plasma chemistry model used here contains 122 reaction channels so far, it is difficult to exactly trace back the origin(s) of these changes. The trend, however, continues when the CF_3 flux is further increased (see data for $x = 0.5$).

A detailed comparison of the modeled and experimental data (Figure 4.27) reveals that the model predicts the saturation of the CF density quite well. The simulated and measured densities differ by maximum a factor of 2 for $\Gamma_{\text{CF}_3} = 50\% \times \Gamma_{\text{CF}_2}$ during the glow. But in the afterglow, the decay of CF is seen to occur faster in the experimental data than in the model. The qualitative time-dependent changes of CF_2 of measured and simulated data agree well, although the absolute values differ. When Γ_{CF_3} is introduced to the model, a better prediction of the absolute density results, which is probably due to the reaction $\text{CF}_2 + \text{CF}_3 \xrightarrow{\text{M}} \text{C}_2\text{F}_5$ ($8.9 \times 10^{-13} \text{ cm}^3\text{s}^{-1}$).

4.2.3.2 Additional reaction channels

In [4], the biradical reaction $\text{CF} + \text{CF}_3$ is mentioned as a source channel of CF_2 ($k = 1 \times 10^{-11} - 1 \times 10^{-10} \text{ cm}^3\text{s}^{-1}$) and as a loss channel for CF and CF_3 . This symproportionation reaction⁴ is not yet considered in the NIST

⁴By this type of redox reaction, two different reactants with different oxidation numbers end up having the same oxidation number.

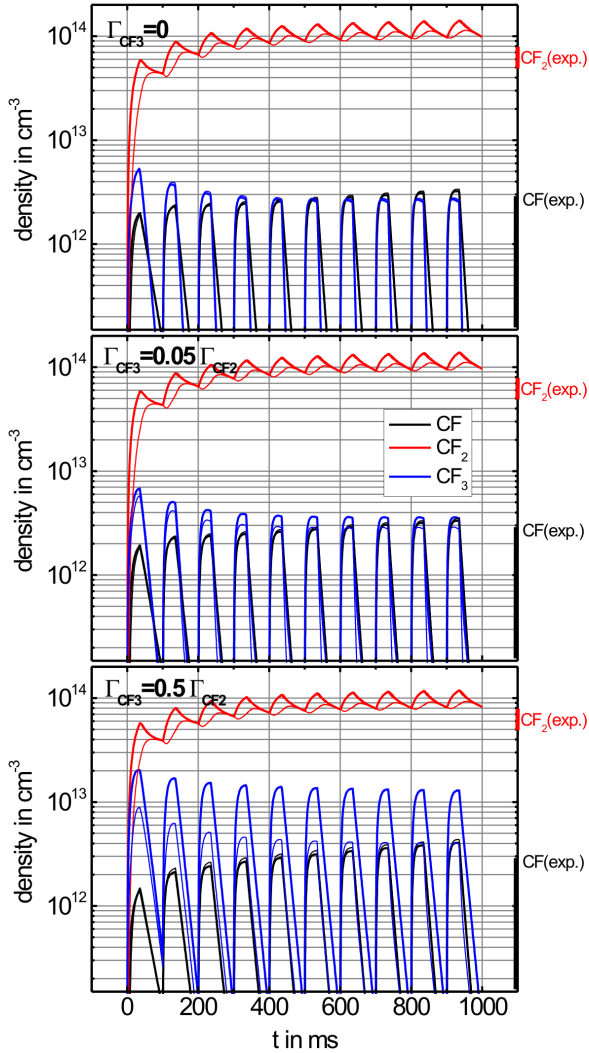


Figure 4.26: Variation of surface fluxes in the numerical model ($T = 100$ ms, $d_c = 35\%$, $P = 20$ W). Influence of Γ_{CF_3} on the radical and metastable densities. Black line: CF; red: CF_2 ; blue: CF_3 . Thick line: Density at the electrodes, thin line: density in the center of the reactor. Model with fixed flux Γ_{CF_2} from experiment. Other graphs: $\Gamma_{CF_3} = 0.05, 0.5 \times \Gamma_{CF_2}$.

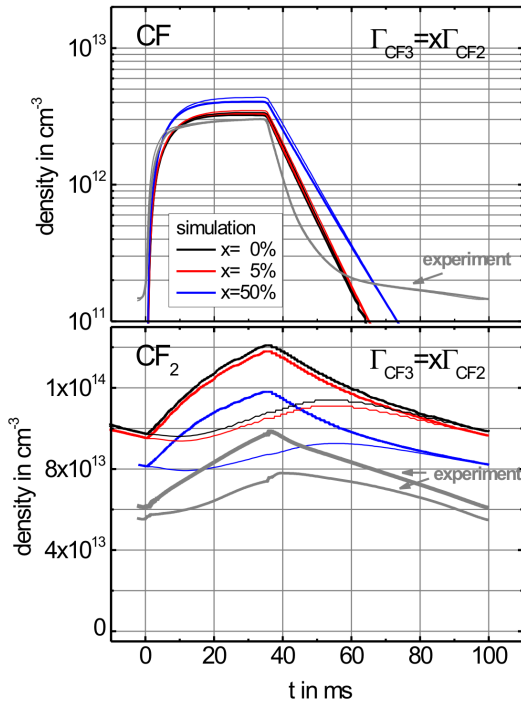


Figure 4.27: Comparison of experimental densities to model for $\Gamma_{CF_3} = x \times \Gamma_{CF_2}$. Top: CF, bottom: CF₂.

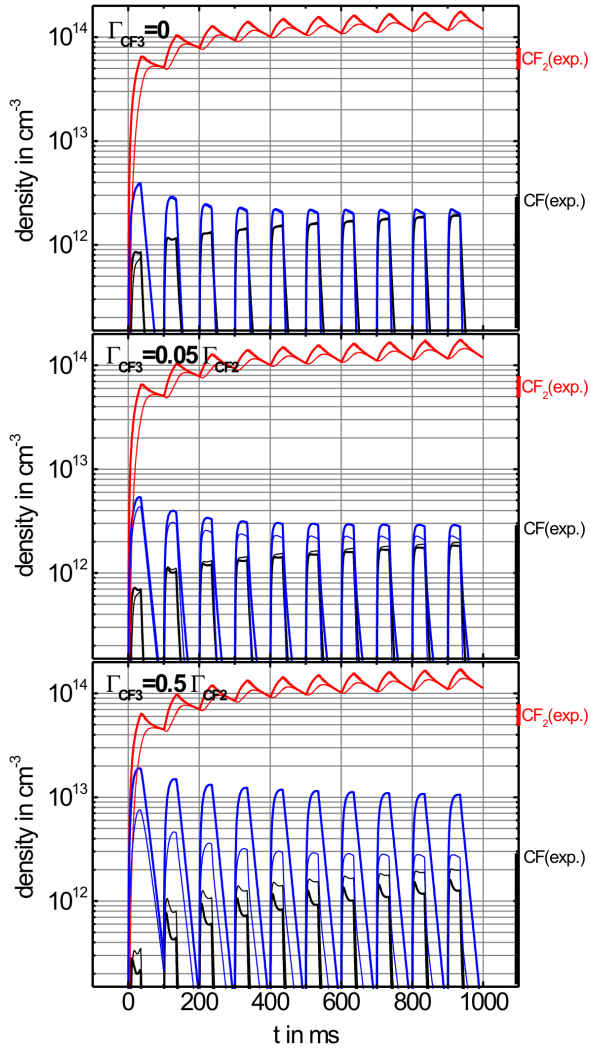


Figure 4.28: Numerical models for $\Gamma_{\text{CF}_3} = 0, 0.05, 0.5 \times \Gamma_{\text{CF}_2}$ with consideration of additional $\text{CF} + \text{CF}_3$ -recombination. Black: CF ; red: CF_2 ; blue: CF_3 . Thick line: Density at the electrodes, thin line: center density. Standard plasma conditions.

database or, up to the authors knowledge, documented in other publications upon fluorocarbon chemistry. Tentatively introducing this reaction with $k = 5 \times 10^{-11} \text{ cm}^3 \text{ s}^{-1}$ into the Comsol simulation changes the results. Compared to Figure 4.26, Figure 4.28 shows lower densities of CF and CF₃, whereas the CF₂ density is higher.

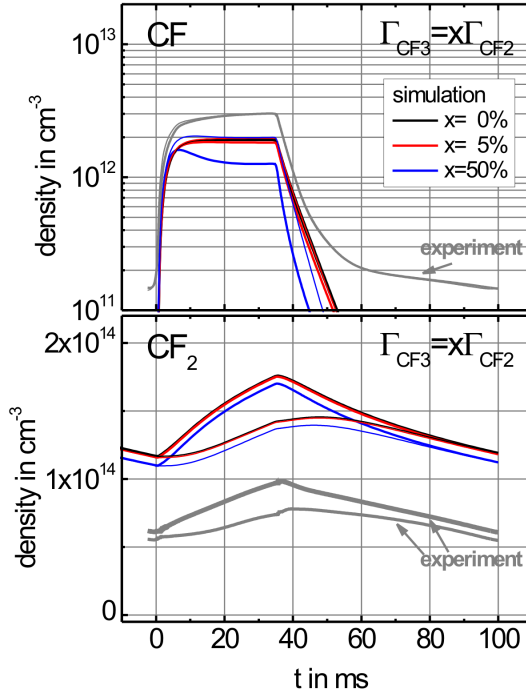


Figure 4.29: Comparison of measured densities with modeling results for $\Gamma_{\text{CF}_3} = 0, 0.05, 0.5 \times \Gamma_{\text{CF}_2}$. Top: CF, bottom: CF₂. Standard plasma conditions.

Especially the time dependence of CF shows significant changes in form of a non-constant concentration or even concentration drop after the initial increase at the beginning of a plasma pulse. The afterglow decay occurs much faster and results in better agreement between experimental and simulated data in Figure 4.29 than in Figure 4.27. But, on the other hand, the CF density shows a strong disagreement in the saturation behavior. The CF₂ density is too high, independent of Γ_{CF_3} . Furthermore, although this reaction was made responsible for the short afterglow increase in the mea-

sured CF_2 density in [4], this effect is hardly visible in the modeled data in Figure 4.29, bottom - probably, the increase relative to the density in the afterglow is too low. Finally, concerning the densities of CF and CF_2 , varying Γ_{CF_3} hardly affects the simulation results as can be seen in both graphs. In general, further tuning of the reaction rate coefficient could result in additional improvement of the model, but such changes would be of completely speculative nature. *Because it could not be experimentally validated in this work, the flux Γ_{CF_3} is not included in the following models.*

4.2.4 Discussion of single-carbon kinetics in the gas phase

4.2.4.1 The kinetics of the CF radical

For several species, the glow- and afterglow reaction channels involving CF as educt or product were evaluated. The total process rates of CF are depicted in Figure 4.30. It can be clearly seen that the major production of CF occurs via hydrogen-atom induced abstraction of fluorine from CF_2 . This is also pointed out by Ryan and Plumb [116] and further shown in the chemical discharge model by Voloshin *et al.* [80]. The loss of CF in the afterglow was found to be insufficiently described by the reactions in the Tables 3.4-3.8. By introducing the reaction $\text{CF} + \text{CF}_3 \rightarrow 2\text{CF}_2$ to the system as suggested by Francis *et al.* [117] and further supported by Booth *et al.* [4], the model shows better agreement, especially in the afterglow decay. Such, the overall losses were found to be mostly due to reactions with F and CF_3 , resulting both in the formation of CF_2 . The loss reactions stabilize the concentration of CF during the glow; the predominant reactions occur with CF_2 and CF_3 . In addition, the production and loss rates are nearly equal within the whole discharge volume. This is in agreement with the experimentally observed high uniformity of the density within the reactor.

Finally, the LLIF data showed a high production at the beginning of a plasma pulse. The total net rates as obtained from the experiments and the chemical discharge simulation are depicted in Figure 4.31. It is seen that simulations and experimental results show good agreement.

4.2.4.2 The kinetics of difluorocarbene

The production and loss rates of CF_2 are depicted in Figure 4.32. The production of CF_2 occurs isotropically in the discharge volume (top graph).

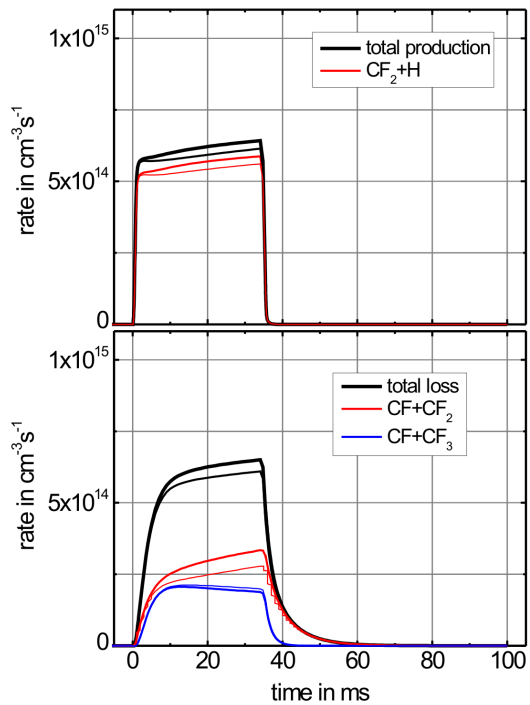


Figure 4.30: Modeling of the CF production and loss rate. Thick lines: at the electrodes; thin lines: in the discharge center.

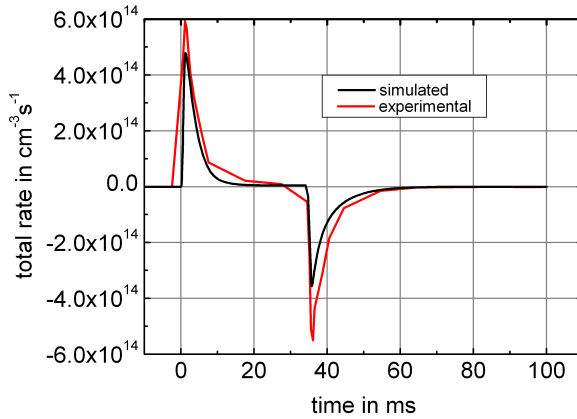


Figure 4.31: Total reaction rate from experiment and simulation. The high-rate initial increase is due to hydrogen-induced abstraction of F from CF_2 . Experimental and simulation parameters: standard conditions.

Here, only chemical reactions are considered, Γ_{CF_2} does not contribute to the production rates. During the glow, in the gas phase, CF_2 is produced e.g. by the combination of $\text{CF} + \text{CF}_3$ and by H-atom induced abstraction of fluorine from CF_3 (Figure 4.32). Contrary to that, the loss processes (labeled with the reaction products in the bottom graph) are anisotropic in space. This is due to the spatial density profile of CF_2 arising from Γ_{CF_2} . In the gas phase, dimerization and reactions with CF and CF_3 oppose the CF_2 flux from the walls. The first reaction results in the formation of the comparably inert molecule C_2F_4 , both latter reactions in the formation of C_2F_3 and C_2F_5 , respectively. These two molecules are important precursors for the formation of larger molecules. Per second, according to simulations in a pulsed discharge at 20 Watt, $2 - 3 \times 10^{14}$ molecules per ccm and second are produced (see Figure 4.32).

Looking at the spatial distribution of the net rates during the plasma glow, production and loss processes are nearly equal in the reactor center, whereas losses exceed the gas phase production close to the electrodes (Figure 4.33). When the net rate is compared to the feed of CF_2 molecules by Γ_{CF_2} , it is anyway almost negligible. This is important to notice because such way, the wall production of CF_2 is solely responsible for the devel-

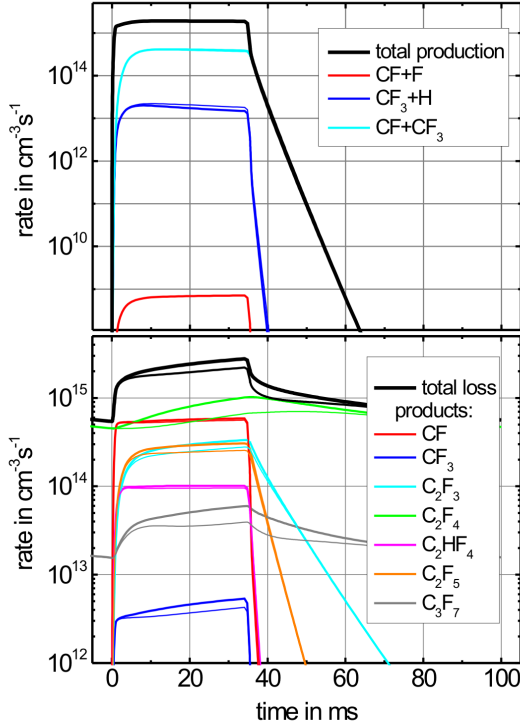


Figure 4.32: Upper line: major CF_2 production rates in the gas phase. Bottom line: major CF_2 loss rates in the gas phase. Thick lines: at the electrodes; thin lines: in the discharge center.

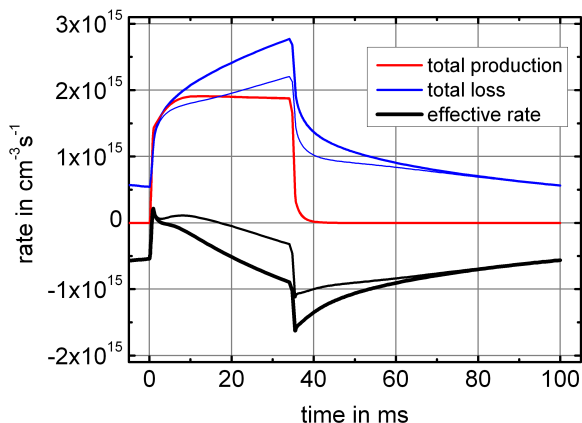


Figure 4.33: Total production and loss rates of CF_2 . Thick lines: at the electrodes; thin lines: in the discharge center.

opment of a profile by diffusion, which was the basic presumption of the diffusion model in Section 4.2.2.1. Details about the potential reasons for the difluorocarbene production at the electrodes are given in Section 4.2.6.

The models based on the rate coefficients in Tables 3.4-3.8 were found to describe the CF_2 density with sufficient precision. This finding is somewhat contrary to the results of Voloshin *et al.*, who suggested the dimerization rate coefficient of CF_2 (channel 43 in Table 3.6) to be too low by a factor of 30 [80]. Here, it was found that the commonly used rate coefficient is correct. Much more, it is suggested that the differences in Voloshin's work result from not including e.g. several oligomerization reactions like channels 38-41 and 45-49. In addition, the time-dependent surface flux of CF_2 was not considered in their work as well.

4.2.4.3 Other radicals

CHF can be measured by LIF according to literature [118, 119]. However, a complete wavelength scan of the available laser emission range⁵ with integral detection by the ICCD did not reveal any other species than CF and CF_2 . CF_3 is a highly abundant product from electron-induced dissociation of

⁵The available emission wavelengths with the current setup are between 210-355 nm and 420-2300 nm.

CHF₃. The rate of this process is somewhat larger than the one resulting in CHF₂ formation. Although CF₃ has well been detected by IR absorption, it was not possible to determine the absolute density [120–122]. CHF₂ can be measured by IR absorption [123] but, to the authors' knowledge, no data were published for trifluoromethane plasmas.

4.2.5 Summary of radical kinetics

The simulated chemical kinetics in the discharge show to strongly depend on the surface flux of CF₂.

- Without surface fluxes, the simulated densities of CF and CF₂ are $3 \times 10^{12} \text{ cm}^{-3}$ and $1 \times 10^{13} \text{ cm}^{-3}$ during the plasma glow according to simulations. In this model, the whole reactions are initiated by electron collision induced dissociation of CHF₃ as only initial source. The densities with the densities in [80] under similar simulation conditions with $2 \times 10^{12} \text{ cm}^{-3}$ and $1 \times 10^{13} \text{ cm}^{-3}$, respectively. The simulation methods in the present study and in the literature were different. Here, a two-term Boltzmann fluid approach was applied, whereas in [80], Monte-Carlo simulations were performed. Moreover, the gas composition was different due to addition of inert gas in this work. However, the partial pressures of CHF₃ were about the same (11.4 Pa and 10 Pa, respectively), which explains the similar results. In addition, from a physical point of view, the results support the statements on equality of the two-term Boltzmann to MC approaches in the examined pressure and excitation regime which is found in the literature [94].
- The experimental data resulting from the LLIF measurements showed that the CF₂ densities are about one order of magnitude higher. In addition, the experimentally observed anisotropy of the CF₂ density profile can only be reproduced in the simulation by inclusion of CF₂ fluxes from the surface as an additional source of reactants. By introducing the experimentally determined surface fluxes Γ_{CF_2} to the chemical model, the experimental densities were reproduced more accurately (see Figure 4.26). Persistent errors result from the surface flux determination, from the reaction rate coefficients, and finally from incomplete chemical reaction data. Additional surface fluxes of other reactive species could be present, but it was found to be too speculative to include them.

4.2.6 Discussion of single-carbon production on the surface during glow and afterglow

4.2.6.1 Wall production of CF

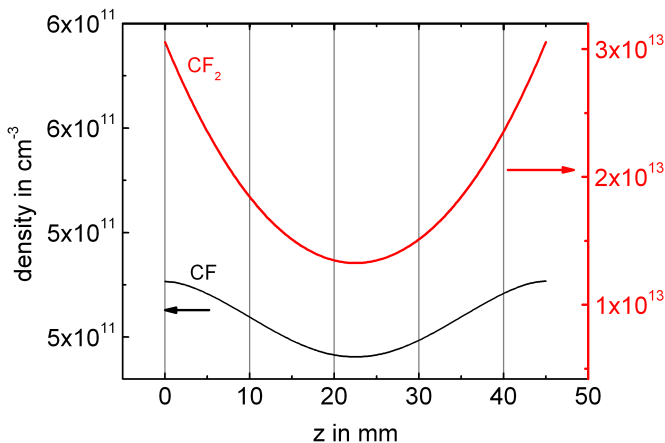


Figure 4.34: CF and CF₂ densities in a chemical simulation during glow in a pulsed discharge (beginning of pulse sequence). Notice that only CF₂ is produced at the walls, and the effect on the CF density profile.

In the literature, CF production at the electrodes is occasionally observed [4, 23, 124–126]. In the present work, no concave density profiles and therefore, no indications for such processes were found. Furthermore, especially in hydrogen containing plasmas, care must be taken whether concave CF density profiles are not induced by the CF₂ profiles in combination with high-rate H-atom induced abstraction of fluorine (reaction channel 96 in Table 3.8). This can be generalized to cases where CF₂ densities are orders of magnitude larger than the CF density, as also other processes result in fluorine abstraction. In Figure 4.34, a simulated diffusion-flow profile of CF₂ is shown together with the resulting CF profile. Only slight, but significant differences are observed at the electrodes ($z = 0, 45$), where the pseudo-diffusion profile of CF shows a typical flattening. Such deviations are easily overlooked when conventional cross-beam LIF techniques are applied. Often, the height-resolution is poor or acquisition times are too long such

that heating of the electrodes and other time-dependent effects cause large scattering and prevent to identify the curvature of the density distributions.

4.2.6.2 Production of CF_2 at the surface

The CF_2 densities show a height distribution dominated by diffusion fluxes from the electrodes towards the reactor center. The diffusion fluxes depend on the plasma conditions as there are power, duty cycle, pressure, gas flows, and the chemical state and polymer coverage of the walls as shown before in Section 4.2.2.2.

The phenomenon of CF_2 surface fluxes is under discussion for a long time. It was observed under many different experimental conditions (different monomer gases, plasma excitation, wall materials, and others, see Table 4.3). Profiles in these different plasmas were acquired by LIF.

- Γ_{CF_2} is sometimes accompanied by significant volume losses which were e.g. attributed to ionization [126] and oligomerization [50].
- Production at the electrodes can result from ion neutralization, ion sputtering, electron-induced fragmentation [36] as well as dissociation of oligomer [127] or other chemical reactions [126, 128].
- Additional to that, an electron-collision induced transition from singlet $^1\text{A}^1\text{CF}_2$ to triplet $^3\text{B}^1\text{CF}_2$ was suggested by Booth and Corr [129]. Accordingly, the singlet-triplet transition would reduce the center $^1\text{A}^1\text{CF}_2$ density, followed by a triplet-singlet transition at the electrodes and thus, reappearance of the singlet at the electrodes. Such, a concave profile would result.
- Temperature gradients can generally affect density profiles of CF and CF_2 [4, 130].
- The possibility of plasma-sheath processes by e.g. ion-neutral collisions was pointed out in [115, 131].

The monomer used also has a large effect, and a major criterion for a Γ_{CF_2} abundance is the fluorine-to-carbon ratio [29, 125, 132]. It is found that under fluorine-rich conditions like in CF_4 plasmas, ionic processes are presumably leading to CF_2 formation as neutralized fragments. For the further kinetics it must be noticed that in these plasmas, no film is deposited. Such, in the afterglow, molecules are observed to stick to the surface, which results in an opposed diffusion.

Table 4.3: CF₂ wall production in the literature

source	gas	geom.	wall	density profile	power supply
[126]	CF ₄	tube	quartz	concave, radial	rf, hw, p/cw
[23]	C ₄ F ₈	tube	quartz	concave, radial*	rf, hw, p
[50] (a)	CF ₄	pp	Al	> at powered el.	rf, ccp, p
[50] (b)	C ₂ F ₆	pp	Al	concave, axial	rf, ccp, p
[29]	CF ₄	pp	Al	> at powered el.	rf, RIE, p
[125]	CF ₄ + H ₂	tube	quartz	concave, radial	rf, ccp, cw
[127]	CHF ₃ + Ar	pp	Si	concave, axial	rf, icp, cw

p: pulsed excitation, cw: continuous wave excitation, *:afterglow

Contrary to that, at a lower fluorine-to-carbon ratio, CF₂ densities are larger (see comparative studies on CF₄ and C₄F₈ in [132]), which results from a strong wall production. A cyclic model of oligomerization, neutral or ion deposition, and subsequent (chemical) formation and desorption of CF₂ was suggested.

The influence of the fluorine-to-carbon ratio on the surface fluxes in a CF₄ + H₂ plasma was examined by Sasaki *et al.* [125]. Γ_{CF_2} turned from negative values ($-0.5 \times 10^{15} \text{ cm}^{-2}\text{s}^{-1}$) in pure CF₄ to $4.5 \times 10^{15} \text{ cm}^{-2}\text{s}^{-1}$ at 50% hydrogen, and same time, the CF₂ density increased by a factor of about 20. Especially the almost linear relation between the CF₂ density and Γ_{CF_2} supports the previously mentioned model of cyclic oligomerization, deposition, and CF₂ desorption in [132].

4.2.6.3 Surface production processes under the examined conditions

During the experiments performed, no wall production of CF was observed. Concerning CF₂, several of the above mentioned mechanisms can be excluded:

- Volume losses are not responsible as shown by evaluation of the net rate in Section 4.2.4.2.
- Neutralization of CF_x ions at the electrodes can be discarded as ion current densities are too low by two orders of magnitude (Figure 4.35) and, due to the gas mixture, consist of about 80-93% argon ions.

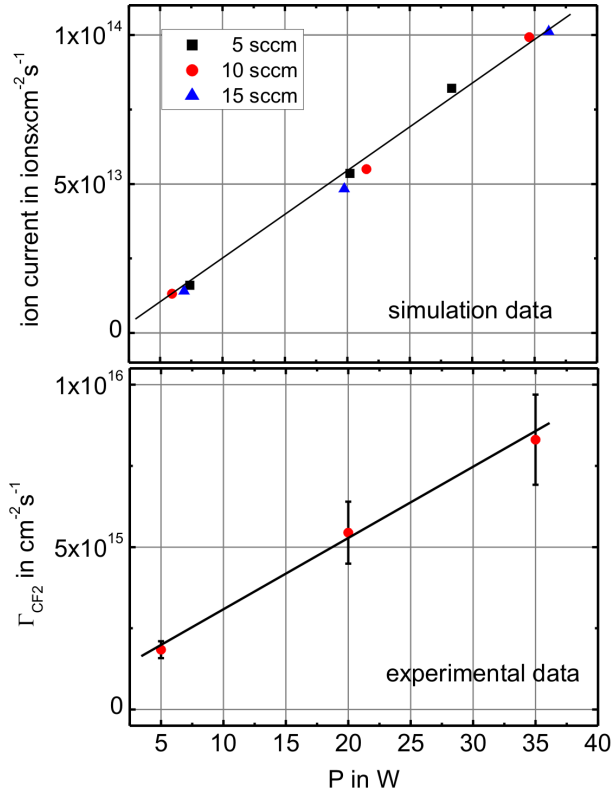


Figure 4.35: Ion currents (top) and Γ_{CF_2} (bottom) versus plasma power.

- Concerning singlet-triplet transitions, it is known from literature that triplet-triplet annihilation is taking place in the gas phase as well [133]. At pressures as used in the experiments, the annihilation should be well pronounced in the gas phase. In addition, the emission from the spin-triplet $^3\text{CF}_2$ at 540.5, 560.6 and 582.3 nm [134] was not visible in OES. The conversion of $^1\text{CF}_2$ to $^3\text{CF}_2$ is therefore unlikely to occur at rates high enough to explain the observed profiles.
- Temperature gradients can be excluded as well as absorption spectra showed that the rotational and vibrational temperatures are around room temperature.
- The same holds for ion-neutral processes in the sheath, because the ion-neutral cross sections commonly decrease upon increasing energy, and such, ion-neutral reaction rates would be higher in the plasma bulk than in the sheath region [29].

Instead, the dependence of the CF_2 density on the surface condition (Figure 4.24) shows increase and saturation when a homogeneous, closed film is obtained (see Section 4.4.1). This is in agreement with the model in [132]. Such, the kinetics of the wall production could be (a) sputtering by ions and/or electron-induced detachment, or (b) chemical reactions.

To (a): The ion current densities as obtained from the discharge simulation in Section 3.2 are depicted in Figure 4.35. A comparison to Γ_{CF_2} shows that the ion current densities are by two orders of magnitude lower than Γ_{CF_2} . Therefore, to obtain the surface flux, a sputtering yield of 100 molecules per incident ion would be at least necessary. This yield is too large compared to known sputtering yields at these ion energies. However, the energy input by impinging ions or electrons may be import to initiate chemical reactions.

To (b): Chemical reactions are consequently the major production source of difluorocarbene. The reaction kinetics, especially at the ignition stage, strongly depend on the plasma power and the duty cycle (Section 3.3). This is seen from the dependence of oligomer formation in the gas phase on the plasma conditions (Section 4.3):

- Upon increasing the plasma power, more oligomer is formed.
- Upon increasing the duty cycle, more oligomer is formed.

This both affects the maximum in the diffusion flux, Γ_{CF_2} . The faster increase observed at higher duty cycle could then be attributed to more

residual oligomers in the gas phase after a shorter pause (due to less pump-out). In this case, oligomer would be faster available for reactions on the surface, or even still be physisorbed to the surface. During the plasma glow, reactions leading to cross linking of the films are initiated. These reactions depend on energy supply by the plasma. Indeed, formation of such active sites inside polymers, resulting from plasma treatments or irradiation has been probed by ESR in [135, 136] and [137], respectively. This leads to restructuring of the material.

Electromagnetic radiation (emission of excited atoms or molecules) has not been taken into consideration so far. In the literature, the possible effect of radiation on polymerization and/or decomposition of polymer in fluorocarbon plasmas has yet not been mentioned, although it is well known that CF_2 can be e.g. obtained from flash-photolysis of several molecular substances [21, 138–140], amongst them several pure fluorocarbons [17, 21, 48, 141]. Bond breaks and excitations can be induced in polymers as well. The electronic states of PTFE for example reveal several possibilities for excitations of C – C and C – F bonds, mostly in the vacuum-UV region [142]. These processes can be used for surface processing. Such way, polishing by electronic excitation via F_2 -laser irradiation was recently published [143]. A significant weight-loss of 1-2 mg was found after irradiation of a PTFE substrate. In this example, the loss of mass would correspond to about 3.3×10^{18} CF_2 molecules cm^{-2} , the total energy input to 1.6×10^{19} photons ($\lambda = 157$ nm). Both numbers are comparable, showing the high efficiency of this process. The ejection of molecules from a PTFE surface would consequently require a similar number of radiative events in the plasma bulk. Depending on the emitting atom/molecule, the delay compared to a plasma pulse start could result from formation and excitation processes of the emitter, furthermore on the availability of oligomer as well as the reaction velocity within the film. The production of CF_2 in the afterglow is mainly attributed to persistent reactions inside the polymer, but also the post-discharge emission due to metastables could have an influence.

Concluding, strong indications are found that CF_2 is mainly chemically formed in the layer by reactions which are promoted by energy supply from the plasma. However, besides the proposed photonic model, no detailed chemical research on this topic was carried out yet, and it is not clear from chemical point of view, what kind of process can result in carbene formation

at such high rates. Candidates could be processes like cheletropic reactions⁶ which result in ejection of CF_2 from ionized molecules [144]. But these details require future investigations, otherwise, statements and conclusions on this special topic will remain speculative.

4.3 Gas phase kinetics and oligomer formation

4.3.1 Oligomer production probed by QMS

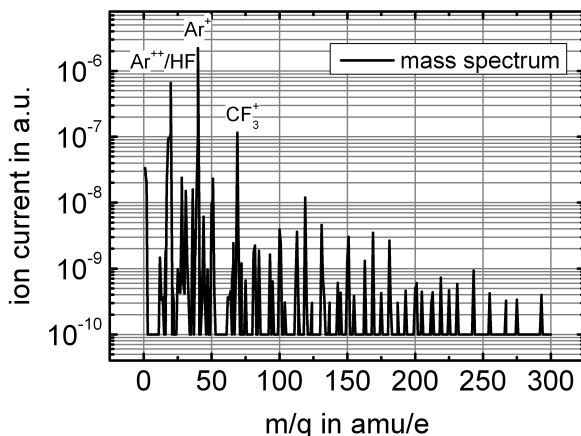


Figure 4.36: Example mass spectrum of a cw discharge at 8 W.

Mass spectrometry was carried out in pulsed and in cw discharges. A mass spectrum at 8 W in the setup used for mass spectrometry is shown exemplary in Figure 4.36. The reactor used was also a symmetric parallel-plate system, but had a smaller diameter (20 cm) than the one used for LIF measurements (29.8 cm). It is known from the literature that a scaling between different setups of same geometry is possible as long as the Yasuda factor W/FM is kept constant [145]⁷. Here, the scaling factor between both setups is 2.5. The pressure is kept constant, whereas power and gas flows

⁶Cheletropic reaction is a conversion reaction of a π bond into a lone pair of electrons and a pair of σ bonds.

⁷This is an empirical formula and is valid only in case of e.g. constant electron-energy distribution functions and invariant plasma mode.

are downscaled. Such, the residence time as well as the energy uptake per molecule are kept constant. In the following text and graphs, the power of the small setup was converted to the corresponding power of the LIF setup for better comparison. The original power applied to the reactor attached to the mass spectrometer thus can be obtained by division with 2.5.

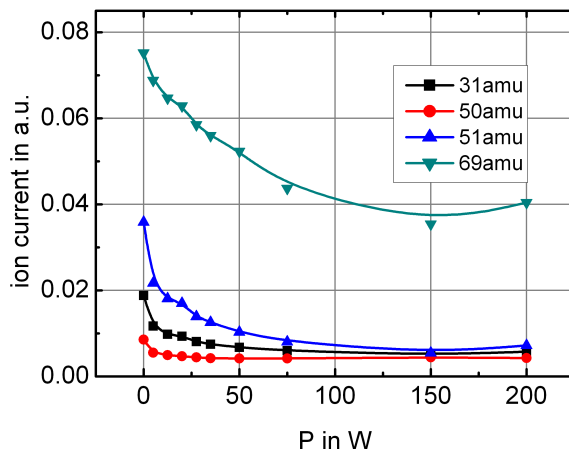


Figure 4.37: Low-mass fragments detected by the QMS versus plasma power. The initial points at 0 W correspond to the fragmentation pattern of CHF_3 in the setup with the ionizer settings used.

Figure 4.37 shows the dependence of small mass fragments on the plasma power. Increasing the plasma power leads to a decreasing signal of low mass fragments, which can either originate from feed gas CHF_3 or species formed in the plasma. For the interpretation of masses see Table 4.4. The data points at 0 Watt correspond to the fragmentation of CHF_3 . Low mass signals measured during discharges can also arise from fragments of oligomers. It is found that all single-carbon (C_1) signals decrease with increasing plasma power which is due to the formation of oligomer species with C_n backbones.

In the following sections, the fragments will be categorized by their carbon backbone C_n , n being the number of carbon atoms *per charge*.

Table 4.4: Mass fragments and suggested composition

amu/e	n	position	singly charged ion
31	1	chain	CF^+
32	1	chain	CHF^+
50	1	end	CF_2^+
51	1	end	CHF_2^+
69	1	end	CF_3^+
82	2	chain	CF_2CHF^+
100	2	chain	$(\text{CF}_2)_2^+$
101	2	end	$\text{CF}_2\text{CHF}_2^+$
119	2	end	CF_2CF_3^+
132	3	chain	$(\text{CF}_2)_2\text{CHF}^+$
150	3	chain	$(\text{CF}_2)_3^+$
151	3	end	$(\text{CF}_2)_2\text{CHF}_2^+$
169	3	end	$(\text{CF}_2)_2\text{CF}_3^+$
182	4	chain	$(\text{CF}_2)_3\text{CHF}^+$
200	4	chain	$(\text{CF}_2)_4^+$
201	4	end	$(\text{CF}_2)_3\text{CHF}_2^+$
219	4	end	$(\text{CF}_2)_3\text{CF}_3^+$
251	5	end	$(\text{CF}_2)_4\text{CHF}_2^+$
269	5	end	$(\text{CF}_2)_4\text{CF}_3^+$

4.3.1.1 Single-carbon molecules

In general, the most abundant ions in the mass spectra (see Figure 4.36) were those with $m/q < 70$ amu/e, 70 amu corresponding to the mass of CHF_3 . Here, 69 amu/e had the highest intensity, followed by 51, 31, and 50 amu/e. Amongst some fractions of double-charged ions, these signals arise from fragmentation of the precursor as well as of oligomer species.

4.3.1.2 Macromolecules

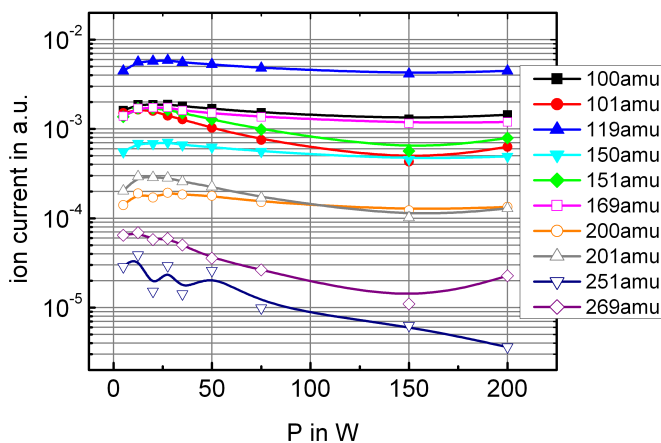


Figure 4.38: Some oligomer fragments detected by the QMS versus plasma power. Notice the first initial increase in all signals, followed by different signal reductions when the plasma power is further enhanced. For the interpretation of masses, see Table 4.4.

The major macromolecular fragment detected was $m/q=119$ amu/e, originating from a pure fluorocarbon with C_2 backbone, followed by two other fluorocarbons with 100 amu/e (C_2 backbone) and 169 amu/e (C_3) for powers $P > 12.5$ W. Further, as a tendency, it is observed that the higher n , the lower the signal. This could be due to fragmentation within the mass spectrometer, resulting in destruction of long chains. But most likely, in accordance with the decrease in signal with increasing plasma power, losses due to polymerization may be important. This is further supported by the results of the polymer deposition as discussed in Section 4.4.

The formation of oligomer fragments ($m/q > 70$ amu/e) is shown in Figure 4.38. The fragments show an initial increase up to about 20 Watt. This is followed by a decrease in signal for all channels which may be attributed to oligomer loss by polymerization at the electrodes. Thereby, two types of decrease are observed, a fast one for 101, 151, 201, 251, and 269 amu/e, and a second one where the other signals decrease much slower. In the final state recorded at 200 Watt, several masses shown an increase again. As the plasma showed trends towards a hollow-cathode like glow towards the mass spectrometer aperture at this power, the signal increase may be attributed to enhanced polymer sputtering and release of heavy species and was therefore discarded.

4.3.1.3 Hydrogen and fluorine bond retention

The ratio $r_{FC/HFC}$ of pure fluorocarbon (FC) to hydrogen-containing fluorocarbon (hydrofluorocarbon, HFC) mass fragments with same C_n backbones is depicted for end- and chain groups⁸ in Figure 4.39. In these graphs, the spectra are normalized with respect to the ratios obtained at 5 Watt plasma power, which was the lowest power for a stable discharge. Hydrogen may be abstracted from molecules by atomic fluorine (see e.g. Section 1.3.2), such, the changes of the hydrogen content in oligomer fragments upon the variation of the plasma power indicate changes in the plasma chemistry.

The chain groups in Figure 4.39, top, show a strong increase in $r_{HFC/FC}$ upon the increase of the plasma power. For C_2 species (82 and 100 amu), a local minimum around 20 Watt is seen, followed by a linear power dependence above 25 Watt. For molecules with C_3 backbones (132 and 150 amu), the local minimum is less pronounced, but the overall trend is quite close to the one of C_2 species. Mass signals of C_4 species were close to the lower detection limit, and therefore, $r_{FC/HFC}$ data points are subjected to scattering. However, an increase is seen for the ratio of these fragments as well: The data depicted in Figure 4.39 shows an relative ratio of 150% at 150 W compared to 5 W. The end groups in Figure 4.39 show a strong increase in $r_{HFC/FC}$ upon the increase of the plasma power.

For end group C_1 species (51 and 69 amu in Figure 4.39), two linear regimes are seen. At 20 W, the slope sharply decreases, the reason is unclear. For end group molecules with C_2 backbones, a linear dependence on the plasma power is seen in the power range from 25 to 150 Watt. For molecules with C_3 backbones, linear behavior is seen above 37.5 Watt, with a lower

⁸assuming linear molecules

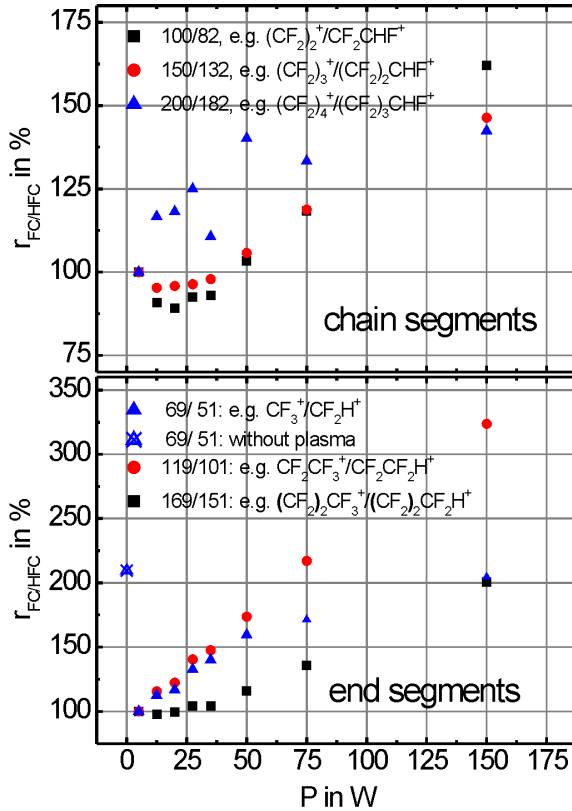


Figure 4.39: Ratio of some fluorocarbon to hydrofluorocarbon chain and end segments in dependence on the plasma power, normalized with respects to the ratio at 5 Watt.

slope than in the case of C_2 backbones. For C_1 and C_3 end fragments, $r_{FC/HFC}$ reaches 200 % at 150 W, for C_2 , 300 % were calculated.

The above examples show that less and less hydrogen is found within the ionic fragments detected by mass spectrometry if the plasma power is increased. We attribute these changes in the plasma chemistry to various parameters, but basically to the changes in the electron collision induced dissociation rates which are addressed in the modeling in Chapter 3.

4.3.2 Modeling of oligomer formation

The numerical analysis of cw and pulsed discharges reveals the influences of the primary dissociation channels as well as the wall production of CF_2 on the overall chemical composition. Also the mean electron energy dependence on the plasma power as depicted in Figure 3.13 and the resulting ratio $r_{FC/HFC}$ of fluorocarbon (FC) to hydrofluorocarbon (HFC) fragments from primary dissociation (Figure 3.18) may have an effect. Here, power, pressure, and gas flow variations are in the focus of interest.

4.3.2.1 Non-carbonic species in cw plasmas

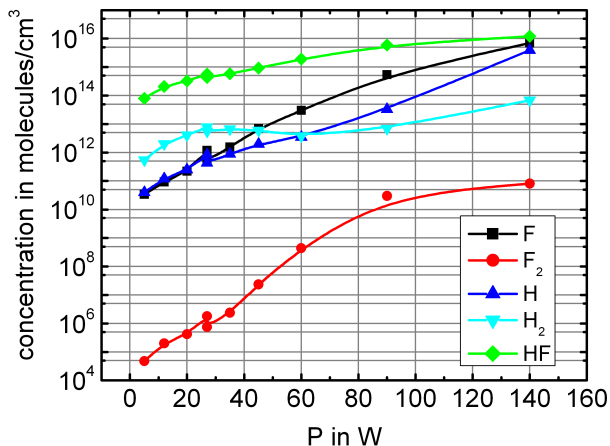


Figure 4.40: Formation of atomic fluorine, atomic hydrogen, F_2 , H_2 , and HF in discharges with variable power after 1 second of simulated time. $p = 80$ Pa, $F_{CHF_3} = 10$ sccm, $F_{Ar} = 60$ sccm.

As could be expected, HF appears as one of the most abundant molecules (Figure 4.40). It is found that the $C_xH_yF_z$ concentration is reduced by fluorine-induced hydrogen abstraction, resulting in the formation of HF according to the reactions in Table 3.8. Hydrogen, in addition, leads to fluorine abstraction and also to the formation of HF. In both cases, large amounts of hydrogen become bound to fluorine which leads to an overall reduction of carbon-hydrogen or carbon-fluorine bonds and consequently to an increase of free carbon bonds. Amongst all processes, the rate coefficient for diatomic combination is rather small. F_2 is hardly formed for this reason. H_2 is a product of several processes, and therefore, it is present at higher concentrations than F_2 .

4.3.2.2 Oligomer species in cw plasmas

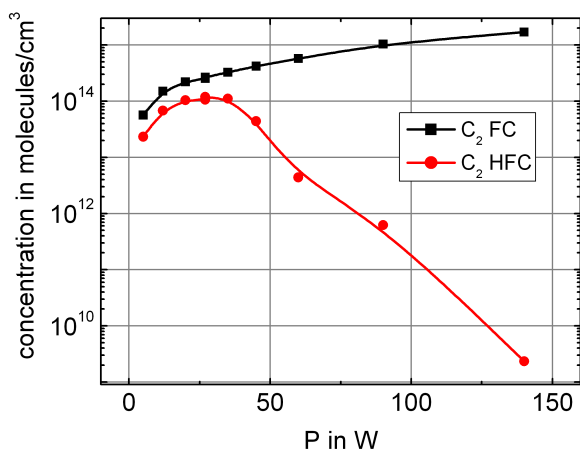


Figure 4.41: Formation of pure fluorocarbons and hydrofluorocarbons with a C_2 backbone. $p = 80$ Pa, $F_{CHF_3} = 10$ sccm, $F_{Ar} = 60$ sccm.

Figure 4.41 shows the results of C_2 -backbone molecules in a power-variation simulation. The formation of pure fluorocarbon species compared to hydrofluorocarbons is more and more favored when the plasma power is increased, which is partially due to the preferential dissociation of CHF_3 into $CF_3 + H$ according to Section 3.2.3. According to the enhanced formation of HF, the amounts of C_xF_z increase with increasing plasma power.

Therefore, more fluorocarbon oligomers are formed.

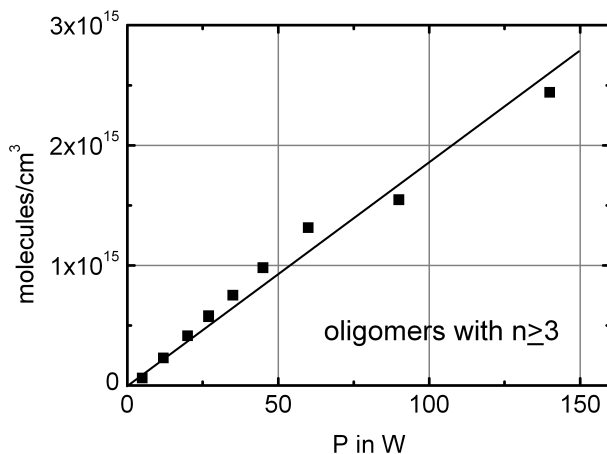


Figure 4.42: Formation of macromolecules with C_n backbone, $n \geq 3$.

Figure 4.42 shows the linear increase in macromolecule formation with plasma power. The products with $n \geq 3$ are important precursors for polymer deposition and thus, an increase in polymer deposition upon increasing the plasma power can be expected from the simulated plasma-chemical composition.

In addition to the power variation simulation series, the effect of the pressure on the formation of dimers and oligomers was investigated as well. According to Figure 3.13, the mean electron energy increases upon increasing pressure within a broad range of plasma powers. Consequently, increasing pressure is expected to result in higher partial pressures of hydrofluorocarbons according to the dissociation scheme in Figure 3.18. In fact, this results in the chemical simulation (conditions: $p = 60, 80, 100$ Pa, $F_{\text{CHF}_3} = 10$ sccm, $F_{\text{Ar}} = 60$ sccm) as depicted in Figure 4.43. Here, for C_2 backbone molecules, an enhancement in the partial pressure as well as the absolute pressure results in lower production of fluorocarbon species, whereas the hydrofluorocarbon production remains approximately constant. Under the examined conditions, the build-up of oligomer with $n \geq 3$ shows an increase with increasing partial pressure of trifluoromethane as well as with increasing absolute pressure, both obviously on the cost of C_2 molecules such as C_2F_4 .

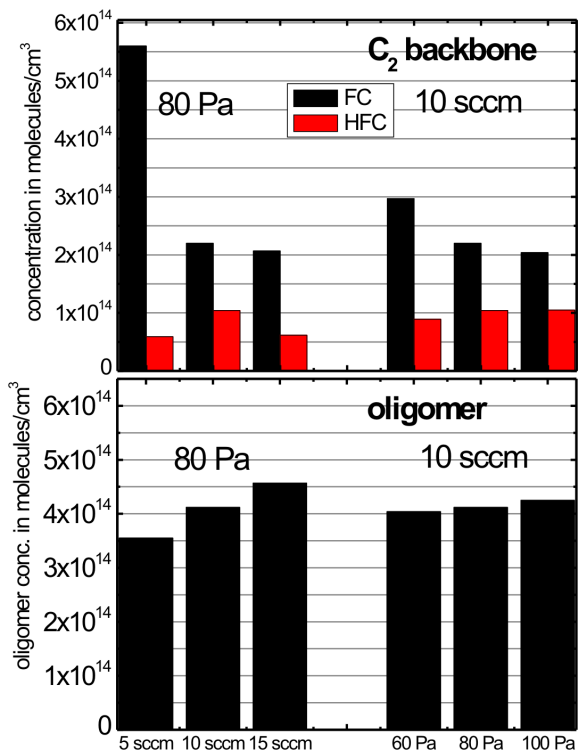


Figure 4.43: Formation of HFC and FC with C₂-backbone (top) and oligomer formation (bottom) under various conditions (constant: 20 W plasma power, 60 sccm argon).

4.3.2.3 Oligomer species in pulsed discharges

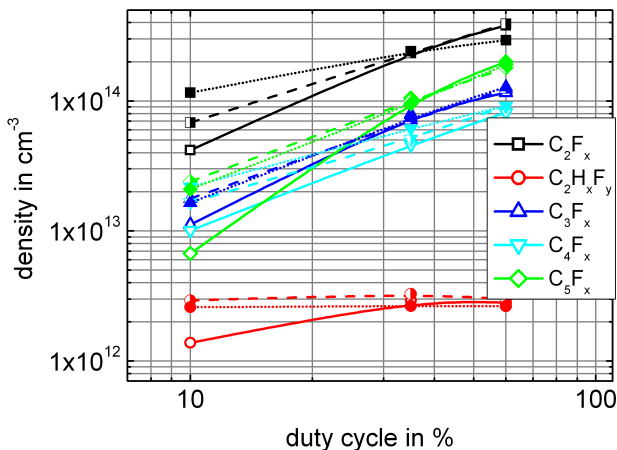


Figure 4.44: Comsol Multiphysics simulation of high-mass oligomer formation in a pulsed discharge at variable dc. Hollow symbols, solid line: $T = 100$ ms; half-filled symbols, dashed line: $T = 500$ ms; full symbols, dotted line: $T = 1000$ ms. Hydrofluorocarbon concentrations are insignificant.

As it turns out from the simulations, the densities of molecules with $n \geq 3$, monitored after 2 seconds of simulation time⁹, show mainly a dependence on the dc and less on the pulse periods (Figure 4.44). The concentration of $C_2H_xF_y$ as a representative of hydrofluorocarbons is very low compared to C_2F_x , which is due to the low net production rate. In general, a linear increase of the oligomer concentration with duty cycle is found.

4.3.3 Discussion of oligomer formation

Comparing the build-up of oligomer as monitored by quadrupole mass spectrometry (QMS) to the data obtained from simulations, the observed trends are similar: An increase in plasma power results in higher formation rates of large molecules at low plasma powers (Figures 4.38 and 4.42). However, above a power of about 20 W, an decrease in the overall QMS signals was observed (Section 4.3.1). This is not seen in the simulations in Section 4.3.2

⁹at this point, all simulations were in afterglow conditions

- the decrease is therefore attributed to losses by polymer deposition of the parent high-mass precursors.

Furthermore, with increasing power, the retention or formation of CH-bonds decreases, that means the ratio $r_{FC/HFC}$ of pure fluorocarbons to hydrofluorocarbons increases as shown for experimental and simulated data in Figures 4.39 and 4.41. This is accompanied by the formation of the stable molecules HF and H₂ (see Figure 4.40).

However, in the simulation of chemical kinetics, $r_{FC/HFC}$ increases much faster than observed experimentally. This is accompanied by the higher formation of HF in the simulation. The reason is probably a too large electron-collision induced dissociation rate coefficient of HF (channel 13 in Table 3.4), which affects many reaction channels in CHF₃ containing discharges [67]. The mechanism of HF formation can become avalanche-like: When the HF bond is broken, H· and F· radicals abstract fluorine or hydrogen at high rates. Such, from one broken molecule, two are abundant by chemical reactions [80]. Consequently, the HF increase becomes enhanced, and more fluorocarbon radicals without hydrogen-bonds result. A second reason is that pump-out of species was not considered in the simulation. This may largely affect the gas phase chemistry, as HF and H₂ hardly condensate at the surfaces and are, in reality, removed from the system by pumping. A third point may be that chemical kinetic data on hydrofluorocarbon reactions with C_{n≥3} backbones was not included.

But despite of these restrictions, the major trends of models and experiments agree quite well.

4.4 Gas phase reactions and polymer deposition

4.4.1 Polymer deposition and polymer properties

Under all plasma conditions which were examined by LIF and with additional variation of T in the microsecond to second range, the polymer deposited on silicon substrates exposed to the plasmas were examined. The thickness of the deposits was measured by spectroscopic ellipsometry, the surface tension resulted from contact-angle measurements, and finally, the chemical composition was investigated by XPS. Details on the measurements and the observed phenomena were published by the author in [146, 147].

4.4.1.1 Polymer thickness and density

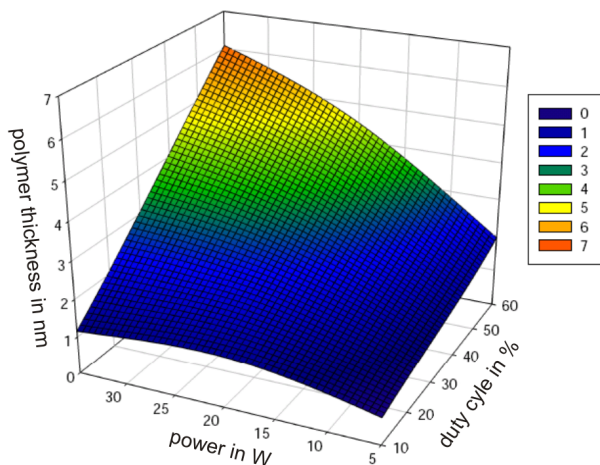


Figure 4.45: Dependence of the polymer thickness (after 60 seconds of deposition) on the plasma power and the duty cycle as measured by spectroscopic ellipsometry.

Figure 4.45 shows the dependence of the polymer thickness on the plasma power and on the duty cycle in case of pulsed discharges. This graph results from a DoE¹⁰ study and is only addressing the major dependencies. The data refer to a total treatment times of total 60 s. In pulsed discharges, the plasma-off times are herein included. The polymer thickness increases almost linearly with plasma power as well as with duty cycle. The dependence on the other parameters, namely the pulse period ($T = 10 \mu\text{s} - 1 \text{ s}$) as well as pressure (60-80 Pa) and CHF_3 flow (5-15 sccm) is statistically insignificant according to DoE.

The density of the films was measured on 6 inch wafers. One of the wafers was coated in a continuous wave (cw) plasma, the other one in a 10% duty cycle pulsed discharge. In both cases, the gas flows were 10 sccm CHF_3 and 60 sccm Ar, pressure and power were 80 Pa and 20 Watt, respectively. The effective plasma-on time was 1200 seconds in both cases. The gain in weight and the polymer thickness, determined from 30 ellipsometer measurements across the diameter of each wafer, were $3.58 \pm 0.03 \text{ mg}$ / $119.1 \pm 1.9 \text{ nm}$ and

¹⁰Design of Experiments, allowing to identify the most significant parameters of an experiment.

3.90 ± 0.03 mg/ 126.3 ± 1.3 nm for the cw plasma and the pulsed plasma, respectively. Apparently, the mass deposition as well as the thickness are both lower by about 10% in case of the cw discharge. The major reason may be the effect of higher substrate temperatures in a cw discharge, enhanced concentration of etching species in the cw plasma, or additional deposition of polymer in the off time of the pulsed discharge. The polymer density was the same within the error bars (1.75 ± 0.02 gcm⁻³).

4.4.1.2 Surface tension of polymer deposits

On the silicon substrates which were used here, the surface tension was reduced from about 50 mN/m (27 mN/m disperse surface tension, 23 mN/m polar surface tension) on the native substrates to values typical for fluorinated surfaces (disperse ≤ 20 mN/m, polar close to 0 mN/m). The polar contributions clearly indicate the transition to a closed film. This is shown in Figure 4.46. The surface tension in the closed-film regime, seen here as saturation, corresponds to a water contact angle of 120°, which is a typical value for fluorocarbon polymers and the highest one possible: It has been shown that a surface densely covered with CF₃ groups possesses the highest water contact angles amongst all planar solids, due to the lowest surface tension possible [148]. By measuring the contact angles, the presence of a contact angle hysteresis (difference between advancing and receding contact angle) indicates that the surface is either rough or chemically heterogeneous [149, 150]. Here, the progression upon increasing average thickness corresponds to a transition from non-covered to covered substrates¹¹. Expressed in simple terms, upon increasing the drop size, the liquids are repelled by the fluorocarbon groups, whereas upon decreasing the drop size, droplets stick to surface areas with higher surface tension. The hysteresis vanishes at an average thickness of 15-20 Å which therefore corresponds to the threshold value for the transition to a completely closed homogeneous film.

4.4.1.3 Film composition

As expected, XPS reveals that upon enhancing the duty cycle, i.e. increasing the polymer thickness, the surface elemental composition shows increasing amounts of fluorocarbon species due to deposition of polymer (exemplary shown in Figure 4.47). Same time, the element signals from the substrate (silicon Si2p and oxygen O1s) are attenuated. From the attenuation of the

¹¹The roughness is below some Angstroms and does not contribute to these differences.

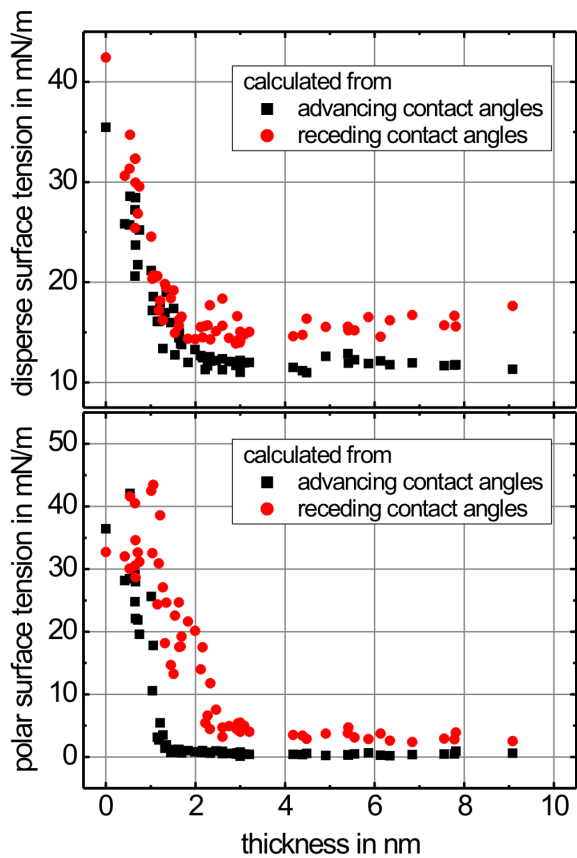


Figure 4.46: Plot of the disperse surface tension (top) and the polar surface versus the polymer thickness. For details, see text.

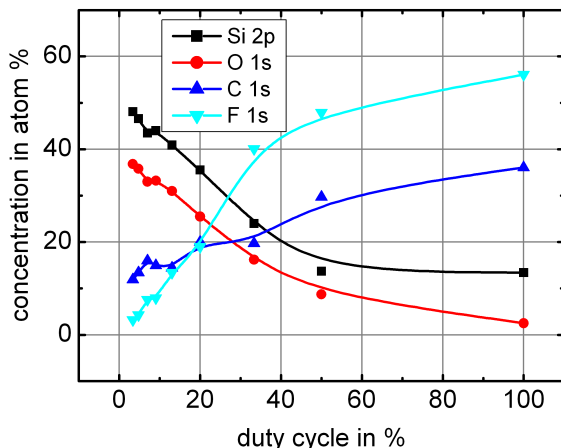


Figure 4.47: Surface elemental composition after treatment in a pulsed plasma in dependence on the duty-cycle. (20 Watt, 80 Pa, 10 sccm CHF_3 , 60 sccm Ar.)

substrate signal, the coating thicknesses can be determined [151–156]. The basic relation is given by a Lambert-Beer attenuation law, but here, the electron attenuation length (EAL) as absorption coefficient must be known. The EAL is basically a function of the kinetic energy of the photoelectrons (here being emitted from silicon and oxygen in the substrate) as well as on the overlayer scattering cross sections. These cross sections depend on the elemental composition of the polymer film. The corresponding data was derived from the NIST database [157]. To summarize the results of this step, the overlayer thicknesses were found to be close to the results from ellipsometry.

The overall chemical compositions results in almost pure fluorocarbon films with F/C ratio $r_{F/C}$ of 5/4, which is in the range of other polymers deposited from CHF_3 [158]. Compared to PTFE¹² ($r_{F/C} = 2/1$), the cross-linking of the plasma polymer, which is reflected in the aliphatic carbon component at 284.6 eV binding energy and the $\underline{\text{C}} - \text{CF}_x$ component at 286.2 eV, shifts the composition towards a lower $r_{F/C}$.

Detail spectra of the carbon core electron (C1s) spectra are shown in

¹²Polytetrafluorethylene (PTFE, $(\text{CF}_2)_n$) is a standard material to which fluorocarbon plasma polymers are often compared regarding their properties.

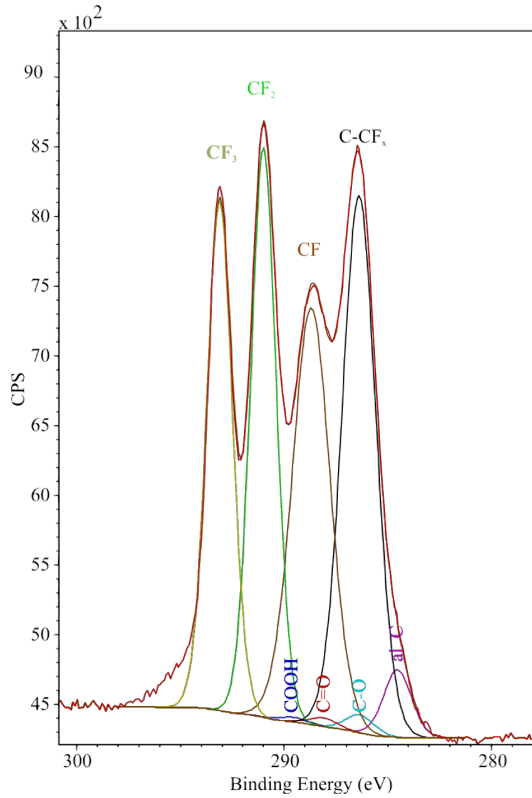


Figure 4.48: C1s detail spectra in dependence of the duty cycle. Deposition at 20 Watt, 80 Pa, 10 sccm CHF_3 , and 60 sccm Ar.

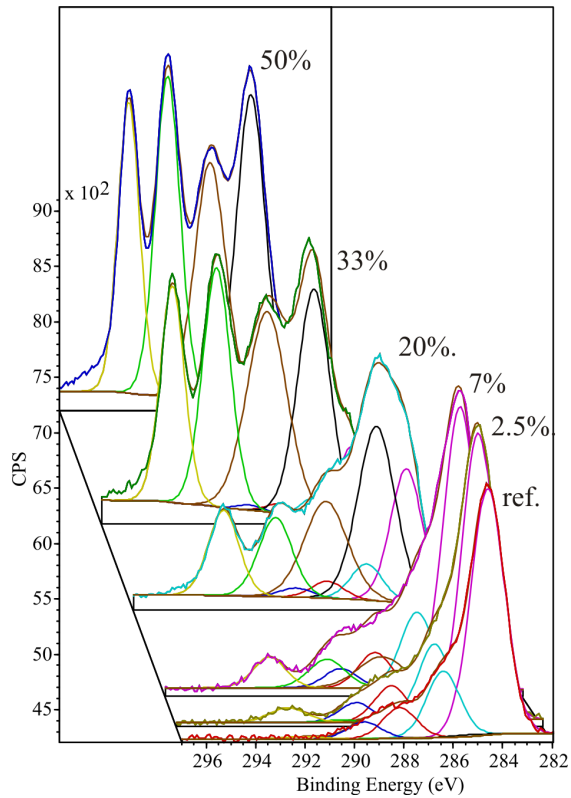


Figure 4.49: C1s detail spectra in dependence of the duty cycle. Deposition at 20 Watt, 80 Pa, 10 sccm CHF₃, and 60 sccm Ar.

Figure 4.49 in dependence of the duty cycle. On the untreated reference, aliphatic and oxidized carbon species are present as a contamination¹³. With increasing duty cycle, more and more fluorinated carbon species are deposited onto the surface. Same time, the signal of $\underline{C} - CF_x$ is throughout very pronounced which indicates a high crosslinking of the polymer. The C1s spectra further do not show any changes above 33% duty cycle and also the relative surface elemental composition of the polymer film remains invariant. Detailed analyses on the peak fittings including oxidized species were published by the author in [147, 159].

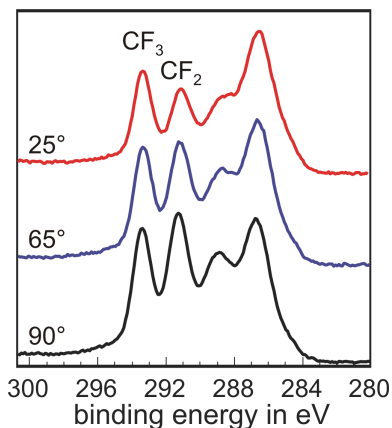


Figure 4.50: C1s detail spectra with angular resolution. The angles indicated are with respect to the film plane. Deposition at dc=50% (20 Watt, 80 Pa, 10 sccm CHF_3 , 60 sccm Ar.)

For the outer boundary layers, CF_3 groups are enriched at the surface: this is seen in the angle-resolved XPS (ARXPS) detail spectra of carbon C1s in Figure 4.50. This observation was confirmed with a TOF-SIMS analysis of von Gradowski, Jacoby, Hilgers, Barz, Wahl, and Kopnarski on such plasma-polymer coatings [160] and is in agreement with the low surface tension values observed at low coating thicknesses as stated above. Further, the effect of chain orientation on contact angles was e.g. studied by Beamson and Alexander [65] and showed highest values when fluorinated groups were directed outwards. The physical reason for enrichment of fluorinated groups on the surface (besides some preferences of group attachment during the

¹³Such contaminations arise from exposure to atmosphere. After cleaning, the surface is quickly recontaminated. The contamination signal corresponds to some atomic layers.

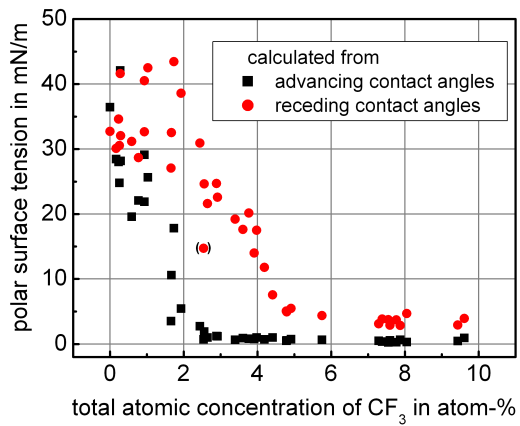
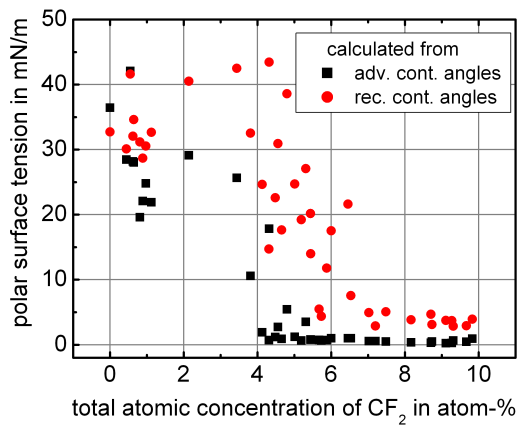


Figure 4.51: Here, the correlation between the amount of hydrophobic groups on the surface tension is shown. For details, see text.

deposition process) is generally reorientation of polymer chains in order to minimize the surface free energy [161].

This is illustrated in Figure 4.51, depicting the correlation between polar and disperse surface tension, and the amount of CF_2 and CF_3 groups on the surface. The good correlation between the measured CF_3 group density and the polar surface tension indicates that these groups are turned outward, whereas the worse correlation of the CF_2 groups to the polar surface tension indicates that the latter groups are not all accessible to the testing liquids.

4.4.1.4 Crosslinking effects: radical reactions

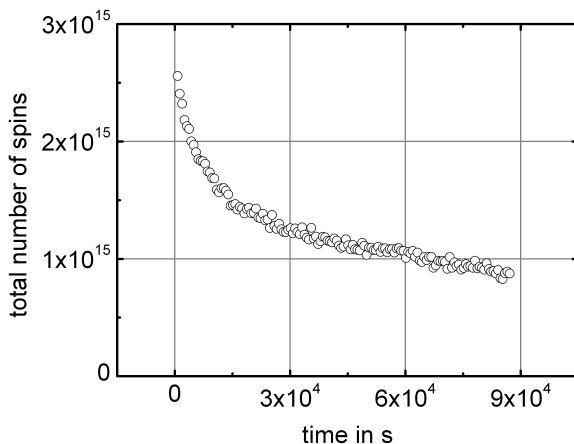


Figure 4.52: ESR data illustrating the dynamical processes in a coating from a CHF_3/Ar plasma.

The high XPS signals of crosslinked groups, which are present under all conditions, can be due to fluorine abstraction by gas-phase radicals, by radicalization due to electron or ion impact, or UV radiation. All these processes are well known to occur and to affect the structures of polymers being exposed to plasmas [162]. A tracing method for radical reactions inside and on the surface of the polymers is given by ESR [135–137]. Here, upon time, the radical density is either reduced due to recombination or disproportionation (=formation of double bonds) as depicted in Figure 4.52. Such processes within plasma polymer layers from a different precursor were

investigated e.g. by Haupt, Barz, and Oehr in [136].

4.4.2 Correlation between polymer deposition and oligomer formation

In this part, plasma-surface interactions concerning oligomer formation and polymer deposition are addressed. According to Section 1.3.3.4, several mass fluxes appear in the overall mass flux balance (Equations (1.37) and (1.38)).

1. Adsorbing particles:

- Small neutrals: Some authors observed sticking of radicals to the surface under fluorine-rich conditions (see Section 4.2.6). In the afterglow density measurements of CF and CF₂ in (non-depositing) CF₄ plasmas in [115], the molecules were found to stick to blank substrate surfaces. In contrast, fluorocarbon polymer coatings on the substrates completely prevented the molecules from sticking. Accordingly, sticking was not at all observed for CF and CF₂ in this work. More general, sticking deposition of small reactive species, though it may take place, can only lead to insignificant deposition fluxes. The excessive heat of reaction in case of a chemical reaction with the surface may result in immediate destruction of bonds, and such, chemisorption is unlikely to take place. More likely, three-body recombinations can take place at the electrodes after physisorption of small reactive species. The excessive reaction heat is then transformed to kinetic energy, which will result in desorption of the reaction products.
- Small ions: As species interacting with the surface, small positive ions could be considered. But as the ion currents of fluorocarbon species are in the range of $2-10 \times 10^{13} \text{ cm}^{-2} \text{ s}^{-1}$ (see Figure 4.35), they do not affect the balance.
- Neutral and ionic oligomers: Physisorption and chemisorption are both more likely to occur the larger the molecules are. It was concluded that in particular large species with low vapor pressure will remain for a longer time at the walls or even condensate on them [132]. They are not necessarily neutral, such that deposition from ions is under discussion as well [50]. The vapor pressure

strongly depends on the length of the oligomer backbones [163]. Such way, by direct radical reaction or subsequent activation due to electron and ion impact, or radiation, large molecules have a high probability to be cross-linked and polymerized, which is supported by the correlation between oligomerization and polymer deposition shown in the beginning of this paragraph.

Due to the above considerations, the deposition flux is calculated from the oligomerization rate¹⁴. The oligomerization rate in the gas phase was calculated by the chemical plasma model in Section 4.2.3. Integration of the oligomerization rate $dn_{ol}(z)/dt$ over half the reactor height yields the maximum theoretical flux of adsorbing particles: $\Gamma_{\text{ads.,max}} = \int_0^{d/2} dn_{ol}(z)/dt dz$. Accordingly,

$$\Gamma_{\text{ads.,max}} \geq \Gamma_{\text{adsorbing}} \quad (4.7)$$

should be fulfilled (compare Equation (1.38)).

2. Polymer flux: By evaluation of the layer growth in Section 4.4.1, it is found that at 20 Watt plasma power in a cw discharge¹⁵, the deposition rate is 6.8 nm per minute. Taking into consideration the chemical composition determined by XPS and the polymer density, this value corresponds to a polymerization flux $\Gamma_{\text{polymer}} = 4.2 \times 10^{14}$ carbon $\text{cm}^{-2}\text{s}^{-1}$. When this value is compared to the number of carbon atoms supplied by the feed gas in the same time, 6.3×10^{15} carbon atoms $\text{cm}^{-2}\text{s}^{-1}$, the polymerization yield is 7% per electrode. The same calculation can be performed for 5 Watt and 35 Watt. The polymerization fluxes are 1.6×10^{14} and 6.6×10^{14} carbon atoms $\text{cm}^{-2}\text{s}^{-1}$, the yields are 2.5% and 10.5% per electrode, respectively. The evaluation of the layer growth rate was also performed for pulsed discharges with 500 ms pulse period and variable duty cycle.
3. Flux of released particles: It is assumed that only CF_2 is released from the polymer, such that $\Gamma_{\text{released}} = \Gamma_{\text{CF}_2}$.

Thus, the balance Equation (1.38) is approximated by

$$\Gamma_{\text{ads.,max}} \geq \Gamma_{\text{polymer}} + \Gamma_{\text{CF}_2} \quad (4.8)$$

¹⁴assuming that the oligomer is lost completely as polymer at the electrodes

¹⁵10 sccm CHF_3 , 10 sccm Ar, 80 Pa

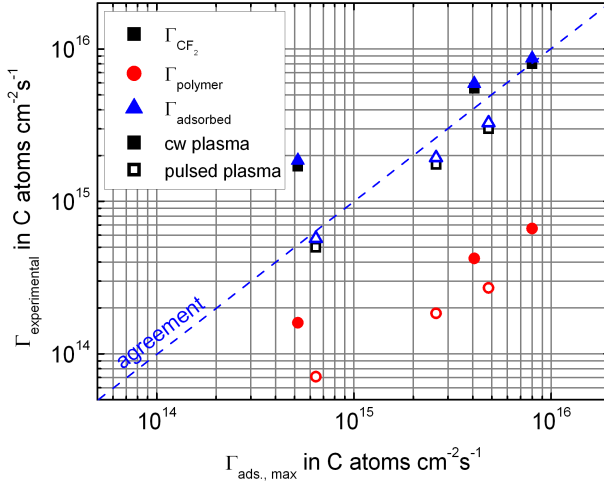


Figure 4.53: Comparison between the measured polymer and the maximum theoretical adsorption fluxes. Full symbols: cw plasma, powers 5, 20, and 35 Watt; hollow symbols: pulsed plasma at 20 Watt, 10%, 35%, and 60%, from left to right.

An open point so far is which oligomers participate in deposition. The best agreement between both sides of Equation (4.8) was obtained when oligomers with $C_{n \geq 2}$ backbones were included in the example data in Figure 4.53. Accordingly, unsaturated $n = 2$ as well as $n \geq 3$ oligomers are participating in polymerization. The previously mentioned possible bond breaks in small molecules due to excessive heat of reaction are not contradicting the inclusion of C_2 oligomers in $\Gamma_{\text{ads.,max}}$ because the fragments may contribute to Γ_{released} . When only $C_{n \geq 3}$ oligomers were included, the errors were larger by more than a factor of two.

Retention of oligomer structures is not observed even for larger molecules as suggested by the model. This is in agreement with the experiments where $\Gamma_{\text{CF}_2} \gg \Gamma_{\text{polymer}}$ is found, indicating that decomposition takes place at the surface. The high crosslinking of the polymer measured by XPS further shows that long-chain oligomer backbones are hardly retained.

The remaining discrepancies between theoretical and experimental data of Equation (4.8) are mainly due to incompleteness of reaction channels (e.g. no ion-neutral reactions were included) and/or incorrect reaction rates. Best agreement is seen for pulsed discharges, whereas the agreement is worst for low power cw discharges. It is suggested that the formation of oligomer in

the plasma exceeds the one obtained in the model. Besides that, the overall reaction pathways leading to polymer deposition confirm the assumptions in [132].

Appendix A

Gas flow dynamics in the reactor

In the setup used for the experiments, the flow system was simulated in Comsol Multiphysics 3.5. The reactor system was simplified to an axial symmetric model. An average flow of $F = 70$ sccm was introduced normal to the upper electrode. The outlet was simulated by a ring area set to a normal flow keeping the pressure at 100 Pa.

The resulting total, radial, and axial speed distributions are shown in Figures A.1, A.2 and A.3. As can be seen, the maximum flow speed in

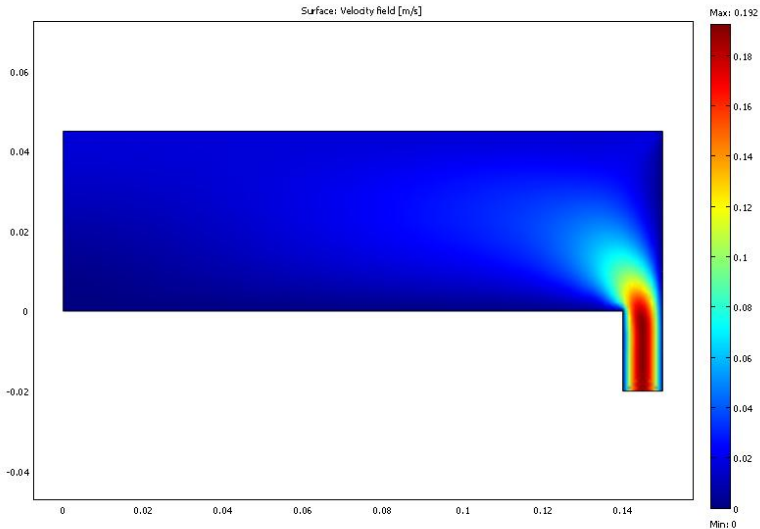


Figure A.1: Color plot of total flow speed as simulated for current setup

the middle of the reactor does not exceed 1.8 cm s^{-1} . This hardly affects chemical processes as chemical and diffusion kinetics are in the millisecond

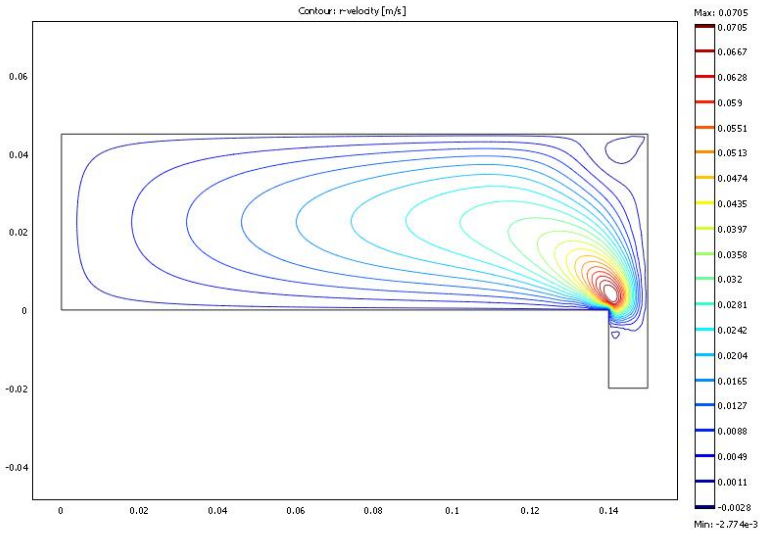


Figure A.2: Contour plot of radial flow speed as simulated for current setup

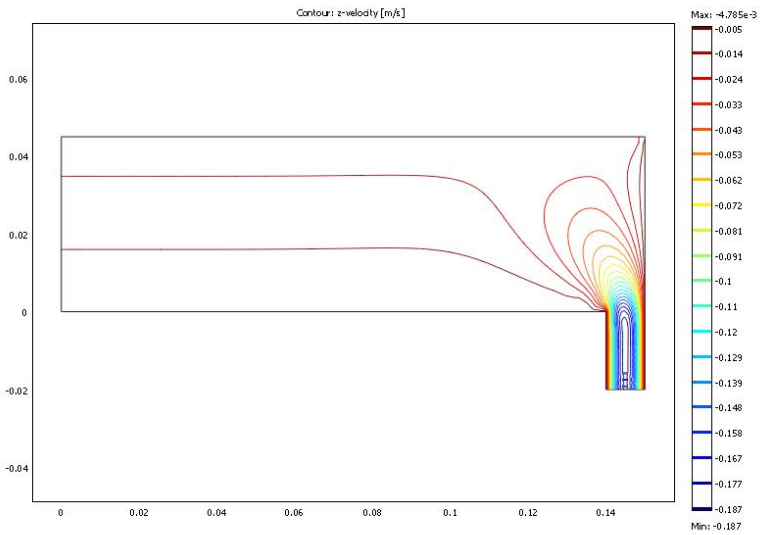


Figure A.3: Contour plot of axial flow speed as simulated for current setup

range. Furthermore, the major contributions to the velocity in the middle of the reactor arise from the axial component.

In a gas mixture, the pump-out of the different species is of great interest. For stable species, this represents a volume-exchange and dilution process which is described by

$$c(t) = c_0 k^t. \quad (1.1)$$

The dilution constant k can hardly be determined theoretically. The gas diffusion process of residual into new entering gas depends mainly on the gas velocity distributions and the diffusion coefficients.

Appendix B

LIF image calibration

The evaluation of LIF data includes several steps. The process can be comprehensively written a matrix form. The data which were acquired in 1024 height steps per point in time are written in columns:

$$\hat{S} = \begin{pmatrix} s_1(t_1) & s_1(t_2) & s_1(t_3) & \cdots & s_1(t_{max}) \\ s_2(t_1) & s_2(t_2) & s_2(t_3) & \cdots & s_2(t_{max}) \\ s_3(t_1) & s_3(t_2) & s_3(t_3) & \cdots & s_3(t_{max}) \\ \cdots & \cdots & \cdots & \cdots & \cdots \\ s_{1024}(t_1) & s_{1024}(t_2) & s_{1024}(t_3) & \cdots & s_{1024}(t_{max}) \end{pmatrix}.$$

The background matrix is organized accordingly:

$$\hat{B} = \begin{pmatrix} b_1(t_1) & \cdots & b_1(t_{max}) \\ \cdots & \cdots & \cdots \\ b_{1024}(t_1) & \cdots & b_{1024}(t_{max}) \end{pmatrix}.$$

Furthermore, differences arising from the optical pathway (lenses, windows, optical elements in the laser) and spatial differences in laser intensity have to be corrected. The correction matrix \hat{C}_i requires a determination of the spatial profile for one calibration data set $d_{l,0}$. Therefore, the spectra $s_{l,0}$ and $b_{l,0}$ are acquired and evaluated accordingly. The real density $\rho_{l,0}$ as determined by different measurements (see experimental Section 2.2) is divided by the standard data set $d_{l,0}$: $c_l = \rho_{l,0}/d_{l,0}$. Then, \hat{C}_i is written as

$$\hat{C}_i = \begin{pmatrix} c_1 & \cdots & c_{1024} \\ \cdots & \cdots & \cdots \\ c_1 & \cdots & c_{1024} \end{pmatrix}$$

Finally, the whole correction can be written as

$$\hat{D} = c_s(U_{MCP}) \cdot \hat{C}_i \cdot (\hat{S} - \hat{B})$$

where $c_s(U_{MCP})$ is a sensitivity correction factor accounting for the different settings of the multi-channel plate (MCP) gain voltage.

For further evaluation of reaction kinetics, diffusion and time behavior have to be determined. Diffusion and reaction kinetics are described in Chapter 1. Time derivatives as required in Equation (1.9) can be easily obtained by line-by-line readout and processing of \hat{D} .

At each time t_m , the averaged inclination is assigned to the local density $\rho_l(t_m)$:

$$\frac{d\rho_l(t_m)}{dt} = \frac{d\rho_{lm}}{dt} \approx \frac{\Delta\rho_{lm}}{\Delta t_m} \approx \frac{\rho_{l,m} - \rho_{l,m-1}}{t_m - t_{m-1}}. \quad (2.1)$$

This was found to be the best approach for the data.

Bibliography

- [1] J. W. Coburn and H. F. Winters, *Journal of Vacuum Science and Technology* **16**, 391 (1979).
- [2] R. d'Agostino, D. L. Flamm, and O. Auciello, editors, *Plasma Deposition, Treatment, and Etching of Polymers* (Academic Press, 1990).
- [3] J. Warnatz, U. Maas, and R. Dibble, *Combustion*, 3rd ed. (Springer, 2001).
- [4] J. P. Booth, H. Abada, P. Chabert, and D. B. Graves, *Plasma Sources Sci. Technol.* **14**, 273 (2005).
- [5] M. A. Lieberman and A. J. Lichtenberg, *Principles of Plasma Discharges and Materials Processing* (John Wiley & Sons, Inc., 1994).
- [6] Y. P. Raizer, M. N. Shneider, and N. A. Yatsenko, *Radio-Frequency Capacitive Discharges* (CRC Press, Inc., 1995).
- [7] G. J. M. Hagelaar and L. C. Pitchford, *Plasma Sources Science and Technology* **14**, 722 (2005).
- [8] K. K. S. Lau, K. K. Gleason, and B. L. Trout, *Journal of Chemical Physics* **113**, 4103 (2000).
- [9] D. R. Burgess, M. R. Zacharaiah, W. Tsang, and P. R. Westmoreland, *Progress in Energy and Combustion Science* **21**, 453 (1995).
- [10] P. W. Atkins and J. de Paula, *Physical Chemistry*, 8th edition ed. (Oxford University Press, Oxford, UK, 2006).
- [11] R. D. Levine and R. B. Bernstein, *Molekulare Reaktionsdynamik* (G. B. Teubner, Stuttgart, 1991).
- [12] J. Troe, *The Journal of Chemical Physics* **66**, 4758 (1977).
- [13] I. C. Plumb and K. R. Ryan, *Plasma Chemistry and Plasma Processing* **6**, 205 (1986).
- [14] B. Dils, J. Vertommen, S. A. Carl, L. Vereecken, and J. Peeters, *Phys. Chem. Chem. Phys.* **7**, 1187 (2005).

- [15] M. J. Schabel, T. W. Peterson, and A. J. Muscat, *Journal of Applied Physics* **93**, 1389 (2003).
- [16] D. Bethell, *Structure and Mechanism in Carbene Chemistry*, *Advances in Physical Organic Chemistry* Vol. 7 (Academic Press, London and New York, 1969), pp. 153–155.
- [17] W. J. R. Tyerman, *Trans. Faraday Soc.* **65**, 1188 (1969).
- [18] V. Franzen, *Chemische Berichte* **95**, 1964 (1962).
- [19] R. A. Mitsch and A. S. Rodgers, *International Journal of Chemical Kinetics* **1**, 439 (1969).
- [20] N. N. Buravtsev and Y. A. Kolbanovsky, *Journal of Fluorine Chemistry* **96**, 35 (1999).
- [21] F. Dalby, *Journal of Chemical Physics* **41**, 2297 (1964).
- [22] C. Suzuki, K. Sasaki, and K. Kadota, *Plasma Chemistry and Plasma Processing* **21**, 139 (2001).
- [23] C. Suzuki, K. Sasaki, and K. Kadota, *Jpn. J. Appl. Phys. Part 1* **37**, 5763 (1998).
- [24] G. I. Font, W. L. Morgan, and G. Mennenga, *Journal of Applied Physics* **91**, 3530 (2002).
- [25] C. Q. Jiao, R. Nagpal, and P. D. Haaland, *Chemical Physics Letters* **269**, 117 (1997).
- [26] M. A. Parkes, R. Y. L. Chim, C. A. Mayhew, V. A. Mikhailov, and R. P. Tuckett, *Molecular Physics* **104**, 263 (2006).
- [27] H. Jungblut, D. Hansen, and W. F. Schmidt, *IEEE Transactions on Electrical Insulation* **24**, 343 (1989).
- [28] E. Gogolides, M. Stathakopoulos, and A. Boudouvis, *Journal of Physics D: Applied Physics* **27**, 1878 (1994).
- [29] J. P. Booth, G. Cunge, P. Chabert, and N. Sadeghi, *Journal of Applied Physics* **85**, 3097 (1999).
- [30] D. Humbird, D. B. Graves, X. Hua, and G. S. Oehrlein, *Applied Physics Letters* **84**, 1073 (2004).

- [31] A. Vasenkov, X. Li, G. S. Oehrlein, and M. J. Kushner, *Journal of Vacuum Science and Technology A* **22**, 511 (2004).
- [32] D. Troya, *Journal of Physical Chemistry A* **109**, 5814 (2005).
- [33] K. L. Steffens and M. A. Sobolewski, Electrical control of plasma spatial uniformity investigated by planar laser-induced fluorescence, in *IEEE TRANSACTIONS ON PLASMA SCIENCE* Vol. 27, pp. 74–75, 1999.
- [34] K. L. Steffens and M. A. Sobolewski, *Journal of Vacuum Science & Technology A* **17**, 517 (1999).
- [35] S. Hayashi, K. Ishikawa, and M. Sekine, Time-resolved planar laser-induced fluorescence of fluorocarbon radicals in oxide etch process plasma, in *25th ICPIG. International Conference on Phenomena in Ionized Gases. Nagoya Univ. Nagoya, Japan*, edited by T. Goto Vol. 2, p. 91, 2001.
- [36] S. Hayashi, K. Ishikawa, and M. Sekine, *Jpn. J. Appl. Phys. Vol. Part 1* **41**, 2207 (2002).
- [37] K. L. Steffens and M. A. Sobolewski, *Journal of Vacuum Science & Technology A* **21**, 241 (2003).
- [38] K. L. Steffens and M. A. Sobolewski, 2-D Imaging of Temperature in CF₄ Plasmas, in *IEEE TRANSACTIONS ON PLASMA SCIENCE* Vol. 33, pp. 370–371, 2005.
- [39] J.-P. Booth, G. Cunge, F. Neuilly, and N. Sadeghi, *Plasma Sources Sci. Technol.* **7**, 423 (1998).
- [40] N. Bulcourt *et al.*, *Journal of Chemical Physics* **120**, 9499 (2004).
- [41] G. Cunge, J. Booth, and J. Derouard, *Chemical Physics Letters* **263**, 645 (1996).
- [42] I. Bronštein, K. A. Semedjajew, G. Musiol, and H. Mühlig, *Taschenbuch der Mathematik*, 3 ed. (Verlag Harri Deutsch, 1997).
- [43] K. Meyberg and P. Vachenauer, *Höhere Mathematik 2*, 4 ed. (Springer, 1997).
- [44] J. Luque, Lifbase, www.sri.com/psd/lifbase.
- [45] E. C. Benck *et al.*, *Journal of Vacuum Science & Technology B: Microelectronics and Nanometer Structures* **21**, 2067 (2003).

- [46] P. B. Davies, P. A. Hamilton, J. M. Elliott, and M. J. Rice, *Journal of Molecular Spectroscopy* **102**, 193 (1983).
- [47] D. S. King, P. K. Schenck, and J. C. Stephenson, *Journal of Molecular Spectroscopy* **78**, 1 (1979).
- [48] S. Sharpe, B. Hartnett, H. S. Sethi, and D. S. Sethi, *Journal of Photochemistry* **38**, 1 (1987).
- [49] R. d'Agostino, F. Cramarossa, and S. Benedictis, *Plasma Chemistry and Plasma Processing* **2**, 213 (1982).
- [50] J.-P. Booth, *Plasma Sources Sci. Technol.* **8**, 249 (1999).
- [51] W. W. Stoffels, E. Stoffels, and K. Tachibana, *Jpn. J. Appl. Phys.* **36**, 4638 (1997).
- [52] E. Stoffels, W. W. Stoffels, and K. Tachibana, *Review of Scientific Instruments* **69**, 116 (1998).
- [53] W. W. Stoffels, E. Stoffels, and K. Tachibana, *Journal of Vacuum Science & Technology A: Vacuum, Surfaces, and Films* **16**, 87 (1998).
- [54] K. Teii, M. Hori, T. Goto, and N. Ishii, *Journal of Applied Physics* **87**, 7185 (2000).
- [55] S. W. Ip and J. M. Toguri, *Journal of Materials Science* **29**, 688 (1994).
- [56] D. K. Owens and R. C. Wendt, *Journal of Applied Polymer Science* **13**, 1741 (1969).
- [57] J. Drelich, *The Journal of Adhesion* **63**, 31 (1997).
- [58] B. J. Tielsch and J. E. Fulghum, *Surface and Interface Analysis* **24**, 28 (1996).
- [59] B. J. Tielsch, J. E. Fulghum, and D. J. Surman, *Surface and Interface Analysis* **24**, 459 (1998).
- [60] B. J. Tielsch and J. E. Fulghum, *Surface and Interface Analysis* **25**, 904 (1998).
- [61] G. Beamson and D. Briggs, *High Resolution XPS of Organic Polymers* (Wiley, London, 1992).

- [62] I. Dalins and M. Karimi, *Journal of Vacuum Science & Technology A* **10**, 2921 (1992).
- [63] B. Beard and R. Brizzolara, *Surface Science Spectra* **2**, 8 (1993).
- [64] G. Nansé, E. Papirer, P. Fioux, F. Moguet, and A. Tressaud, *Carbon* **35**, 175 (1997).
- [65] G. Beamson and M. R. Alexander, *Surface and Interface Analysis* **36**, 323 (2004).
- [66] M. J. Kushner and D. Zhang, *Journal of Applied Physics* **88**, 3231 (2000).
- [67] D. Bose, M. V. V. S. Rao, T. R. Govindan, and M. Meyyappan, *Plasma Sources Science and Technology* **12**, 225 (2003).
- [68] M. Meyyappan, private communication, 2008.
- [69] V. Kolobov and R. Arslanbekov, *IEEE Transactions on Plasma Science* **34**, 895 (2006).
- [70] G. Hagelaar and L. Pitchford, Bolsig+, online, www.laplace.univ-tlse.fr, 2008.
- [71] D. Loffhagen and R. Winkler, *Journal of Physics D: Applied Physics* **29**, 618 (1996).
- [72] D. Loffhagen, G. L. Braglia, and R. Winkler, *Contributions to Plasma Physics* **38**, 527 (1998).
- [73] M. Goto, K. Nakamura, H. Toyoda, and H. Sugai, *Jpn. J. Appl. Phys. Part 1* **33**, 3602 (1994).
- [74] J. de Urquijo, *Journal of Physics: Conference Series* **71**, 012006 (2007).
- [75] J. E. Baio, H. Yu, D. W. Flaherty, H. F. Winters, and D. B. Graves, *Journal of Physics D: Applied Physics* **40**, 6969 (2007).
- [76] L. Christophorou and J. Olthoff, *Journal of Physical and Chemical Reference Data* **28**, 967 (1999).
- [77] W. L. Morgan, C. Winstead, and V. McKoy, *Journal of Applied Physics* **90**, 2009 (2001).

- [78] I. Torres, R. Martínez, and F. Castaño, *Journal of Physics B: Atomic, Molecular and Optical Physics* **35**, 2423 (2002).
- [79] D. G. Voloshin, T. V. Rakhimova, K. S. Klopovskiy, and Y. A. Mankelevich, *Journal of Physics: Conference Series* **44**, 121 (2006).
- [80] D. Voloshin *et al.*, *IEEE Transactions on Plasma Science* **35**, 1691 (2007).
- [81] Á. Yanguas-Gil, J. Cotrino, and L. L. Alves, *Journal of Physics D: Applied Physics* **38**, 1588 (2005).
- [82] E. Gargioni and B. Grosswendt, *Reviews of Modern Physics* **80**, 451 (2008).
- [83] M. Haverlag *et al.*, *Journal of Applied Physics* **70**, 3472 (1991).
- [84] B. McMillin and M. Zachariah, *Journal of Applied Physics* **77**, 5538 (1995).
- [85] G. A. Hebner and K. E. Greenberg, *Journal of Research of the National Institute of Standards and Technology* **100**, 373 (1995).
- [86] M. R. Zachariah and B. K. McMillin, *Solid State Technology* **39**, 147 (1996).
- [87] J. B. Boffard, C. C. Lin, and C. A. DeJoseph Jr, *Journal of Physics D: Applied Physics* **37**, R143 (2004).
- [88] Z. Gavare, D. Gött, A. V. Pipa, J. Röpcke, and A. Skudra, *Plasma Sources Science and Technology* **15**, 391 (2006).
- [89] D. Mariotti, Y. Shimizu, T. Sasaki, and N. Koshizaki, *Applied Physics Letters* **89**, 201502 (2006).
- [90] E. Augustyniak, S. Filiminov, and J. Borysow, *Bull. Amer. Phys. Soc.* **37**, 2002 (1992).
- [91] G. A. Hebner, *Journal of Applied Physics* **80**, 2624 (1996).
- [92] SIGLO-RF v.1.11, online, www.siglo-kinema.com, 1998.
- [93] J.-P. Boeuf, *Phys. Rev. A* **36**, 2782 (1987).
- [94] J. P. Boeuf and L. C. Pitchford, *Phys. Rev. E* **51**, 1376 (1995).
- [95] E. Basurto and J. de Urquijo, *Journal of Applied Physics* **91**, 36 (2002).

- [96] A. Kono, M. Haverlag, G. M. W. Kroesen, and F. J. de Hoog, *Journal of Applied Physics* **70**, 2939 (1991).
- [97] H. W. Ellis, R. Y. Pai, E. W. McDaniel, E. A. Mason, and L. A. Viehland, *Atomic Data and Nuclear Data Tables* **17**, 177 (1976).
- [98] H. W. Ellis *et al.*, *Atomic Data and Nuclear Data Tables* **22**, 179 (1978).
- [99] Z. Petrovič *et al.*, *Applied Surface Science* **253**, 6619 (2007).
- [100] V. Georgieva, A. Bogaerts, and R. Gijbels, *Phys. Rev. E* **69**, 026406 (2004).
- [101] D. R. Lide, editor, *Handbook of Chemistry and Physics*, 85th ed. (CRC Press, 2004-2005).
- [102] G. A. Hebner and P. A. Miller, *Journal of Applied Physics* **87**, 7660 (2000).
- [103] D. Edelson and D. L. Flamm, *Journal of Applied Physics* **56**, 1522 (1984).
- [104] S. Rauf and M. J. Kushner, *Journal of Applied Physics* **82**, 2805 (1997).
- [105] P. Ho, J. E. Johannes, R. J. Buss, and E. Meeks, *Journal of Vacuum Science & Technology A: Vacuum, Surfaces, and Films* **19**, 2344 (2001).
- [106] J. Kerr and M. Parsonage, *Evaluated Kinetic Data on Gas Phase Addition Reactions. Reactions of Atoms and Radicals with Alkenes, Alkynes and Aromatic Compounds* (Butterworths, London, 1972).
- [107] C. J. Ultee, *Chemical Physics Letters* **46**, 366 (1977).
- [108] L. P. Walkauskas and F. Kaufman, Gas Phase Hydrogen Atom Recombination, in *Proc. 15th Symp. (Int.) on Combustion*, The Combustion Institute, Pittsburgh, 1975.
- [109] T. Nakano and K. Yanagita, *Jpn. J. Appl. Phys. Part I* **42**, 663 (2003).
- [110] F. Gaboriau *et al.*, *J. Vac. Sci. Technol. A* **20**, 919 (2002).
- [111] P. Ray and P. Chaudhuri, *Czechoslovak Journal of Physics* **53**, 229 (2003).

- [112] R. B. Piejak, J. Al-Kuzee, and N. S. J. Braithwaite, *Plasma Sources Sci. Technol.* **14**, 734 (2005).
- [113] S. G. Hansen, G. Luckman, and S. D. Colson, *Applied Physics Letters* **53**, 1588 (1988).
- [114] T. Arai *et al.*, *Jpn. J. Appl. Phys. Part 2* **34**, L1392 (1995).
- [115] P. Fendel, A. Francis, and U. Czarnetzki, *Plasma Sources Science Technology* **14**, 1 (2005).
- [116] K. Ryan and I. Plumb, *Plasma Chemistry and Plasma Processing* **4**, 141 (1984).
- [117] A. Francis, P. Fendel, S. Narishige, U. Czarnetzki, and H. Döbele, Structure and Dynamics of Radical Densities in a Capacitively Coupled RF-Discharge in CF₄ with Various Electrode Materials, in *Joint Conference ESCAM PIG 16 and ICRP 5. Conference Proceedings.*, pp. 161–162, Univ. Joseph Fourier, Grenoble, France, 2002.
- [118] M. N. R. Ashfold, F. Castaño, G. Hancock, and G. W. Ketley, *Chemical Physics Letters* **73**, 421 (1980).
- [119] D. L'Esperance, B. A. Williams, and J. W. Fleming, *Chemical Physics Letters* **280**, 113 (1997).
- [120] K. Maruyama, A. Sakai, and T. Goto, *Journal of Physics D: Applied Physics* **26**, 199 (1993).
- [121] K. Maruyama and T. Goto, *Journal of Physics D: Applied Physics* **28**, 884 (1995).
- [122] K. Maruyama, K. Ohkouchi, Y. Ohtsu, and T. Goto, *Japanese Journal of Applied Physics* **33**, 4298 (1994).
- [123] M. E. Jacox, *Journal of Molecular Spectroscopy* **81**, 349 (1980).
- [124] K. Sasaki, H. Furukawa, C. Suzuki, and K. Kadota, *Jpn. J. Appl. Phys. Part 2* **38**, L954 (1999).
- [125] K. Sasaki, H. Furukawa, K. Kadota, and C. Suzuki, *Journal of Applied Physics* **88**, 5585 (2000).
- [126] C. Suzuki, K. Sasaki, and K. Kadota, *Journal of Applied Physics* **82**, 5321 (1997).
- [127] H. Nakagawa *et al.*, *Jpn. J. Appl. Phys. Part 1* **41**, 319 (2002).

- [128] N. Mackie, V. Ventura, and E. Fisher, *Journal of Physical Chemistry B* **101**, 9425 (1997).
- [129] J.-P. Booth and C. Corr, *Plasma Sources Sci. Technol.* **15**, 112 (2006).
- [130] H. Abada, P. Chabert, J.-P. Booth, J. Robiche, and G. Cartry, *Journal of Applied Physics* **92**, 4223 (2002).
- [131] M. Haverlag, E. Stoffels, W. W. Stoffels, G. M. W. Kroesen, and F. J. de Hoog, *J. Vac. Sci. Technol. A* **14**, 384 (1996).
- [132] G. Cunge and J. P. Booth, *Journal of Applied Physics* **85**, 3952 (1999).
- [133] S. Koda, *Chemical Physics Letters* **69**, 574 (1980).
- [134] S. Koda, *Chemical Physics Letters* **55**, 353 (1978).
- [135] M. Kuzuya, T. Yamashiro, S.-i. Kondo, M. Sugito, and M. Mouri, *Macromolecules* **31**, 3225 (1998).
- [136] M. Haupt, J. Barz, and C. Oehr, *Plasma Processes and Polymers* **5**, 33 (2008).
- [137] S. Siegel and H. Hedgpeth, *Journal of Chemical Physics* **46**, 3904 (1967).
- [138] D. Mann and B. Trush, *Journal of Chemical Physics* **33**, 1732 (1960).
- [139] D. E. Milligan, D. E. Mann, M. E. Jacox, and R. A. Mitsch, *Journal of Chemical Physics* **41**, 1199 (1964).
- [140] M. E. Jacox and D. E. Milligan, *Journal of Chemical Physics* **50**, 3252 (1969).
- [141] O. Suto and J. Steinfeld, *Chem. Phys. Let.* **168**, 181 (1990).
- [142] K. Seki *et al.*, *Physica Scripta* **41**, 167 (1990).
- [143] T. Gumpenberger, J. Heitz, D. Bauerle, and T. C. Rosenmayer, *EPL (Europhysics Letters)* **70**, 831 (2005).
- [144] C. Wesdemiotis, H. Schwarz, H. Budzikiewicz, and E. Vogel, *Organic Mass Spectrometry* **16**, 89 (1981).
- [145] H. Yasuda, *Plasma Polymerization* (Academic Press, New York, 1985).

- [146] J. Barz, M. Haupt, U. Vohrer, H. Hilgers, and C. Oehr, *Surface and Coatings Technology* **200**, 453 (2005), PSE 2004.
- [147] J. Barz, M. Haupt, H. Hilgers, and C. Oehr, Ultrathin carbon-fluorine films, in *XXVIIIth ICPIG, Eindhoven, the Netherlands* No. 03-359, 2005.
- [148] T. Nishino, M. Meguro, K. Nakamae, M. Matsushita, and Y. Ueda, *Langmuir* **15**, 4321 (1999).
- [149] C. Fang and J. Drelich, *Langmuir* **20**, 6679 (2004).
- [150] L. Gao and T. J. McCarthy, *Langmuir* **22**, 6234 (2006).
- [151] P. J. Cumpson, *Surface and Interface Analysis* **20**, 727 (1993).
- [152] P. J. Cumpson and M. P. Seah, *Surface and Interface Analysis* **25**, 430 (1997).
- [153] A. Jablonski and C. Powell, *Journal of Electron Spectroscopy and Related Phenomena* **100**, 137 (1999).
- [154] C. J. Powell and A. Jablonski, *Journal of Electron Spectroscopy and Related Phenomena* **114-116**, 1139 (2001).
- [155] A. Jablonski and C. J. Powell, *Surface Science Reports* **47**, 33 (2002).
- [156] C. J. Powell and A. Jablonski, *Surface and Interface Analysis* **33**, 211 (2002).
- [157] C. Powell and A. Jablonski, *NIST Electron Effective-Attenuation-Length Database - Version 1.1* (Gaithersburg, MD, Gaithersburg, MD, 2003).
- [158] E. J. Winder and K. K. Gleason, *Journal of Applied Polymer Science* **78**, 842 (2000).
- [159] J. Barz, M. Haupt, K. Pusch, M. Weimer, and C. Oehr, *Plasma Processes and Polymers* **3**, 540 (2006).
- [160] M. von Gradowski *et al.*, *Surface and Coatings Technology* **200**, 334 (2005).
- [161] H. J. Griesser, D. Youxian, A. E. Hughes, T. R. Gengenbach, and A. W. H. Maut, *Langmuir* **7**, 2484 (1991).

- [162] M. Strobel, C. S. Lyons, and K. L. Mittal, editors, *Plasma Surface Modification of Polymers: Relevance to Adhesion*, 1st ed. (VSP, Zeist, The Netherlands, 1994).
- [163] K. R. Hall, *Vapor Pressure and Antoine Constants for Hydrocarbons, and S, Se, Te, and Halogen Containing Organic Compounds*, Landolt-Börnstein - Group IV Physical Chemistry, Numerical Data and Functional Relationships in Science and Technology Vol. 20 A (Springer, 1999).

List of Figures

1.1	Plasma regions in electronegative rf plasmas.	22
1.2	Reaction zones in the plasma.	22
1.3	Major reaction routes.	36
2.1	Plasma setup as used for the experiments	43
2.2	Geometry of the plasma setups used for the experiments, not true to scale.	45
2.3	Setup for LIF	47
2.4	ICCD images in PLIF mode.	48
2.5	LIFBASE excitation spectra of CF and NO	52
2.6	LIF excitation scans of CF and NO	54
2.7	Difluorocarbene absorption spectra	56
2.8	Density calibration profile of the CF radical (fluorescence imaging mode)	58
2.9	Density profile of CF ₂ (spectral mode)	59
2.10	Effect of excitation wavelength and axial position on the measured signal.	59
2.11	CF ₂ density profile as obtained in the imaging mode.	61
2.12	Comparison of concentration profiles obtained in the fluorescence imaging and the spectral mode.	61
2.13	Setup for mass spectrometry	62
3.1	Comparison of simulated and Maxwellian EEDFs	66
3.2	Electron collision cross sections of CHF ₃	69
3.3	Electron collision cross sections of argon	70
3.4	Rate coefficients in dependence on mean electron energy	71
3.5	$\langle \epsilon \rangle$ and μ versus the reduced electric field, different cross sections	73
3.6	Detailed cross sections for CHF ₃	74
3.7	Plasma parameter effect on the EEDF	75
3.8	Plasma parameter effect on the $\langle \epsilon \rangle$ and on μ	76
3.9	Gas composition effect on the EEDF	77
3.10	Gas composition effect on the mean electron energy and on the electron mobility.	78
3.11	Total ionization rate coefficients.	79

3.12	Influence of superelastic scattering	80
3.13	Mean electron energy vs. plasma power.	87
3.14	Charge carrier densities vs. discharge voltage.	88
3.15	Power-voltage characteristics at different pressures.	89
3.16	Current-voltage characteristics at different pressures.	89
3.17	Major electron-induced dissociation channels versus power.	91
3.18	Ratios of electron-induced dissociation channels versus power.	92
3.19	Electron collision induced ionization and attachment versus power.	93
3.20	Dissociation rates vs. $\langle \epsilon \rangle$ for Maxwellian and simulated EEDFs	94
3.21	Attachment and ionization in chemical simulations.	101
4.1	Power-voltage characteristics of pure argon, simulation and experiment.	105
4.2	Power-voltage characteristics of pure CHF ₃ , simulation and experiment.	106
4.3	Power-voltage characteristics in pure CHF ₃	107
4.4	Power-voltage characteristics at 5 sccm and different pressures.	108
4.5	Power-voltage characteristics at 10 sccm and different pressures.	109
4.6	Power-voltage characteristics at 15 sccm and different pressures.	110
4.7	n_e , comparison of experiment and model.	112
4.8	Electron density profile and optical emission of difluorocarbene.	113
4.9	Space- and time-resolved development of the CF density	116
4.10	Cross-sectional plot of Figure 4.9	116
4.11	CF density in the afterglow, semilog. plot.	117
4.12	Space- and time-resolved development of the CF ₂ density	118
4.13	Time-resolved absorption measurements	119
4.14	Cross sectional plot of Figure 4.12	119
4.15	Time-dependent Comsol simulations for the profile develop- ment.	122
4.16	Experimental data of the center density in comparison to simulation results.	122
4.17	Comparison of experimental data of the initial and final CF ₂ profiles to simulation results.	123
4.18	Difluorocarbene density in the afterglow.	124
4.19	Concentration gradient plots of Figure 4.15.	125
4.20	Density gradients for the flow calculation.	126
4.21	Surface flux of difluorocarbene, standard plasma	126
4.22	Surface flux of difluorocarbene, power and duty cycle var.	127
4.23	Surface flux of difluorocarbene, flow and pressure var.	128
4.24	Substrate dependence of difluorocarbene flux.	130

4.25	Pulsed discharge simulation without surface fluxes.	132
4.26	Introduction of surfaces fluxes to the chemical model.	134
4.27	Comparison of flux model to experimental data.	135
4.28	Comsol model with additional recombination reaction.	136
4.29	Comparison of flux model to experimental data.	137
4.30	Major production and loss processes of CF.	139
4.31	Total rate of CF in experiment and model.	140
4.32	Major production and loss rates of CF ₂	141
4.33	Rate balance of difluorocarbene.	142
4.34	Difluorocarbene diffusion and effect on CF.	144
4.35	Ion currents and surface flux of difluorocarbene.	147
4.36	Example mass spectrum.	150
4.37	Low-molecular weight species detected by mass spectrometry.	151
4.38	Oligomer fragments detected by mass spectrometry.	153
4.39	Hydrogen retention in chain and end groups in dependence on plasma power.	155
4.40	Simulation of abundant, non-carbonic species in cw plasmas.	156
4.41	Simulation on hydrogen-bond retention in cw plasmas.	157
4.42	Simulation on formation of oligomers in cw plasmas.	158
4.43	Pressure and flow dependence of oligomer formation.	159
4.44	Simulation of oligomer formation in a pulsed discharge	160
4.45	Deposition rate vs. duty cycle and power.	162
4.46	Surface tension vs. coating thickness.	164
4.47	Surface chemical composition versus duty cycle.	165
4.48	Development of the carbon C1s spectrum vs. duty cycle.	166
4.49	Development of the carbon C1s spectrum vs. duty cycle.	167
4.50	Angle-resolved XPS of plasma polymer.	168
4.51	Surface tension versus hydrophobic groups.	169
4.52	ESR signal of plasma polymer.	170
4.53	Polymer vs. maximum theoretical adsorption flux.	173
A.1	Color plot of total flow speed	175
A.2	Contour plot of radial flow speed	176
A.3	Contour plot of axial flow speed	176

List of Tables

1.1	Transport processes due to gradients	25
1.2	Enthalpies of formation	32
1.3	Reaction orders, differential equations, and solutions	33
1.4	Ion reaction channels and rates	40
2.1	Variables for plasma experiments	44
2.2	Input parameters for LIFBASE	51
3.1	EEDF standard simulation parameters	70
3.2	Zero-field ion mobilities	83
3.3	Ion dissipation channels	85
3.4	Reaction channels considered in chemical modeling: Dissociation and ionic channels	96
3.5	Reaction channels considered in chemical modeling: neutral reactions	97
3.6	Reaction channels considered in chemical modeling: neutral reactions, continued	98
3.7	Reaction channels considered in chemical modeling: F- and H-atom reactions	99
3.8	Reaction channels considered in chemical modeling: F- and H-atom reactions, continued	100
4.1	Simulation parameters for profile studies	121
4.2	Difluorocarbene wall production.	131
4.3	CF ₂ wall production in the literature	146
4.4	Mass fragments and suggested composition	152

Lebenslauf

Jakob Philipp Barz, geboren am 7. März 1977 in Tübingen

1996	Abitur am Wildermuth-Gymnasium in Tübingen
1996-1997	Zivildienst beim Strahlenschutzbereich II des Universitätsklinikums Tübingen
1997-2003	Studium der Physik an der Universität Stuttgart
2002-2003	Diplomarbeit am 1. Physikalischen Institut der Universität Stuttgart (Prof. Manfred Dressel)
2003	Abschluß als Diplom-Physiker
2003-2010	Doktorarbeit, Betreuung über das Institut für Plasmaforschung, Universität Stuttgart (Prof. Achim Lunk)
2003-2007	Doktorand am Fraunhofer IGB, Stuttgart
2007-2009	wiss. Angestellter am Fraunhofer IGB, Stuttgart
seit 09/2009	wiss. Angestellter am IGVT der Universität Stuttgart

Liste bisheriger Publikationen:

- J. Barz, M. Dumm, M. Dressel, C. Meziere, and P. Batail, *Journal de Physique IV* **114** 289 (2004).
- J. Barz, M. Haupt, U. Vohrer, H. Hilgers, and C. Oehr, *Surface and Coatings Technology* **200**, 453 (2005).
- M. von Gradowski, B. Jacoby, H. Hilgers, J. Barz, M. Wahl, and M. Kopnarski, *Surface and Coatings Technology* **200**, 453 (2005).
- M. Haupt, J. Barz, U. Vohrer, H. Hilgers, and C. Oehr, *Vakuum in Forschung und Praxis* **17**, 329 (2005).
- M. Haupt, J. Barz, U. Vohrer, H. Hilgers, and C. Oehr, *NanoS* **01**, 23 (2006).
- J. Barz, M. Haupt, K. Pusch, M. Weimer, and C. Oehr, *Plasma Processes and Polymers* **3**, 540 (2006).
- M. Haupt, J. Barz, U. Vohrer, and C. Oehr, *Jahrbuch Oberflächentechnik*, Band 62 (Eugen G. Leuze, 2006, ISBN 3-87480-222-1).
- D. Faltermeier, J. Barz, M. Dumm, M. Dressel, N. Drichko, B. Petrov, V. Semkin, R. Vlasova, C. Meziere, and P. Batail, *Phys. Rev. B* **76**, 165113 (2007).
- J. Barz, B. Elkin, M. Müller, and C. Oehr, *Jahrbuch Oberflächentechnik*, Band 64 (Eugen G. Leuze, 2008, ISBN 978-3-87480-245-1).
- M. Haupt, J. Barz, and C. Oehr, *Plasma Processes and Polymers* **5**, 33 (2008).
- R. Vlasova, N. Drichko, B. Petrov, V. Semkin, D. Faltermeier, J. Barz, M. Dumm, M. Dressel, C. Mezier, and P. Batail, *Physics of the Solid State* **51**, 1041 (2009).

Eidesstattliche Erklärung

Hiermit erkläre ich an Eides statt, daß ich die Dissertation "Particle dynamics simulation and diagnostics of the PECVD processes in fluorocarbon rf discharges" selbst verfaßt und keine anderen als die angegebenen Quellen und Hilfsmittel verwendet habe.

Stuttgart, im Juli 2010

Jakob Barz